Université de Montréal

Numerical Insights for AAA Growth Understanding and Predicting: Morphological and Hemodynamic Risk Assessment Features and Transient Coherent Structures Uncovering

par
Florian Joly

Département de pharmacologie et physiologie, Institut de génie biomédical,
Faculté de Médecine

Thèse présentée en vue de l'obtention du grade de Philosophiæ doctor
Doctorat en génie biomédical

Août, 2019

RÉSUMÉ

Les anévrismes de l'aorte abdominale (AAA) sont des dilatations localisées et fréquentes de l'aorte. En cas de rupture, seul un traitement immédiat peut prévenir la morbidité et la mortalité. Le diamètre maximal AAA (D_{max}) et la croissance sont les paramètres actuels pour évaluer le risque associé et planifier l'intervention, avec des seuils inférieurs pour les femmes. Cependant, ces critères ne sont pas personnalisés ; la rupture peut se produire à un diamètre inférieur et les patients vivre avec un AAA important. Si l'on sait que la maladie est associée à une modification de la morphologie et de la circulation sanguine, à un dépôt de thrombus intra-luminal et à des symptômes cliniques, les mécanismes de croissance ne sont pas encore entièrement compris. Dans cette étude longitudinale, une analyse morphologique et des simulations de flux sanguins sont effectuées et comparées aux sujets témoins chez 32 patients ayant reçu un diagnostic clinique d'AAA et au moins 3 tomodensitogrammes de suivi par patient. L'objectif est d'abord d'examiner quels paramètres stratifient les patients entre les groupes sains, à faible risque et à risque élevé. Les corrélations locales entre les paramètres hémodynamiques et la croissance de l'AAA sont également explorées, car la croissance hétérogène de l'AAA n'est actuellement pas comprise. Enfin, les paramètres composites sont construits à partir de données cliniques, morphologiques et hémodynamiques et de leur capacité à prédire si un patient sera soumis à un test de risque. La performance de ces modèles construits à partir de l'apprentissage supervisé est évaluée par les ROC AUC : ils sont respectivement de $0,73 \pm 0,09$, $0,93 \pm 0,08$, $0,96 \pm 0,10$. En incorporant tous les paramètres, on obtient une AUC de $0,98 \pm 0,06$. Pour mieux comprendre les interactions entre la croissance et la topologie de l'écoulement de l'AAA, on propose un worflow spécifique au patient pour calculer les exposants de Lyapunov en temps fini et extraire les structures lagrangiennes-cohérentes (SLC). Ce modèle de calcul a d'abord été comparé à l'imagerie par résonance magnétique (IRM) par contraste de phase 4-D chez 5 patients. Pour mieux comprendre l'impact de la topologie de l'écoulement et du transport sur la croissance de l'AAA, des SLC hyper-

boliques répulsives ont été calculées chez un patient au cours d'un suivi de 8 ans, avec 9 mesures morphologiques volumétriques de l'AAA par tomographie-angiographie. Les SLC ont défini les frontières du jet entrant dans l'AAA. Les domaines situés entre le SLC et le mur aortique ont été considérés comme des zones de stagnation. Leur évolution a été étudiée lors de la croissance de l'AAA. En plus des SLC hyperboliques (variétés attractives et répulsives) découvertes par FTLE, les SLC elliptiques ont également été considérées. Il s'agit de régions dominées par la rotation, ou tourbillons, qui sont de puissants outils pour comprendre les phénomènes de transport dans les AAA.

Mots clés : anévrismes de l'aorte abdominale ; simulation numérique ; hémodynamique ; structures lagrangiennes cohérentes

ABSTRACT

Abdominal aortic aneurysms (AAA) are localized, commonly-occurring dilations of the aorta. In the event of rupture only immediate treatment can prevent morbidity and mortality. The AAA maximal diameter (D_{max}) and growth are the current metrics to evaluate the associated risk and plan intervention, with lower thresholds for women. However, these criteria lack patient specificity; rupture may occur at lower diameter and patients may live with large AAA. If the disease is known to be associated with altered morphology and blood flow, intra-luminal thrombus deposit and clinical symptoms, the growth mechanisms are yet to be fully understood. In this longitudinal study, morphological analysis and blood flow simulations for 32 patients with clinically diagnosed AAA and at least 3 follow-up CT-scans per patient, are performed and compared to control subjects. The aim is first to investigate which metrics stratify patients between healthy, low risk and high risk groups. Local correlations between hemodynamical metrics and AAA growth are also explored, as AAA heterogeneous growth is currently not understood. Finally, composite metrics are built from clinical, morphological, and hemodynamical data, and their ability to predict if a patient will become at risk tested. Performance of these models built from supervised learning is assessed by ROC AUCs: they are respectively, 0.73 ± 0.09, 0.93 ± 0.08, 0.96 ± 0.10. Mixing all metrics, an AUC of 0.98 ± 0.06 is obtained. For further insights into AAA flow topology/growth interaction, a workout of patient-specific computational flow dynamics (CFD) is proposed to compute finite-time Lyapunov exponents and extract Lagrangian-coherent structures (LCS). This computational model was first compared with 4-D phase-contrast magnetic resonance imaging (MRI) on 5 patients. To better understand the impact of flow topology and transport on AAA growth, hyperbolic, repelling LCS were computed in 1 patient during 8-years follow-up, including 9 volumetric morphologic AAA measures by computed tomography-angiography (CTA). LCS defined barriers to Lagrangian jet cores entering AAA. Domains enclosed between LCS and the aortic wall were considered to be stagnation zones. Their evolution was studied during AAA growth.

In addition to hyperbolic (attracting and repelling) LCS uncovered by FTLE, elliptic LCS were also considered. Those encloses rotation-dominated regions, or vortices, which are powerful tools to understand the flow transport in AAA.

Keywords: abdominal aortic aneurysms; computational fluid mechanics; hemodynamics ; Lagrangian coherent structures

CONTENTS

LIST OF TABLES

LIST OF FIGURES

NOMENCLATURE

Abbreviations

AA Abdominal Aorta

AAA Abdominal Aortic Aneurysm

AAA Abdominal Aortic Aneurysnm

aFTLE augmented Finite Time Lyapunov Exponents

AUC Area Under Curve

BC Boundary Condition

BMI Body Mass Index

CFD Computational Fluid Dynamics

CFL Courant–Friedrichs–Lewy (condition)

CSD Computational Structural Dynamics

CT (X-ray) Computed Tomography

CTA (X-ray) Computed Tomography-Angiography

D_{max} Maximal diameter

D_{max}^{lumen} Maximal diameter, lumen only

DIZ Dynamically Isolated Zone

DLP Dyslipidemia

DSA Digital Substraction Angiography

ECAP Endothelial Cell Activation Potential

EV Eulerian Vortices

FEA Finite Element Analysis

FSI Fluid Structure Interaction

FTLE Finite Time Lyapunov Exponents

FVM Finite Volume Method

GCI Grid Convergence Index

ILT Intra-Luminal Thrombus

IVD Instantaneous Vorticity Deviation

LAVD Lagrangian-Averaged Vorticity Deviation

LBM Lattice Boltzmann Method

LCS Lagragian Coherent Structure

LOF Local Outlier Factor

LV Lagrangian Vortices

MMP-2 Matrix Metalloproteinase-2

MRI Magnetic Resonance Imaging

NSI Normalized Shape Index

OSI Oscillatory Shear Index

PC-MRI Phase-Contrast MRI

PISO Pressure-Implicit with Splitting of Operators

PRI Particle Residence Index

PRT Particle Residence Time

PSS Peak Shear Stress

PWS Peak Wall Stress (solid mechanics)

PWS Peak Wall Stress

RBC Red Blood Cells

RCR Lumped-parameters Windkessel model (R, resitance; C, capacitance)

Re Reynolds number

RK45 Runge-Kutta method of order 4(5)

ROC Receiver Operating Characteristic

RPI Rupture Potential Index

RRT Relative Residence Time

SIMPLE Semi-Implicit Method for Pressure Linked Equations

TAWSS Time Average Wall Shear Stress

VS Vortical Structure

WSS Wall Shear Stress

WSSG Wall Shear Stress Gradient

Symbols

τ_0	Shear stress when $\dot{\gamma} \to 0$
$\dot{\gamma}$	Shear rate
η	Apparent viscosity
λ	Characteristic time $^{-1}$
$\mathscr{B}$	Outermost level surface of $\mathscr{V}$
$\mathscr{C}$	Innermost level surface of $\mathscr{V}$
$\mathscr{V}$	Set of nested tubular surfaces
∇	Nabla operator
Ω	Computational volume
ω	Vorticity
σ	FTLE
τ	Shear stress
α	Womersley number
μ	Dynamic viscosity
ρ	Density
τ_w	Wall Shear Stress
ξ	Convergence criteria
St	Stokes number
η_∞	Viscosity when $\dot{\gamma} \to \infty$

λ_{max} Maximal eigenvalue of the Cauchy-Green tensor of flow

Co Courant–Friedrichs–Lewy condition

T Cardiac period

Torture numbers, and they'll confess to anything.

Gregg Easterbrook

ACKNOWLEDGMENTS

Firstly, I would like to express my sincere gratitude to my advisor Claude Kauffmann for the opportunity he gave me to do my research at the LCTI. I had the opportunity to manage my research project in total autonomy, from scientific questions to the tools choice. Having Gilles Soulez as co-director allowed me to keep in mind the objectives of the thesis, i.e. to provide technological solutions to clinical issues, when it is easy to forget why we are here to focus on more fundamental issues. In addition to his clinical pragmatism, I thank him for the material support and access to the patient data necessary for my work and especially for his ability to listen and mediate. Otherwise it would have been difficult not to give in to such puerility and lack of scientific rigour. Finally, I am extremely grateful for the involvement of Irène Vignon-Clémentel. Despite her late involvement, her role was decisive and she convinced my supervisors - and myself - of the value of my work and pushed me to promote it and finish it. I was fortunate that Simon Lessard's good soul was present at the LCTI. Knowing nothing about medical imaging, he trained me in the technologies used by the team and helped me with data acquisition and image segmentation. If in the end we spent more time talking about movies and coffee than image processing, it made my stay in Quebec more enjoyable, from the 7:30 coffee break to the evening class at the ETS. In addition, his skills as an email archivist proved to be very beneficial afterwards. A thought also for David Roy, the only comrade in computer simulation at the lab. I would not forget his earplugs and his constant willingness to help. Also a big thank you to Jennifer Satterthwaite. I could never say her name, but she was always there to help and with a smile that brought a little cheer to the team. I don't forget Marta, Mélusine and the other LBEV girls who made our floor more lively and liveable.

The thesis does not stop as soon as one steps outside the laboratory. That is why I would always be grateful to my parents for their support and the freedom I had in my choices. And for having faced Quebec mosquitoes and deer flies many times. And also my brother who, despite the distance, was more present than anyone would imagine from a

brother.

Finally, I do not forget the one who encouraged me to complete this work and accompanied me from proofreading to defense. To Pauline, the one who supports me and helps me to move forward.

CHAPTER 1

Introduction

1.1 AAA clinical context and risk assessment criteria

Abdominal aortic aneurysms (AAA) are localized dilations of the abdominal aorta (see Figure 1.1) which can rupture if equilibrium between artery resistance and blood pressure is lost. AAA prevalence could reach 8.9% among men and 2.2% among women. It is the 15^{th} leading cause of death in the USA for people over 65 [KMY13]. AAA risk factors are typically the same as for atherosclerosis, i.e., gender (male), smoking, age, hypertension and hyperlipidemia [McG11] but genetic factors are also believed to contribute to AAA development, growth and rupture.

If the human scale, the AAA is defined by the enlargement of the vascular wall, it can also be defined pathophysiologically. The breakdown of the extracellular matrix thanks to an excessive proteolytic activity, especially metalloproteinases (MMPs) [BAZM80].

AAA are usually asymptomatic and therefore often detected through unrelated examinations or dedicated screenings, such as ultrasound or computed tomography (CT-scan) examinations. Once detected, AAA risk assessment is generally based on the measurement of its maximal diameter (D_{max} criterion). Patients will undergo open or endovascular aneurysm repair (see Figure 1.2) if D_{max} is over a statistically-based threshold: 55 mm for

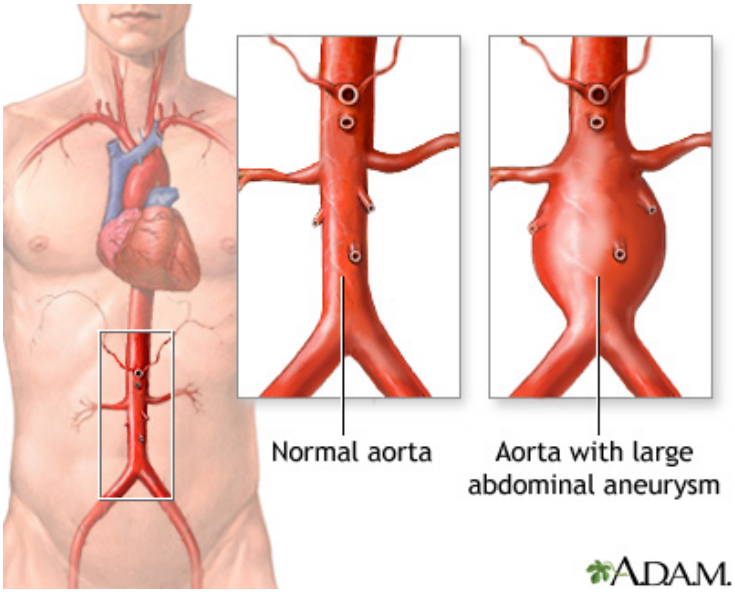

(a)

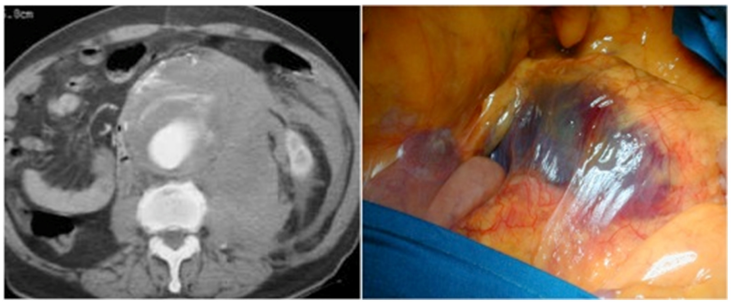

(b)

Figure 1.1 – a) Visualization of the localization of the AAA and the difference with a normal aorta. Source: https://www.adam.com/ b) Axial slice from CT-scan and view during surgery or a ruptured AAA. Images source : [Ant11]

men and 45-50 for women and grows of more than $10\,\mathrm{mm\,yr^{-1}}$ [PFL+15, CBD+09].

However, D_{max} is an imperfect criterion as the estimated annual rupture rate of 4.0 to 4.9 cm AAA, is non-negligible (1.0% per year) [PFL+15] and 23% of ruptured AAA are less than 5 cm [DMBO77]. In contrast, rupture rate in large aneurysms could be lower than expected with annual rupture rate of 3.5% for 5.5 to 6 cm and 4.1% in 6 to 7 cm AAAs [PFL+15]. These data show the maximal diameter to rupture relationship to be nonlinear and inaccurate to predict rupture. To overcome these limitations, new metrics have been introduced for better AAA-rupture risk assessment.

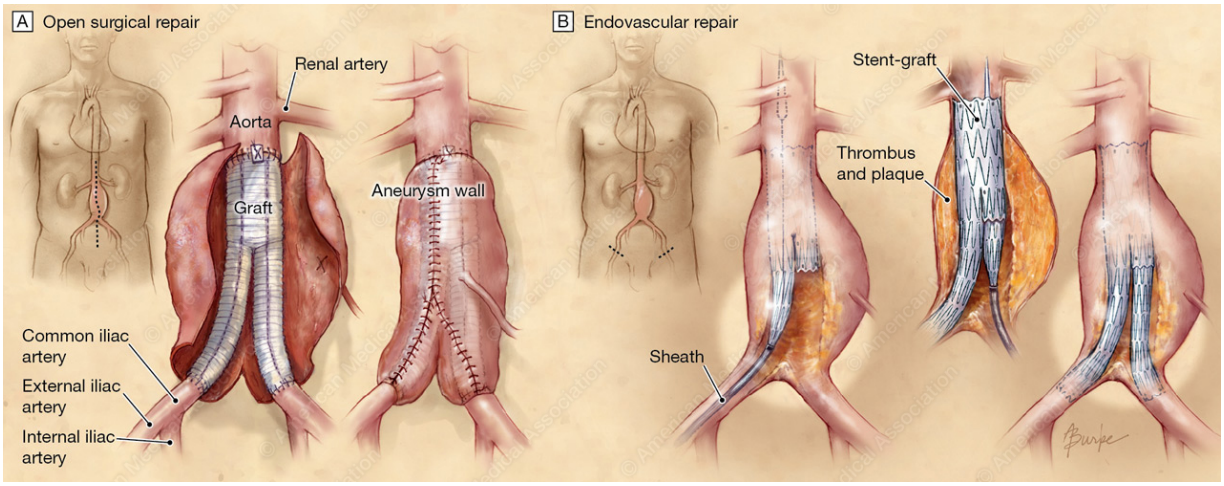

Figure 1.2 – Visual comparison between open surgical repair (left) and endovascular repair (right). Source: http://www.alison-burke.com

1.2 Morphological and hemodynamic risk metrics: previous studies

Some morphological features with known relationship to AAA rupture risk are, indeed, volume, surface, bulge height, tortuosity and local surface curvature [RKCdT+06, SMDM+11]. Besides the above geometric attributes, mechanical wall stresses in AAAs depend upon tissue properties, which are essentially heterogeneous and nonlinear and patient specific [RKCdT+06, WVDA+13]. As it is impossible to fully characterize such properties as well as complex micro to macro-scale interconnections, handling generalized numerical models for rupture risk prediction becomes difficult.

The expanding accessibility of patient-explicit 3-D AAA models from computed tomography angiography (CTA) now makes individualized hemodynamic investigations conceivable, with flow simulation, fluid-solid interaction and multiphysics modeling. The latter couples mechanics with biology, enabling, for example, simplified simulations of AAA growth by replicating the evolution of wall composition and rheology.

Blood flow and its altered topology are known to play a key role in both wall-fluid shearing action and transport perturbations in AAA evolution. Very few studies focus on local parameters and their variations between two scans. [TKM+17] observed a relationship between ILT growth and TAWSS and OSI but not with RRT on six AAA

while [ASDS14] noticed in ten AAAs a significant relationship between ILT deposition and high OSI but not with low TAWSS. Both studies included small AAA (D_{max} <53 and <50 mm respectively). [ZGL+16] observed a relationship between low WSS and the ILT deposition locations. Furthermore on their 14 patients, ILT volume accumulation was correlated with the AAA growth. The investigation of the hemodynamic mechanisms underlying AAA expansion is a promising approach to understand and potentially provide more patient-specific tools to characterize AAA vulnerability. The goal of this work is to explore the potential dependence between computed hemodynamic factors and morphological patterns of AAAs on a large longitudinal study. More specifically, several global as well as local metrics were computed for 32 AAA patients (in a total of 129 scans) and compared to 9 healthy patients. A large number of morphological and CFD-based hemodynamics parameters were studied. Classification of patients and parameter correlations were performed based on machine learning tools to understand and predict AAA growth.

Rationale

A better understanding of the underlying mechanisms of AAA growth can lead to the creation of improved patient care.

Goal of this study

- Extract characteristic metrics of the flow alteration
- Evaluate relationships between those metrics and AAA growth
- Build a predictive growth model

Working hypothesis

- Flow alteration is a key contributor to AAA growth
- The ability to predict the evolution (D_{max}^{t+1} and ΔD_{max}) corresponds to the expectation of physicians to make a treatment decision

1.3 Advanced flow structures extraction

The concept of Lagrangian Coherent Structures (LCS) is an efficient way of characterizing transport in complex fluid flow. To cite [PH13], the LCS approach is a mean of identifying key material lines that organize fluid-flow transport. LCS form separatrice surfaces, which divide the domain into dynamically-isolated regions and reveal the hidden flow skeleton. LCS defining Lagrangian jet cores [Hal11] can be extracted from maxima ridges in the so-called finite-time Lyapunov exponent (FTLE) scalar field. FTLE quantifies the rate of stretching between flow trajectories integrated over time. Previous studies [AS12, ADES12, ST08] have shown that extraction of LCS from the FTLE field allows the observation of blood flow transport over a complete cardiac cycle from an Eulerian point of view (see Figure 1.3 for a comparison of forward and backward integration with the flow residence time). If FTLE are an efficient tool for structures extraction, other Lagrangian-based quantities may serve as support for LCS definition [HFB+17] but no comparison where performed on physiological flows, to the authors knowledge. The existence of extensive literature on vorticity in AAAs [JSR07, MGM+11, She09], the presumed role of vortical structures in platelet activation [BHCG11] makes the Lagrangian-Averaged Vorticity Deviation (LAVD) which integrates the vorticity deviation with the local average along the flow trajectories [HHFH16] particularly appropriate for this study.

1.4 Thesis structure and objectives

This thesis is organized around three chapters followed by their respective bibliography, each dedicated to one aspect of the AAA growth understanding and metrics investigation. The first chapter is a published article and thus follows the journal structure; the two following chapters have not yet been published but are organized in a similar fashion.

We now present for each chapter, its specific objective and associated main approach.

1 **Faced with the existence of numerous morphological and hemodynamic alteration metrics evaluated on small cohorts, the goal of this study was**

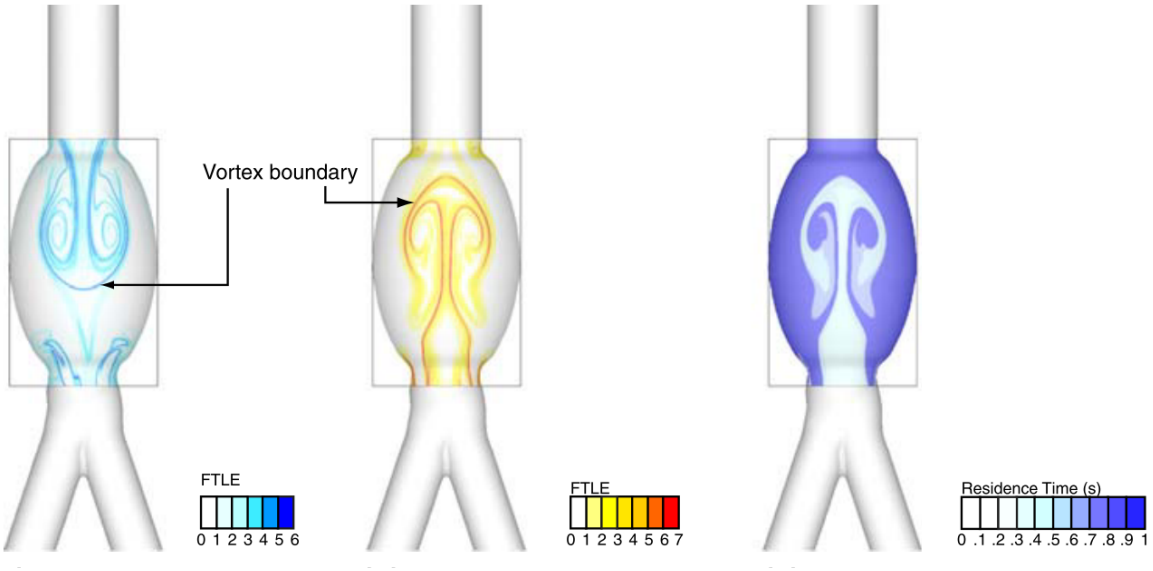

Figure 1.3 – Visualisation of flow transport in an idealized AAA. Left: backward time FTLE, center: forward time FTLE and right: residence time. Reproduced from [ST08].

1) to assess their relationship to AAA growth and 2) build a predictor from those with a better predictive power than the existing criteria.

In chapter 2, a database of thirty-two patients with AAA was built. Each patient is monitored as long as their state is not critical and does not require repair and undergo regular CT-scans. One of the criteria was the presence of at least 3 follow-up scans for each of them, thus giving 129 exploitable AAA scans in total. In addition to those, nine age and sex matched patients without AAA where included as baseline. Those CT-scans were segmented, blood flow simulations were carried and results were post-processed. Clinical (age, sex, smoking...), morphological (tortuosity, shape, ILT) and hemodynamic metrics were confronted to the growth speed of AAA. The population was split into healthy, low risk and high risk groups and the ability of each metric to stratify the population was reported. One major part of the work was the evaluation of local correlations between flow topology and growth metrics. Despite no significant results in terms of diagnosis, the heterogeneity of AAA was highlighted. Then each AAA feature and outcome, i.e. if the AAA will be at risk at the next step or not, were

incorporated into a prediction model. Neural networks were used for each category of metrics and compared to the reference, the D_{max}. Despite the heterogeneities previously pointed out, the specificity and sensitivity of the new predictor based on hemodynamic and/or morphological features significantly exceeded the D_{max}. The potential of learning algorithm based on a composition of patient specific features was demonstrated and could become a clinical diagnostic tool.

2 **Transport alteration in AAA is challenging due to the nature of the flow itself but is presumed to play a key role in ILT deposition and AAA growth. The objective of this study is the extraction of the Lagrangian Coherent Structure – the hidden skeleton of the flow – in an AAA followed for 8 years.**

While in the previous study the focus was the influence of blood flow on the AAA in terms of wall fields, in chapter 3 a quantitative metric of transport alteration was built and evaluated. For that, a patient followed eight years with nine CT-scans was selected. All lumen and ILT were segmented and blood flow was simulated. Observing flow transport in a time-dependent flow is challenging and most metrics do not account for the transient phenomena. Finite-Time Lyapunov Exponents measure the rate of stretch between adjacent flow particles to reveal the hidden characteristics and material frontier in the flow. Those frontiers are one method to extract the Lagrangian Coherent Structures of the flow that separate dynamically isolated zones. ILT deposition could trigger platelet activation and adhesion which are linked to AAA growth. LCS provide two crucial piece of information: frontiers are subjected to high shear, or platelet activation zones, and separation of the domain into regions with different dynamics. For this specific patient, three regions would stand out: two in the bulges of the AAA and a tubular zone connecting the proximal to the distal neck. The volume and relative volumes of each region were plotted alongside the lumen and total volume of the AAA to observe potential relationships.

3 **The objective of this chapter was the evaluation of a novel technique for LCS extraction, based on the Lagrangian-Averaged Vorticity Deviation on AAA of various shape and compared to the results of vorticity.**

The previous chapter described an innovative method for dividing the flow domain into dynamically isolated zones. However, this method did not transpose well to the diversity of AAA encountered in real life, either because of intrinsic limitations of the method or the absence of clearly separated regions of the flow. Vorticity was at the core of chapter 4. First, on a selection of five patients, vorticity was computed, discussed and compared with the literature before testing a promising Lagrangian approach, the LAVD. Unlike the FTLE, where a function of the local stretching is advected along the flow trajectories, an objective variation of the vorticity, the Instantaneous Vorticity Deviation (IVD), is transported. Globally, if the vortical structures (VS) of the flow are captured in a single time frame, LCS could not be successfully extracted. Several causes are considered, from the complexity of the flow where organized VSs of interest exist only during a small time window of the cardiac pulse, rendering the method unsuited for this context or suboptimized computational parameters.

The manuscript ends with a main conclusion on the work performed in this thesis. A bibliography is given at the end of each chapter.

BIBLIOGRAPHY

ADES12. Amirhossein Arzani, Petter Dyverfeldt, Tino Ebbers, and Shawn C. Shadden. In vivo validation of numerical prediction for turbulence intensity in an aortic coarctation. *Annals of Biomedical Engineering*, 40(4):860–870, 2012.

Ant11. M Antonello. *Diagnosis, Screening and Treatment of Abdominal, Thoracoabdominal and Thoracic Aortic Aneurysms*. InTech, 9 2011.

AS12. Amirhossein Arzani and Shawn C. Shadden. Characterization of the transport topology in patient-specific abdominal aortic aneurysm models. *Physics of Fluids*, 24(8):81901, 8 2012.

ASDS14. Amirhossein Arzani, Ga-Young Suh, Ronald L. Dalman, and Shawn C. Shadden. A longitudinal comparison of hemodynamics and intraluminal thrombus deposition in abdominal aortic aneurysms. *American Journal of Physiology-Heart and Circulatory Physiology*, 307(12):H1786–H1795, 12 2014.

BAZM80. Ronald W. Busuttil, A. M. Abou Zamzam, and Herbert I. Machleder. Collagenase Activity of the Human Aorta: A Comparison of Patients With and Without Abdominal Aortic Aneurysms. *Archives of Surgery*, 115(11):1373–1378, 1980.

BHCG11. Jacopo Biasetti, Fazle Hussain, and T. Christian Gasser. Blood flow and coherent vortices in the normal and aneurysmatic aortas: A fluid dynamical approach to intraluminal thrombus formation. *Journal of the Royal Society Interface*, 8(63):1449–1461, 10 2011.

CBD+09. Elliot L. Chaikof, David C. Brewster, Ronald L. Dalman, Michel S. Makaroun, Karl A. Illig, Gregorio A. Sicard, Carlos H. Timaran, Gilbert R. Upchurch, and Frank J. Veith. The care of patients with an abdominal aortic

aneurysm: The Society for Vascular Surgery practice guidelines. *Journal of Vascular Surgery*, 50(4):S2–S49, 2009.

DMBO77. R C Darling, C R Messina, D C Brewster, and L W Ottinger. Autopsy study of unoperated abdominal aortic aneurysms. The case for early resection. *Circulation*, 56(3 Suppl):161–4, 9 1977.

Hal11. George Haller. A variational theory of hyperbolic Lagrangian Coherent Structures. *Physica D: Nonlinear Phenomena*, 240(7):574–598, 2011.

HFB+17. Alireza Hadjighasem, Mohammad Farazmand, Daniel Blazevski, Gary Froyland, and George Haller. A critical comparison of Lagrangian methods for coherent structure detection. *Chaos*, 27(5):053104, 5 2017.

HHFH16. G. Haller, A. Hadjighasem, M. Farazmand, and F. Huhn. Defining coherent vortices objectively from the vorticity. *Journal of Fluid Mechanics*, 795:136–173, 2016.

JSR07. R a Jamison, G J Sheard, and K Ryan. Non-axisymmetric flow development in pulsatile blood flow through an aneurysm. In *16th Australasian Fluid Mechanics Conference AFMC*, number December, pages 353–360, Gold Coast, QLD, Australia, 2007.

KMY13. Koji Kurosawa, Jon S Matsumura, and Dai Yamanouchi. Current Status of Medical Treatment for Abdominal Aortic Aneurysm. *Circulation Journal*, 2013.

McG11. Tim M McGloughlin. *Biomechanics and Mechanobiology of Aneurysms*, volume 7 of *Studies in Mechanobiology, Tissue Engineering and Biomaterials*. Springer Berlin Heidelberg, Berlin, Heidelberg, 2011.

MGM+11. Umberto Morbiducci, Diego Gallo, Diana Massai, Raffaele Ponzini, Marco A. Deriu, Luca Antiga, Alberto Redaelli, and Franco M. Montevecchi. On the

importance of blood rheology for bulk flow in hemodynamic models of the carotid bifurcation. *Journal of Biomechanics*, 44(13):2427–2438, 9 2011.

PFL+15. Fran Parkinson, Stuart Ferguson, Peter Lewis, Ian M. Williams, Christopher P. Twine, and South East Wales Vascular Network. Rupture rates of untreated large abdominal aortic aneurysms in patients unfit for elective repair. *Journal of Vascular Surgery*, 61(6):1606–1612, 6 2015.

PH13. Thomas Peacock and George Haller. Lagrangian coherent structures: The hidden skeleton of fluid flows. *Physics Today*, 66(2):41–47, 2013.

RKCdT+06. Madhavan L. Raghavan, Jarin Kratzberg, E. M. Castro de Tolosa, Mauro M. Hanaoka, Patricia Walker, Erasmo Simão da Silva, Erasmo Magalhães Castro de Tolosa, Mauro M. Hanaoka, Patricia Walker, and Erasmo Simão da Silva. Regional distribution of wall thickness and failure properties of human abdominal aortic aneurysm. *J Biomech*, 39(16):3010–3016, 2006.

She09. Gregory J. Sheard. Flow dynamics and wall shear-stress variation in a fusiform aneurysm. *Journal of Engineering Mathematics*, 64(4):379–390, 2009.

SMDM+11. Judy Shum, Giampaolo Martufi, Elena Di Martino, Christopher B. Washington, Joseph Grisafi, Satish C. Muluk, Ender A. Finol, Elena Di Martino, Christopher B. Washington, Joseph Grisafi, Satish C. Muluk, and Ender A. Finol. Quantitative assessment of abdominal aortic aneurysm geometry. *Annals of Biomedical Engineering*, 39(1):277–286, 1 2011.

ST08. Shawn C. Shadden and Charles A. Taylor. Characterization of coherent structures in the cardiovascular system. *Annals of Biomedical Engineering*, 36(7):1152–1162, 7 2008.

TKM+17. Konstantinos Tzirakis, Yiannis Kamarianakis, Eleni Metaxa, Nikolaos Kontopodis, Christos V. Ioannou, and Yannis Papaharilaou. A robust approach for exploring hemodynamics and thrombus growth associations in abdominal aortic aneurysms. *Medical and Biological Engineering and Computing*, 55(8):1493–1506, 2017.

WVDA+13. J. S. Wilson, L. Virag, P. Di Achille, I. Karšaj, and J. D. Humphrey. Biochemomechanics of Intraluminal Thrombus in Abdominal Aortic Aneurysms. *Journal of Biomechanical Engineering*, 135(2):021011, 2 2013.

ZGL+16. Byron A. Zambrano, Hamidreza Gharahi, ChaeYoung Young Lim, Farhad A. Jaberi, Jongeun Choi, Whal Lee, and Seungik Baek. Association of Intraluminal Thrombus, Hemodynamic Forces, and Abdominal Aortic Aneurysm Expansion Using Longitudinal CT Images. *Annals of Biomedical Engineering*, 44(5):1502–1514, 5 2016.

CHAPTER 2

A cohort longitudinal study identifies morphology and hemodynamics predictors of abdominal aortic aneurysm growth

Abstract

ABDOMINAL aortic aneurysms (AAA) are localized, commonly occurring aortic dilations. Following rupture only immediate treatment can prevent morbidity and mortality. AAA maximal diameter and growth are the current metrics to evaluate the associated risk and plan intervention. Although these criteria alone lack patient specificity, predicting their evolution would improve clinical decision. If the disease is known to be associated with altered morphology and blood flow, intraluminal thrombus deposit and clinical symptoms, the growth mechanisms are yet to be fully understood. In this retrospective longitudinal study of 138 scans, morphological analysis and blood flow simulations for 32 patients with clinically diagnosed AAAs and several follow-up CT-scans, are performed and compared to 9 control subjects. Several metrics stratify patients between healthy, low and high risk groups. Local correlations between hemodynamic metrics and AAA growth are also explored but due to their high inter-patient variability, do not explain

AAA heterogeneous growth. Finally, high-risk predictors trained with successively clinical, morphological, hemodynamic and all data, and their link to the AAA evolution are built from supervise learning. Predictive performance is high for morphological, hemodynamic and all data, in contrast to clinical data. The morphology-based predictor exhibits an interesting effort-predictability tradeoff to be validated for clinical translation.

keywords: abdominal aortic aneurysm; growth; CFD (Computational Fluid Dynamics); haemodynamics; ILT (Intra-Luminal Thrombus); longitudinal study; risk prediction; supervised learning; wall shear stress

2.1 Introduction

Abdominal aortic aneurysms (AAA) are local dilations of the abdominal aorta which can rupture blood pressure overcomes artery wall resistance. Following rupture only urgent treatment can prevent morbidity and mortality. It is the 14^{th} leading cause of death in the USA [BSTM90] with a prevalence of 8.9% for men and 2.2% for women.

AAA are generally asymptomatic and generally detected through unrelated examinations. Risk is assessed using its maximal diameter (D_{max}) [OGD+92], taken at the outer wall of the aneurysm on a plane perpendicular to the lumen centerline [CBH+02]. It includes the lumen, the Intra Luminal Thrombus (ILT) and the arterial wall whose diameter cannot be distinguish on CT-scans. If the D_max exceeds a statistically-based threshold of 55 mm for men and 45-50 for women [BCH+03] or if AAA D_{max} growth exceeds $1 \mathrm{cm yr}^{-1}$ [CBD+09], patients will undergo open or endovascular aneurysm repair. Otherwise a yearly control is performed.

New guidelines [CDE+18] define a more complex follow-up and repair decision process, highlighting the difficulty to predict AAA evolution based on its current diameter. D_{max} is an imperfect criterion as the estimated annual rupture rate of 4.0 to 4.9 cm AAA, is non-negligible (1.0% per year) [PFL+15] and 23% of ruptured AAA are less than 5 cm [DMBO77]. In contrast, rupture rate in large aneurysms could be lower than expected with annual rupture rate of 3.5% for 5.5 to 6 cm and 4.1% in 6 to 7 cm AAAs [PFL+15]. These data show the maximal diameter/rupture relationship to be nonlinear and inaccurate to predict rupture [FA01]. Identifying better performing metrics is an active research field [JSG+18]. Risk-linked predictors are usually based on geometric shape, mechanical tissue properties and flow topology thanks to the increased availability of patient-specific 3D AAA models from computed tomography angiography (CTA). Several fields can even be combined in multi-physics and multi-scale modelling makes possible simulations of AAA growth [GWH15, WS15] by coupling the biology and mechanics of the disease. Known metrics of interests are AAA volume, surface, bulge height, tortuosity and local surface

curvature [SMDM+11, SXCF11] as well as mechanical stress, intrinsicly relying on tissue properties, strongly heterogeneous and nonlinear [RKCdT+06] and also patient specific [RMP+13]. From a fluid point of view, blood flow is known to play a crucial role in in AAA evolution [SH13, BKHF11], as well as ILT presence and growth [HCC+18, BAH18].

Blood flow and its altered topology are known to play a key role in both wall-fluid shearing action and transport perturbations in AAA evolution [SH13, BKHF11], as well as ILT presence and growth [HCC+18, BAH18]. Very few studies focus on local parameters and their variations between two scans. Tzirakis et al. [TKM+17] observed on six AAA, a relationship between ILT growth and Time Average Wall Shear Stress (TAWSS) and Oscillatory Shear Index (OSI) but not with Relative Residence Time (RRT), while Arzani et al. [ASDS14b] noticed in ten AAAs a significant relationship between ILT deposition and high OSI but not with low TAWSS. Both studies included small AAA ($D_{max} < 53$ and < 50 mm respectively). Zambrano et al.[ZGL+16] observed a relationship between low Wall Shear Stress (WSS) and the ILT deposition locations. Furthermore on their 14 patients, ILT volume accumulation correlated with the AAA growth. The investigation of the hemodynamic mechanisms underlying AAA expansion is a promising approach to understand, and potentially provide more patient-specific tools to characterize, AAA vulnerability. From a solid mechanics point of view, Martufi et al. [MLLS+16] found that ILT thickness and wall stress were linked to the local growth rate.

In summary, although repair criteria alone lack patient specificity, predicting their evolution would improve clinical decision for follow-up and repair. If the disease is known to be associated with altered morphology and blood flow, intraluminal thrombus deposit and clinical symptoms, the growth mechanisms are yet to be fully understood. The goal of this work is thus to better understand AAA evolution by exploring the potential dependence between computed hemodynamics factors and morphological metrics of AAA growth on a larger longitudinal study. In this retrospective longitudinal study of 138 scans, morphological analysis and blood flow simulations for 32 patients with clinically diagnosed AAAs and several follow-up CT-scans, are performed and compared to 9 control

subjects. First, the definition of a healthy group, versus low and high risk groups in terms of AAA evolution is motivated. The methods also explain the geometrical and blood flow numerical models, and define their postprocessing into global and local metrics. Global parameters distinguishing the different groups are explored, followed by local correlations between hemodynamic metrics and AAA growth. Finally, high-risk predictors trained with successively clinical, morphological, hemodynamic and all data, and their link to the AAA evolution are built from supervise learning. A schematic representation of the article structure is presented in Figure 2.1.

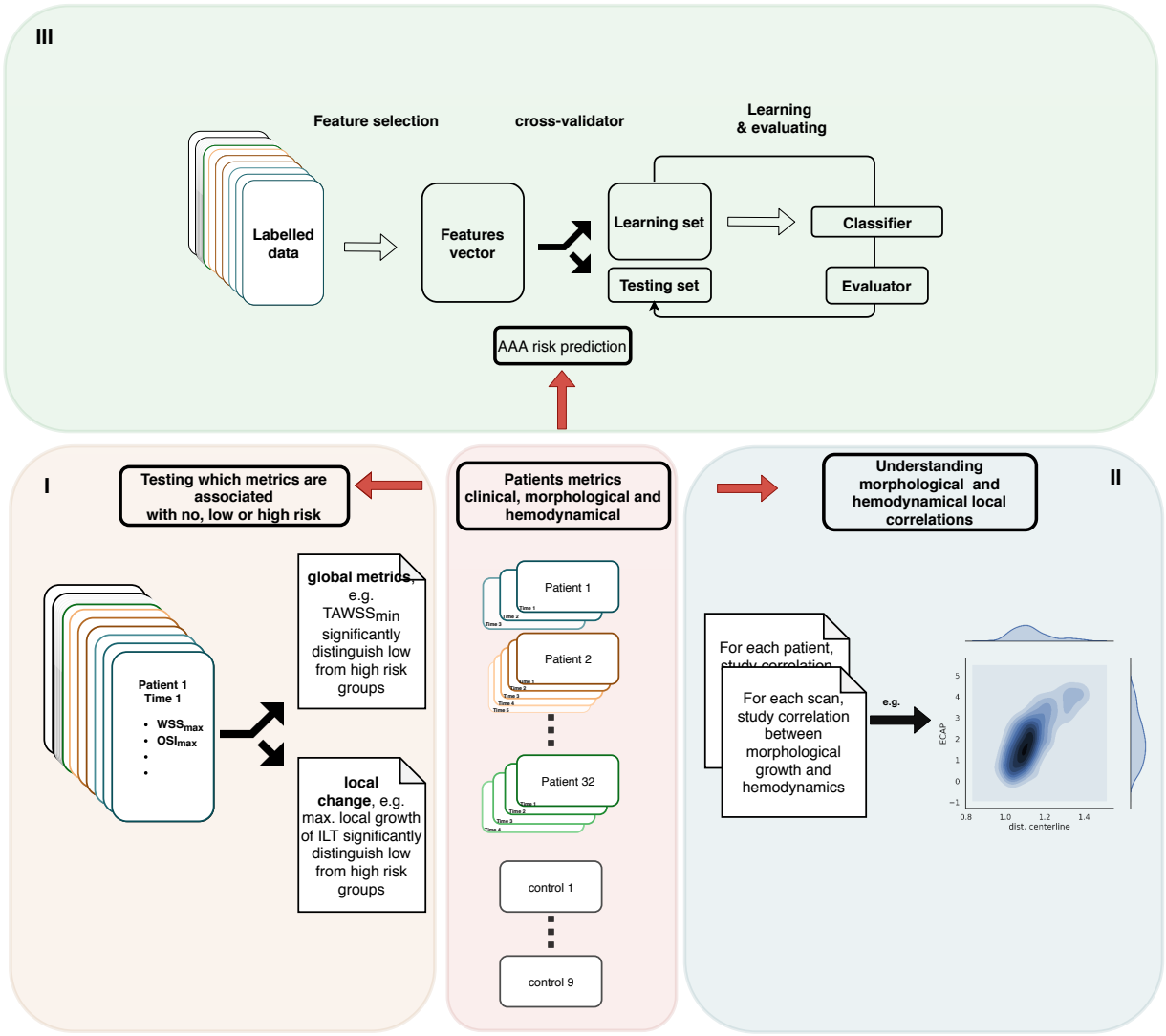

Figure 2.1 – Overview of the study.

2.2 Materials and Methods

This section first describes the patient population and associated definitions. Next, the geometrical model construction and blood flow simulation set-up are explained. Finally, postprocessing of geometry and CFD results is detailed, defining global and local metrics associated with each scan, along with the statistical analysis methods used in this study.

2.2.1 Patient population and associated definitions

This study is HIPAA (Health Insurance Portability and Accountability Act) compliant and approved by the local institutional review board (IRB). Since all data were anonymized, the consent form was waived by the IRB [1] for all patients. Forty-one patients are included in the study, thirty-two with diagnosed AAA and nine healthy. Patients are considered healthy in the absence of AAA ($D_{max} < 30$ mm) and significant arterial disease. They necessitated an abdominal scanner but without peripheral disease, were above 48 year old and were sex-matched with the AAA patients. AAA patients were selected from a clinical data base of patients having CT follow-up for AAA in our institution. The inclusion criteria for AAA patients were: **1**. AAA of more than 30 mm, **2**. At least one baseline CT and 2 following CT scan examinations, **3**. All selected CT scans were acquired with contrast injections and with a slice thickness of less than 2.5 mm in order to ensure accurate and efficient segmentation of the lumen and ILT.

This retrospective study does not include ruptured AAA. Usually patients with ruptured AAA are rarely followed by CT-scan as AAA is usually undiagnosed in such cases. Moreover the AAA size (D_{max}) can be influenced by AAA deflation following rupture and AAA outer wall is more difficult to evaluate in presence of a periaortic hematoma. D_{max} value and growth are therefore combined as a surrogate risk metric.

The AAA population is classified in high and low-risk populations based on the recognized criteria of AAA size and growth over time (D_{max} and D_{max} growth). The commonly

1. Approval #12.153 from the research ethics committee of the University of Montreal Health Centre (CHUM)

used clinical thresholds to indicate an open or endovascular surgery are a D_{max} of 55 mm for male and 45-50 mm for women and a growth of more than 5mm in 6 months [CBD+09]. New guidelines [CDE+18] temper these thresholds, indicating the need for more personalized approaches. There is less consensus on the growth threshold. Growth rate has been reported to be around $2\text{mm}\,\text{yr}^{-1}$ [BTF+04, SSWJ]. The 5mm/year growth threshold has previously been recognized as a fast growth criterion [DWMY14] and this growth variation is above the 95% of the confidence interval of D_{max} measurement error [SKS00]. To define high risk at scan time n, we thus choose 'either D^n_{max} is over 50mm for women and 55mm for men, or D_{max} variation ($D^{n+1}_{max} - D^n_{max}$ between consecutive scans) is under $5\text{mm}\,\text{yr}^{-1}$'.A patient is considered at low risk if he/she is not at high risk Cases are considered as high risk, as soon as one of the high risk criteria is met. For a patient at low risk, if this occurs, the patient switches to high risk for the rest of the follow-up scans.

2.2.2 Geometrical model construction

For all scans, lumens are extracted by an active contour method implemented in *ITK-Snap* [YPH+06]. Aortic models include part of the suprarenal aorta including the ostia of coeliac trunk, mesenteric artery and renal arteries, as well as infrarenal aorta, and internal and external iliac arteries. ILTs are segmented using *ORS Visual* [KTD+11], which is based on active snake segmentation.

2.2.3 Blood flow simulation set-up

The incompressible Navier-Stokes equations are solved in each aortic model as detailed in [JSG+18]. The flow is considered laminar, homogeneous and non-Newtonian, the viscosity following the Quemada model [MGGE+07, MK96]. Model parameters are chosen according to the study of Buchanan et al. [BKC00] based on the rheological data from Kaibara et al. [MK96]. ccPeak Reynolds numbers of 1700-2000 at the proximal inlet in the simulations are within the physiological range [FA01] as well as the Womersley numbers,

ranging from 10 to 15[MMKB94]. A generic flow rate is imposed at the inlet [MGG+70] (see Figure I) with Womersley profile [Wom55]. The aortic wall is considered rigid and a no-slip condition for the blood is imposed on it. Complex recirculation patterns oftentimes exists strecht up to the outlet planes. Additionnaly, reverse flow during diastole [EMBH+11] is likely to create numerical instability. Gradient stabilization to control complex backflow in the domain similarly to Bertoglio et al. [BCB+18] is used. At outlets, a RCR Windkessel model was applied (see Table I in Supplementary materials for parameters value.). The domain is discretized using a polyhedral mesh with refined boundary layers around 0.8-1 million elements (edge length $\approx 0.35mm$), and the Navier-Stokes equations are discretized with finite volume methods (FVM) implemented in the OpenFOAM toolbox. The convective and diffusive term are discretized using a second order Gauss scheme and the time scheme is Crank-Nicholson, also second order[Jas96, JW00]. The solver is a large time-step transient solver for an incompressible fluid for solving pressure–velocity coupling, the PIMPLE (merged PISO-SIMPLE) algorithm. The solution is considered converged if:

- each time steps is fully converged under chosen residuals criteria, i.e. 10^{-6} for pressure and 10^{-8} for velocity; a adaptative time-step was used with the $CFL < 1$ criteria.

- the periodic convergence is achieved, typically after 5-7 cardiac cycles.

- the solution is independent to further mesh refinement, computed using the Grid Convergence Index (GCI)[Roa94]

2.2.4 Definition of global and local metrics

Clinical metrics. The clinical metrics are list in Table 2.II. Their availability among the patient population is reported in the same list.

Lumen centerline and patch description. Most morphological metrics rely on the computation of the centerline of the lumen. The centerline is extracted with *VMTK*, which is based on the Voronoï diagram decomposition of the lumen. The subdomain of interest, i.e. the lumen between the lower renal artery and the iliac bifurcation, is automatically extracted by splitting the surface using the centerline bifurcation information [AEIR03]. It allows a reproducible domain split necessary for surface and volume comparison. Once extracted, the lumen is split along its rotational (24 divisions or 15°) and longitudinal axis, with respect to the centerline curvature (25 divisions), resulting in 600 patches [AS04] (see Figure 2.2). All fields defined on the lumen are averaged on each subdivision. Assuming spatial deformation is spatially homogeneous between acquisitions, each averaged field is compared to its value at the next time step at the estimated same location. Local change is thus computed on a grid-like array : it is the patch-wise variation. The statistical analysis is thus divided in the following manner:

- Unique value for each AAA, (e.g. ILT volume) and their annual variation ; see Table 2.III and Table 2.IV
- Spatially distributed metrics, such as $TAWSS$. First, the distribution information are reported (extrema, average and standard deviations, see Table 2.V) and then the patch-wise annual variation, also reported as extrema, average and standard deviation. For example, the local change of OSI_{max} refers the maximal change of OSI value from one patch at time t to the same patch at time $t+1$. See Table 2.VI and Table 2.VII.

Morphological metrics. To characterize the AAA morphology, we consider (see Table II for definition and references): 1) the maximal lumen diameter D_{max}^{lumen}, computed as the maximal diameter of the AAA luminal sections, defined perpendicular to the lumen centerline, 2) the maximal diameter D_{max} measured at the outer wall, computed normal to the outer wall centerline, 3) the ILT thickness (local and global metric), computed as the

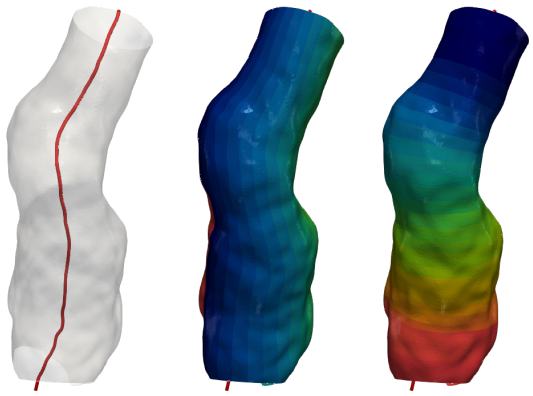

Figure 2.2 – Patching process of the lumen surface. Left: centerline of the vessel lumen, Center: circumferential discretization, colored by the angular index. Right: centerline-based longitudinal discretization colored from top to bottom.

Euclidean distance between the lumen and the outer AAA wall, 4) the lumen centerline curvature, 5) the lumen centerline tortuosity, 6) the Normalized Shape Index (NSI) which characterizes the deviation from a sphere (NSI = 1). A few other metrics are also considered. The lumen surface and volume are defined by the surface area and the volume of the portion of the aortic lumen comprised between the lowest renal and the iliac bifurcation. The ILT volume is also computed for the same region of interest, and the total aortic volume is the sum of lumen and ILT volumes. The ILT coverage is defined as the percentage of the lumen covered with ILT, computed from the number of surface patches on which the average ILT thickness was over one millimetre. The local growth criteria, as defined in the patch-description paragraph, is the ILT thickness change [SGB+17].

Hemodynamics metrics. Finally, to evaluate the flow alteration at the wall, the TAWSS, OSI, RRT and Endothelial Cell Activation Potential (ECAP) are computed from the WSS at the lumen wall (see Table II and Table 2.I), leading to local and global metrics as defined in the patch-description paragraph.

WSS	**Active role** : trigger the mecano-adaptation of the wall **Passive role** : Imprint of flow alteration of the AAA	
TAWSS	Mean over a cardiac period **T** of the WSS	< 0.4 Pa : atherogenic risk > 1.5 Pa : atheroprotective >10-15 Pa : endothelial damage
OSI	Identify regions of oscillating WSS direction	High : perturbed endothelial alignment
RRT	Capture regions of low and oscillatory WSS	Low : atheroprotective High : atherosusceptible
WSSG	Considered as a marker of endothelial cell tension	High : intimal hyperplasia, atherogenic risk
ECAP	Capture endothelial susceptibility	High : risk

Table 2.I – List of relationships between wall fields metrics and the associated AAA risk.

2.2.5 Statistical analysis

Global descriptive statistics. First, descriptive statistics are performed to report population characteristics with a univariate analysis to compare patient populations Figure 2.1I. The population is divided into three groups, as defined in subsection 2.2.1: control cases without AAAs, cases with AAA but considered at low-risk, and cases with AAA at high-risk. Potential correlation between groups for each variable is computed by a Welch's t-test. Similar to the Student's t-test, it accounts for the unequal variance between the samples. Samples are normally distributed as required by the test. In the results, the tables report the lists of variables or global metrics used to describe the AAA and the distribution of their values among the healthy (H), low-risk (LR) and high-risk (HR) patients. For each variable, a Welch's t-test is performed between the healthy and low-risk groups (H-LR), the healthy and low-risk groups (H-HR) and the low-risk and high-risk groups (LR-HR). When significant difference is observed ($p < 0.05$) between two groups, it is reported in the 4^{th} column. Annual variation of hemodynamic parameters and thrombus thickness are computed locally; i.e. patch to patch.

Local descriptive statistics Descriptive statistics are also performed locally (patch-wise) to evaluate the relationships between flow and local morphological metrics Figure 2.1II, in terms of local Euclidean lumen border distance to the centerline (thereafter called 'distance to the centerline'), ILT thickness and patch surface area. Unsupervised outlier detection

is performed on each dataset with the Local Outlier Factor (LOF) method [BKNS00]. As described in Rowland et al. in particular for WSS [RMYC+15], local correlation between a phenomena and a bio-mechanical metric is hindered by spatial auto-correlation. One reported alternative is bootstrapping [ET07] and performing the statistical test on the new dataset. Here, repeating 10000 times the non-parametric Spearman test yields reproducible results. Considering the large amount of data, distribution of Spearman's ρ is reported. Indeed, with a large enough sample size, a very weak correlation can be significant, when the observed effect is likely not real and due to chance in a statistical sense.

Risk predictor methods. Next, we try to anticipate the behaviour of AAA, i.e. to predict the risk based on current information Figure 2.1III. The (predicted) risk criteria is therefore chosen to account for the state after the time evaluated t^n: the D_{max} variation was conserved $((D_{max}^{n+1} - D_{max}^{n})/(t^{n+1} - t^{n}))$ but the D_{max} considered is D_{max}^{n+1}. The thresholds defining low versus high risks are the same as in subsection 2.2.1. To better understand the contribution of the different groups of metrics on risk assessment, the predictor is first build using each set separately, i.e. D_{max} only, clinical, morphological and hemodynamical metrics and they all mixed. The features (input layer) are combined with a neural network to classify whether the next time step is at high-risk or not (output layer). Back-propagation is used to determine weights. Here, a multi-layer perceptron network, implemented in *Theano* [TARA+16] is used. The ten features explaining the most the dataset variance are chosen based on a Principal Components Analysis (PCA). This prevents having too many features compared to the number of samples and the associated risk of overfitting. Hyperparameters are automatically tuned [SDVM+17] to maximize the Area Under the Curve (AUC) of the Receiver Operating Characteristic (ROC) curve and f1-score.

To evaluate the five estimators performance and avoid overfitting, we run repeated k-fold cross correlation with $k = 3$ and 10 repetitions. Features finally selected for each set are reported in Figure 2.8. For clinical interpretation of the results, the ROC curves

with AUC value, and the relative rank of features with respect to the predictability of the target variable evaluated by a multi-class *AdaBoost* [BFKS+11], are reported. AUCs medians are compared with the Delong et al. [DDCP88] method in Table 2.VIII.

2.3 Results

2.3.1 Population description

Healthy population mean age is estimated at 60.4 ± 12.4 years while AAA patient mean age is 73.5 ± 7.4 ($p < 0.05$). Among the AAA patients, 5 are women (15.6%, mean age 73.6 ± 9.4 years) and 27 men (84.4%, mean age 73.5 ± 7.0 years, ($p = 0.98$)) while in the healthy group, one is a woman (11.2%, 78 years) and 8 are men (88.8%, mean age 58.4 ± 11.6 years). At least three follow-up CT-scans are available and suitable for domain reconstruction for AAA patients (mean 4 ± 1.47, range 3-9). Mean time between follow-up CT is 12.74 ± 12.41 months (range : 0.16 to 79.63 months and one case where two CTs were performed on the same day) and the mean follow-up duration is 38.62 ± 22.53 months (range : 6.35 to 111.42 months). Clinical data is available for most patients (see Table 2.II).

Clinical metric	Availability among patients (%)
Age	71.4
Sex	100
BMI	40.5
p_{sys}	61.9
p_{dias}	61.9
Dyslipidemia	69.1
Statins	69.1

Table 2.II – Percentage of the 42 patients for which clinical data are available, per variable. *Age*, *BMI* (body mass index), p_{sys} (systolic pressure) and p_{dias} (diastolic pressure) are continuous variable and *Sex*, *Dyslipidemia* (DLP) and *statins* are discrete.

Regarding the healthy group, D_{max} is 18.2 ± 3.71mm (range: $14.5 - 27.45$mm) whereas in AAA patients D_{max} is estimated 42.68 ± 8.39mm (range: $22.65 - 67.49$mm). At baseline, 7 (21.9%) AAA D_{max} are over the high-risk threshold and 4 (12.5%) have a growth over

$5mm/year$; 2 (6.25%) achieve both. At the last exam, and 16 (50%) are over the high-risk D_{max} threshold and 9 (28.1%) have reached the high-risk growth threshold at the previous follow-up (defined as $D_{max}^{n+1} - D_{max}^{n}$) ; 7 (21.9%) achieve both. The lumen of the healthy aortas are shown in Figure 2.3. Most of them present various degrees of tortuosity, their length increasing with age [XWR+17].

2.3.2 Distribution of clinical, morphological and hemodynamic parameters in the studied population

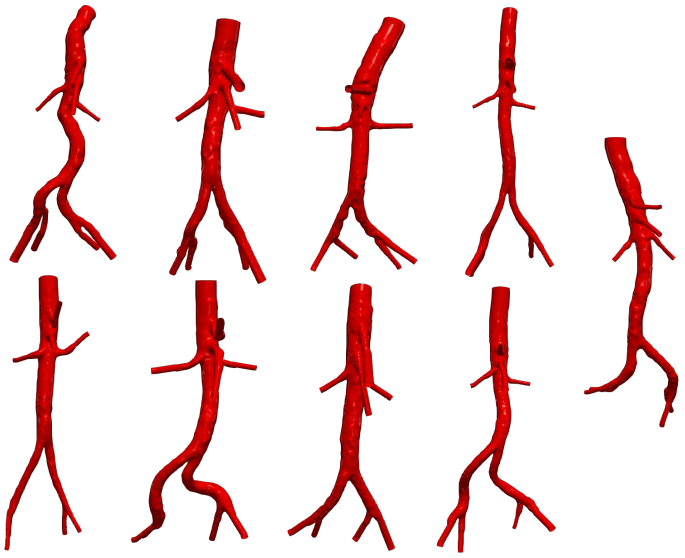

Figure 2.3 – Aorta of the 9 healthy patients included in the study as control subjects. Most present various degrees of tortuosity, due to arteries aging.

This section first studies how metrics associated with the different scans vary among the population and which ones distinguish the different patient groups Figure 2.1I. The distribution of the clinical, morphological and hemodynamic variables among the three groups is presented in tables (Table 2.III, Table 2.IV, Table 2.V,Table 2.VI and Table 2.VII) as well as the correlations between groups for each variable.

139 CT-scans and simulations, from 41 patients, are split into three study groups (healthy (H), low (LR) and high-risk (HR)) as defined in the Methods section. The LR

and HR groups include 59 and 70 cases respectively. Univariate analysis reveals that the D_{max} as well as 10 other variables significantly separate all three groups, some of those being highly correlated, such as volumes and diameters. 18 variables could significantly separate the healthy from the low-risk group, 18 the healthy from the high-risk group, and 27 the low-risk from the high-risk group. For the clinical metrics, all but BMI, separate the groups: pressure for low vs high risks, age, dyslipidemia and statins for healthy vs the other groups. Regarding morphology, all metrics defined for healthy and AAAs can separate the three groups, except for the lumen shape factor (NSI) which separates healthy from AAA but not low-risk from high-risk AAA. Among AAAs, ILT metrics separate low from high risk groups, except ILT coverage and minimum ILT thickness. Regarding annual variations, D_{max} as expected distinguishes the two groups but among all other metrics, only local change of minimum and maximum ILT thickness make that difference, hinting on a particular role of ILT in the local growth process that we will explore in the next section. For all these morphological metrics, significant difference is achieved mostly from mean values but not from their standard deviation (all but the D_{max}). In contrast, for the fluid-based metrics, Table 2.V and Table 2.VII, both average values and standard deviations can discern groups (e.g. the $ECAP_{max}$ and local $ECAP_{max}$ variation). Almost all hemodynamics variables have several metrics that separate healthy from AAAs. $TAWSS_{min}$, RRT_{mean}, $ECAP_{max,mean,stdev}$ further separate low from high-risk groups. Regarding local changes, minimum metrics always separate the two groups, as well as RRT_{max} and $ECAP_{max}$. These results suggest that both instantaneous metric values and their changes are important to understand growth.

In Figure 2.4, the segmented lumen and ILT of two patients during their follow-up are shown. The one on the left shows no major shape change or growth with time, with a fusiform shape and a thin ILT. For the right one, ILT becomes more saccular with time and lumen thinner. This major difference in behaviour is plotted in Figure 2.5 for all patients during their follow-up. D_{max}, D_{max}^{lumen}, lumen tortuosity and shape index plots illustrate the important diversity of the population. The difference between groups is detailed in

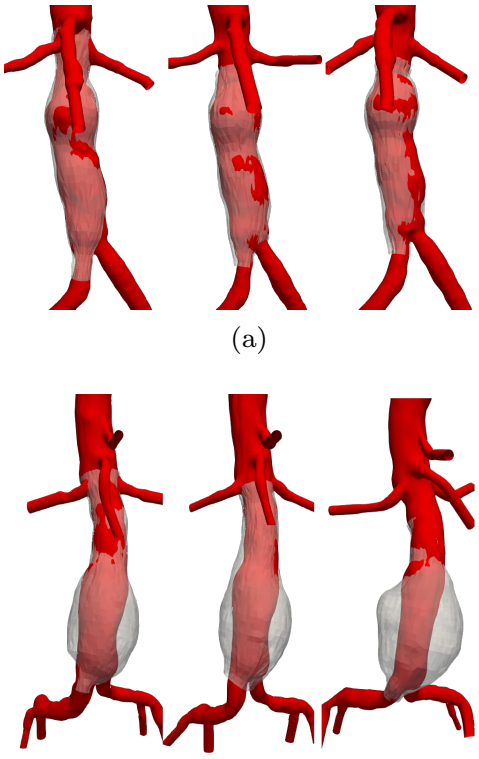

(a)

(b)

Figure 2.4 – Example of different growth dynamics on two patients. The segmented lumen is in red, while ILT is transparent.

Table 2.IV and Table 2.VI.

Next, we present results to understand if there is a local correlation between morphological and hemodynamic metrics that could explain local growth Figure 2.1II. Figure 2.7 describes the correlation coefficients between the wall metrics and two morphological metrics, computed on all patches of each scan : the distance from the lumen wall to the centerline, normalized by the proximal i.e. near the renal arteries distance, and the ILT thickness. There is a large dispersion between patients and scans (see Figure II for the individual data). As a consequence, some exhibit nice correlations (Figure 2.6a), while others do not (Figure 2.6c). The large dispersion of Spearman's ρ distribution is illustrated in Figure 2.6 for one metric. Despite a very large dispersion of data for both the distance to the centerline and the ILT thickness, visible trends stand out (Figure 2.7).

Clinical variables	Healthy	Low-risk	High-risk	Statistical significance
Age (yr)	60.40 (12.44)	73.66 (7.03)	73.88 (7.85)	H-LR, H-HR
Systolic pressure (mmHg)	129.25 (16.89)	119.80 (11.54)	130.73 (17.24)	LR-HR
Diastolic pressure (mmHg)	74.88 (8.67)	68.91 (8.65)	77.21 (13.85)	LR-HR
Dyslipidemia (DLP) (%)	0.33 (0.47)	0.84 (0.37)	0.82 (0.38)	H-LR, H-HR
BMI	25.92 (4.91)	31.20 (5.73)	28.65 (5.95)	
Statins (%)	0.33 (0.47)	0.82 (0.38)	0.80 (0.40)	H-LR, H-HR

Table 2.III – Statistical distribution of the clinical variables among the three groups. When significant difference was observed ($p < 0.05$) between two groups, it was reported in the 4$^{\text{th}}$ column. H-LR means a statistical difference between the High and Low-Risk groups, H-HR between the Healthy and High-Risk groups and LR-HR between the Low and High-Risk groups. Standard deviations are given in parentheses.

Morphological variables	Healthy	Low-risk	High-risk	Statistical significance
Lumen surface area (cm^2)	60.32 (16.93)	98.74 (23.03)	120.90 (27.10)	H-LR, H-HR, LR-HR
Lumen surface area, annual ($cm^2\,yr^{-1}$)	-	6.51 (13.99)	-2.14 (81.85)	
Lumen volume (cm)	24.95 (11.58)	57.17 (20.75)	79.62 (34.28)	H-LR, H-HR, LR-HR
Lumen volume, annual ($cm^3\,yr^{-1}$)	-	6.34 (16.24)	7.43 (80.96)	
ILT volume (cm)	0.00 (0.00)	38.99 (30.80)	65.90 (44.25)	H-LR, H-HR, LR-HR
ILT volume, annual ($cm^3\,yr^{-1}$)	-	3.28 (22.55)	33.95 (154.98)	
Total volume (cm)	24.95 (11.58)	96.17 (41.25)	145.52 (53.53)	H-LR, H-HR, LR-HR
Total volume, annual ($cm^3\,yr^{-1}$)	-	9.38 (14.77)	29.43 (85.82)	
D_{max}^{lumen} (mm)	18.18 (3.52)	28.89 (5.74)	32.94 (8.04)	H-LR, H-HR, LR-HR
D_{max}^{lumen}, annual ($mm\,yr^{-1}$)	-	1.07 (3.85)	2.81 (10.72)	
D_{max} (mm)	18.18 (3.52)	43.72 (7.37)	54.40 (8.77)	H-LR, H-HR, LR-HR
D_{max}, annual ($mm\,yr^{-1}$)	-	1.14 (3.31)	3.61 (4.55)	LR-HR
Lumen NSI (-)	1.22 (0.02)	1.18 (0.04)	1.18 (0.05)	H-LR, H-HR
ILT coverage (%)	-	64.63 (24.92)	67.89 (19.09)	
ILT coverage, annual (yr^{-1})	-	-2.07 (13.06)	33.92 (237.39)	
H_{max}^{ILT} (mm)	-	7.89 (4.12)	11.65 (5.31)	LR-HR
H_{min}^{ILT} (mm)	-	0.31 (0.65)	0.17 (0.46)	
H_{mean}^{ILT} (mm)	-	3.09 (1.80)	4.05 (2.34)	LR-HR
H_{stdev}^{ILT} (mm)	-	2.55 (1.36)	3.71 (1.64)	LR-HR

Table 2.IV – Statistical distribution of the morphological variables among the three groups. When significant difference was observed ($p < 0.05$) between two groups, it was reported in the 4$^{\text{th}}$ column. H-LR means a statistical difference between the High and Low-Risk groups, H-HR between the Healthy and High-Risk groups and LR-HR between the Low and High-Risk groups. Standard deviations are given in parentheses.

hemodynamic variables	Healthy	Low-risk	High-risk	Statistical significance
OSI_{max} (-)	0.36 (0.04)	0.38 (0.04)	0.37 (0.05)	
OSI_{min} (-)	0.02 (0.02)	0.02 (0.02)	0.02 (0.03)	
OSI_{mean} (-)	0.16 (0.04)	0.18 (0.04)	0.17 (0.04)	
OSI_{stdev} (-)	0.11 (0.01)	0.11 (0.01)	0.11 (0.02)	
$TAWSS_{max}$ (Pa)	0.66 (0.31)	0.58 (0.28)	0.54 (0.22)	
$TAWSS_{min}$ (Pa)	0.23 (0.08)	0.11 (0.06)	0.09 (0.05)	H-LR, H-HR, LR-HR
$TAWSS_{mean}$ (Pa)	0.40 (0.17)	0.27 (0.11)	0.23 (0.10)	H-LR, H-HR
$TAWSS_{stdev}$ (Pa)	0.16 (0.09)	0.16 (0.09)	0.16 (0.07)	
$WSSG_{max}$ (Pam^{-1})	135.60 (71.51)	124.55 (70.32)	116.32 (61.23)	
$WSSG_{min}$ (Pam^{-1})	17.42 (9.48)	9.30 (7.30)	6.79 (7.10)	H-LR, H-HR
$WSSG_{mean}$ (Pam^{-1})	61.03 (32.52)	44.74 (25.82)	38.89 (23.32)	
$WSSG_{stdev}$ (Pam^{-1})	61.04 (44.25)	41.97 (24.82)	45.17 (25.02)	
RRT_{max} (Pa^{-1})	22.64 (17.25)	48.26 (30.80)	58.15 (34.73)	H-LR, H-HR
RRT_{min} (Pa^{-1})	2.34 (1.33)	2.63 (1.32)	3.12 (1.84)	
RRT_{mean} (Pa^{-1})	8.20 (6.17)	15.68 (8.01)	19.00 (10.00)	H-LR, H-HR, LR-HR
RRT_{stdev} (Pa^{-1})	8.20 (6.51)	21.68 (16.56)	24.22 (15.69)	H-LR, H-HR
$ECAP_{max}$ (Pa^{-1})	0.66 (0.39)	1.42 (0.76)	1.77 (0.92)	H-LR, H-HR, LR-HR
$ECAP_{min}$ (Pa^{-1})	0.03 (0.03)	0.02 (0.03)	0.04 (0.06)	
$ECAP_{mean}$ (Pa^{-1})	0.26 (0.19)	0.48 (0.22)	0.59 (0.32)	H-LR, H-HR, LR-HR
$ECAP_{stdev}$ (Pa^{-1})	0.20 (0.11)	0.48 (0.27)	0.59 (0.31)	H-LR, H-HR, LR-HR

Table 2.V – Statistical distribution of the hemodynamic variables among the three groups. When significant difference was observed ($p < 0.05$) between two groups, it was reported in the 4$^{\text{th}}$ column. H-LR means a statistical difference between the High and Low-Risk groups, H-HR between the Healthy and High-Risk groups and LR-HR between the Low and High-Risk groups. Standard deviations are given in parentheses.

Local morphological variables	Low-risk	High-risk	Statistical significance
local change of H_{max}^{ILT} (mmyr^{-1})	4.55 (4.27)	7.31 (4.58)	LR-HR
local change of H_{min}^{ILT} (mmyr^{-1})	-4.96 (6.47)	-16.78 (33.77)	LR-HR
local change of H_{mean}^{ILT} (mmyr^{-1})	-0.11 (1.60)	-1.18 (5.38)	

Table 2.VI – Statistical distribution of the local annual variation of ILT thickness among the low and high-risk groups. When significant difference was observed ($p < 0.05$) between two groups, it was reported in the 4$^{\text{th}}$ column. H-LR means a statistical difference between the High and Low-Risk groups, H-HR between the Healthy and High-Risk groups and LR-HR between the Low and High-Risk groups. Standard deviations are given in parentheses.

Local hemodynamic variables	Low-risk	High-risk	Statistical significance
local change of OSI_{max} (yr^{-1})	0.29 (0.41)	1.26 (3.70)	
local change of OSI_{min} (yr^{-1})	-0.29 (0.38)	-1.14 (2.67)	LR-HR
local change of OSI_{mean} (yr^{-1})	0.00 (0.06)	0.05 (0.47)	
local change of $TAWSS_{max}$ ($Pa\,yr^{-1}$)	0.27 (0.36)	1.08 (3.50)	
local change of $TAWSS_{min}$ ($Pa\,yr^{-1}$)	-0.42 (0.70)	-1.47 (3.86)	LR-HR
local change of $TAWSS_{mean}$ ($Pa\,yr^{-1}$)	-0.02 (0.10)	-0.04 (0.25)	
local change of $WSSG_{max}$ ($Pa\,m^{-1}\,yr^{-1}$)	81.56 (108.31)	287.46 (963.86)	
local change of $WSSG_{min}$ ($Pa\,m^{-1}\,yr^{-1}$)	-111.53 (176.19)	-350.49 (829.66)	LR-HR
local change of $WSSG_{mean}$ ($Pa\,m^{-1}\,yr^{-1}$))	-3.86 (24.29)	4.27 (109.43)	
local change of RRT_{max} ($Pa^{-1}\,yr^{-1}$)	44.64 (73.56)	245.22 (658.03)	LR-HR
local change of RRT_{min} ($Pa^{-1}\,yr^{-1}$)	-44.47 (90.49)	-225.57 (538.46)	LR-HR
local change of RRT_{mean} ($Pa^{-1}\,yr^{-1}$)	0.64 (6.76)	8.16 (55.48)	
local change of $ECAP_{max}$ ($Pa^{-1}\,yr^{-1}$)	4.61 (7.11)	23.63 (58.92)	LR-HR
local change of $ECAP_{min}$ ($Pa^{-1}\,yr^{-1}$)	-0.44 (0.56)	-1.85 (3.48)	LR-HR
local change of $ECAP_{mean}$ ($Pa^{-1}\,yr^{-1}$)	1.31 (2.35)	7.39 (21.40)	

Table 2.VII – Statistical distribution of the local hemodynamic variables among the low and high-risk groups. When significant difference was observed ($p < 0.05$) between two groups, it was reported in the 4th column. LR-HR means a statistical difference between the Low and High-Risk groups. Standard deviations are given in parentheses.

TAWSS and WSSG strongly negatively and OSI positively correlate with the centerline distance. Coherently, RRT and ECAP also present strong positive correlation with the distance to the centerline. RRT and TAWSS distributions do not include $\rho = 0$. Regarding ILT thickness, no strong correlation emerges. TAWSS negatively correlates with ILT thickness. This finding is coherent with the common knowledge of low WSS being linked to thrombogenesis. WSSG and OSI also show slightly negative correlation with ILT thickness while no conclusion can be drawn from the RRT and ECAP ρ distributions. In fact, all five hemodynamic metrics ρ distributions are divided between positive and negative values, sign of a great heterogeneity between scans. When the statistics are computed on each patient instead of each scan separately, trends are conserved with however lower dispersions (Figure 2.7, bottom).

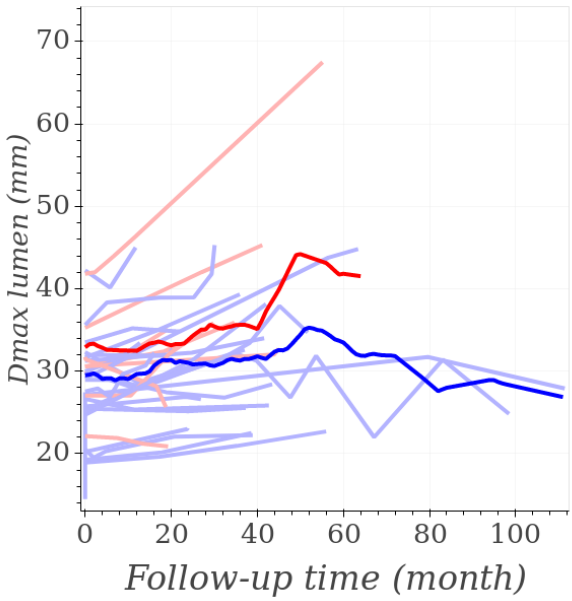

(a) D_{max}^{lumen}

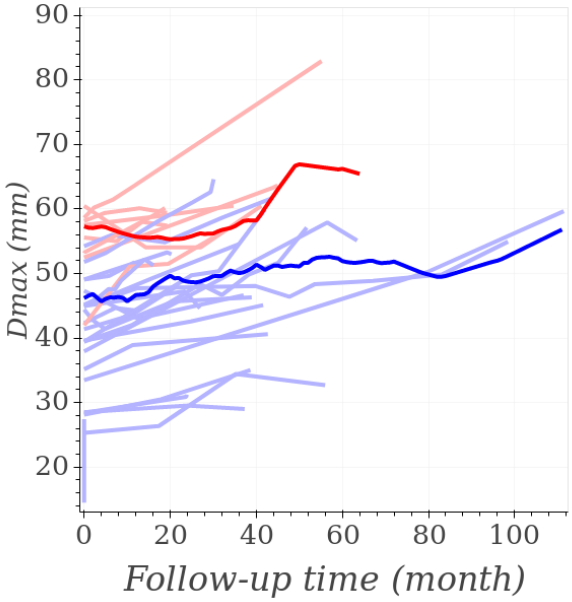

(b) D_{max}

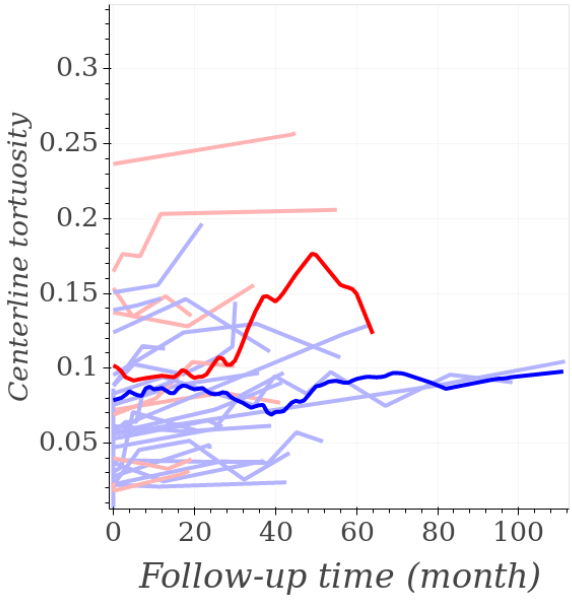

(c) Lumen centerline tortuosity

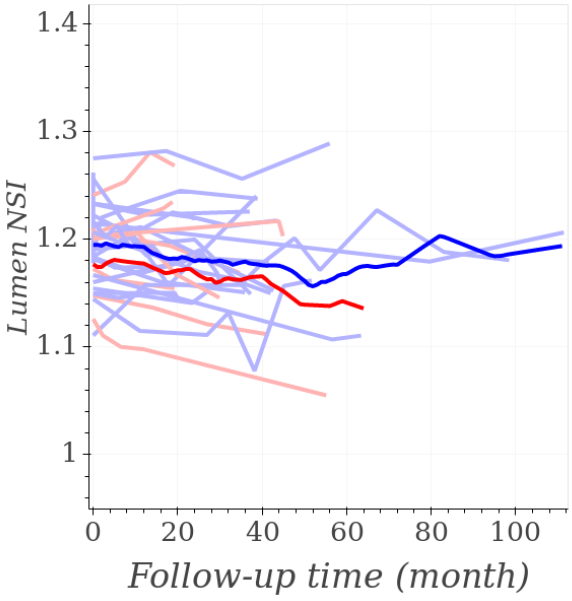

(d) Lumen NSI

Figure 2.5 – Evolution with time of selected parameters among patients. AAA ending up as high-risk are represented by red lines while low-risk AAA are in blue. Averaged behaviours of the two groups are in bold color.

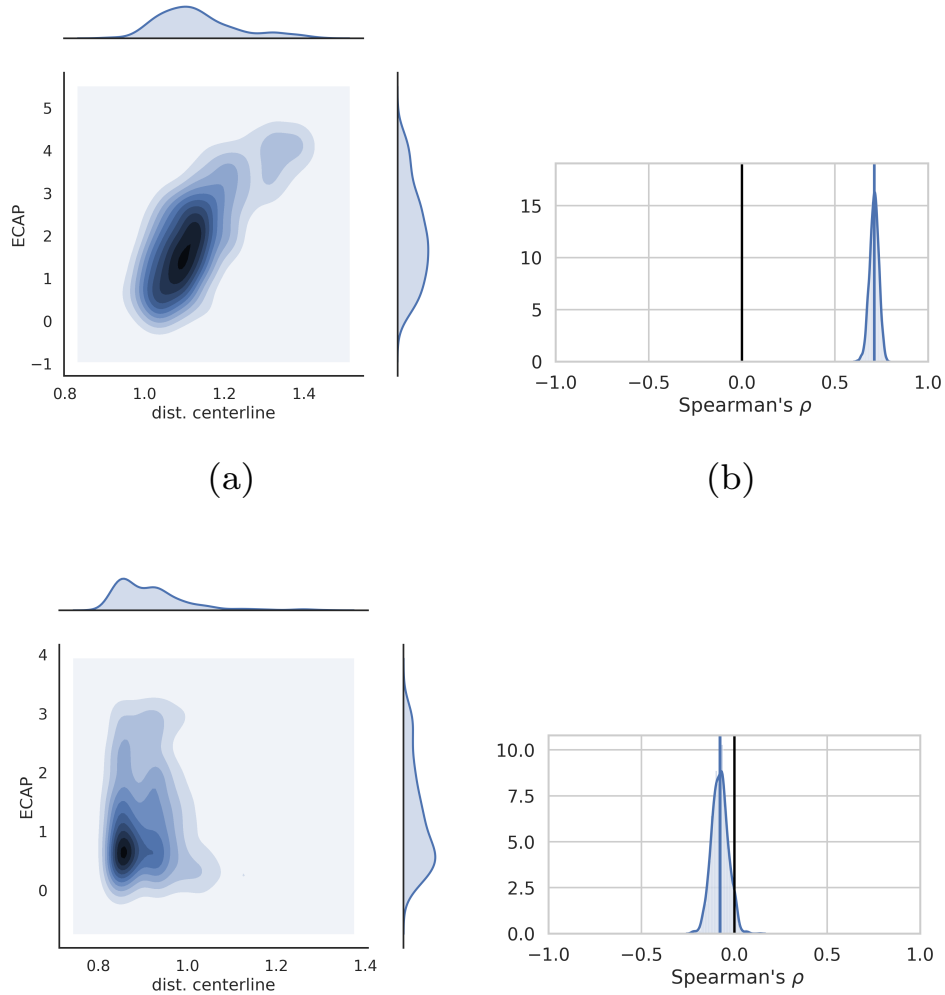

Figure 2.6 – a and c: Bivariate distributions and kernel density plot of ECAP versus the distance from the lumen wall to the centerline of two simulations from two different patients. b and c: Distribution plots of the Spearmans's ρ from the bootstrap evaluations. The top and bottom cases illustrate the variety of the bivariate distributions and correlations encountered in the study.

2.3.3 Global classification as a risk predictor

Finally, we study if the AAA evolution can be predicted (Figure 2.1III). The ability of the classier to discern future high-risks from low-risks cases is presented in Table 2. Recall that this prediction is based on features of the current time. The features are initially

divided into 5 sets: D_{max} only, clinical, morphological and hemodynamic separately and then all features merged. The relative influence of the individual features on the dataset is also plotted for a better understanding of their role.

For reference, the classification is evaluated with D_{max} only and the corresponding AUC is 0.75 ± 0.08. No feature ranking is present as the entire classification information comes from D_{max}. For clinical features alone, the AUC is 0.73 ± 0.09 and the most separating features are age, p_{sys} and p_{dias}. With only morphological features ($D_{max}excluded$), the AUC is 0.93 ± 0.09. The information mostly comes from the lumen centerline curvature, the ILT volume and thickness, and the lumen NSI. Concerning hemodynamic features, the AUC is 0.96 ± 0.10 with information mostly gained from OSI_{mean}, $ECAP_{stdev}$, RRT_{max} and $ECAP_{max}$. Finally, with all features combined, the AUC reaches 0.98 ± 0.06: information is mostly gained from ILT volume, OSI_{max}, OSI_{mean} and $WSSG_{stdev}$. To evaluate the statistical difference between features sets, p-values between AUCs are computed and reported in Table 2.VIII. Significant differences are observed when all the features are compared to a single feature class, and also when the flow features are compared to the D_{max}.

	Dmax	**Clinical**	**Morpho.**	**Flow**	**All**
Dmax		0.393	0.008	0.006	0.006
Clinical			0.004	0.004	0.004
Morpho.				0.561	0.207
Hemo.					0.281
All					

Table 2.VIII – p-values between AUCs from Figure 2.8 according to Delong et al. [DDCP88] method. Significant values (≤ 0.05) are in orange cells.

2.4 Discussion

Quantifying AAA rupture risk has been an active field of research for at least the last decade without dethroning the D_{max} criteria. However, parameters accompanying the disease progression have been observed and discussed, including clinical observation, morphology, structural or fluid analysis and a mix of those. High risk AAA are essentially

either undiagnosed or repaired, hence the scarcity of longitudinal studies with very fast growing aneurysms. If metrics such as WSS or arterial wall solid stress alone cannot specifically single out high-risk aneurysms, their influence on the temporal evolution of AAA may be more relevant [SKS00].

In this work we have attempted to find potential underlying relationships between clinically available variables or computed metrics that quantitatively characterize AAA and their hazardous growth. An AAA is considered at risk after reaching a threshold D_{max} or exceeded a D_{max} monthly variation threshold. If such relationship exists, one can envision a new combination of parameters to be a reliable predictor of an AAA evolution from a single scan, and thereby enhancing the patient-specific decision-making process about increased surveillance or type of treatment.

2.4.1 Descriptive statistics

A total of 129 AAA from 32 patients and 9 healthy aortas were considered. The non-newtonian flow was simulated with FVM including backflow stabilization, and all WSS-based fields and geometrical metrics were discretized on the patch-parameterized AAA lumen. All data were mapped onto the same patch space to be able to compute local time variation of metrics. When exploring the local relationships, i.e. patch-wise, both WSSG and TAWSS negatively strongly and OSI positively correlate with the local distance from the lumen wall to the centerline. This distance is normalized for each scan by the distance at the proximal neck of the AAA. This local distance thus contains information on the local dilation of the AAA, likely creating low TAWSS and high OSI zones. RRT and ECAP, by construction, have an opposite behavior from the OSI and TAWSS. By contrast, it is difficult to conclude for the local relationships with the ILT thickness given the variation among scans. Correlations with the annual variation of the lumen wall distance to the centerline and ILT thickness were not reported, presenting no visible trend. Considering all local variables may not be the appropriate measure to understand local growth. However,

the risk prediction based on hemodynamic features works well (see subsection 2.3.3): mean, extrema or standard deviation of the local metrics seem to be the overall drivers for AAA growth. Nonetheless, previous work, especially Tzirakis et al. [TKM+17] found weak relationship between ILT growth and TAWSS (see Figure 2.7). However, data from their study do not reveal correlation with low OSI as weakly shown in Figure 2.7 and Arzani et al. [ASDS14b] did. TAWSS seemed relevant in both studies as well as in Zambrano et al. [ZGL+16]. These studies considered few patients. To our understanding and as Figure 2.7 illustrates, correlations with local morphological growth are highly heterogeneous among patients, even if for a given patient strong relations can emerge. This behavior prevents emanation of general correlations. Finding a relevant normalization space between all patients may lead to a better understanding of the local growth causes.

Figure 2.5 and Figure II illustrate the variety of situations encountered by clinicians when following an AAA over a given period of time. When all patient data is overlaid, no group separation visibly arises from the curves. However, from Table 2.III to Table 2.VII one can observe that many parameters can separate patients; especially 27 of them can discern the high from the low-risk group. As expected, the classical D_{max} was one of the parameters sensitive enough to discern healthy aortas from low-risk AAAs, and also low from high-risk AAAs. ILT and total volume present the same capacity, as all three are directly linked. Despite the tendency of ILT to fill the AAA cavity, tending to reshape the lumen into a more tubular fashion, Figure 2.5 shows that lumens of AAA at higher risk tend to be more tortuous with a larger D_{max}^{lumen}. At the same time, while for low-risk AAA the D_{max}^{lumen} shows little to no growth, the D_{max} is continuously increasing. A major hypothesis to explain AAA growth is acceleration of the loss of mechanical properties of the aortic wall due to ILT deposition. ILT leads to local wall hypoxia and inflammation [TGP+15], smooth muscle cells apoptosis, elastin degradation and MMP-2 (matrix metalloproteinase-2) concentration. Shifting the pressure load normally mostly borne by elastin cells to collagen fibers contributes to the wall stretching and diameter increase. The shape modification can lead to an increase of the lumen surface prone to ILT deposition,

thus maintaining the vicious cycle. Figure 2.5 could indicate that some AAA could remain at low-risk provided that their lumen keeps its shape and size relatively constant, and the D_{max} growth remains below the repair threshold. This could lead to a better understanding of the difficulty to assess AAA risk, given the presence of patients with large AAAs who will have a lower proportion of rupture than expected [PFL+15] and relatively small aneurysms that rupture [DMBO77].

Currently, sex-adjusted D_{max}, absolute value and progression, is obviously significantly associated with the high risk population. Surprisingly volume and surface progression, despite a theoretically higher sensitivity, were not associated with patient risk. Similarly, no other morphological metrics annual variation could, despite higher theoretical sensitivity such as volume and surface versus diameters. One hypothesis is that the cumulative segmentation error induces a higher variability than the observed growth, especially for slow growing AAAs.

Low TAWSS and high OSI are linked to atheroprone regions of AAAs and predominates at site of rupture [BKLK16]. Di Achille et al. [DATFH14] combined both to form the ECAP. This metric does not offer a mechanistic explanation on ILT deposition but more an imprint on the wall of the near wall flow features that are related to thrombus deposition. Additionally, AAA wall is mostly covered by ILT, and if not, is highly atherosclerotic; therefore seeking metrics related to the wall mechano-adaptation resulting from endothelial cell triggering may not be successful. However, low wall shear can inform about two different phenomena : it is the imprint on the wall of the local flow alteration, and it also favors activated platelets adhesion. As expected, $ECAP_{max}$ and $ECAP_{mean}$ can separate the population but, interestingly, also $ECAP_{stdev}$. Standard deviations were added for all metrics, motivated by the highly patient specific data distribution (see Figure II to Figure V) and can be considered as an indicator of the wall roughness. CT-scan resolution cannot report wall roughness due to atherosclerosis and smoothing prior to meshing removes any small scale perturbation. Nonetheless, larger scale perturbation persists that cannot be explained. Hypotheses include poor segmentation of calcifications, often over-

estimated on CT-scans, contrast inhomogeneity, recurrent in large blood filled cavities such as AAAs or real morphological alteration. Numerically the WSS is computed using the vector normal to the wall, at each cell, and is therefore highly dependent on surface quality. However, because WSS derived metrics allow to statistically separate groups and being visually consistent (e.g. see the ECAP distribution plot in Figure V), we believe the geometrical perturbation is likely of biological origin.

Looking at the local change, i.e. patch-wise, is more challenging. Significant variations of OSI_{min}, $TAWSS_{min}$, $WSSG_{min}$, RRT_{min} and $ECAP_{min}$ are negative and average values are lower for high-risk than for low-risk patients. Whereas for ECAP, mean values increase faster for high-risk AAA while $ECAP_{max}$ is increasing faster but $ECAP_{min}$ is decreasing faster too. This indicates a larger dispersion of the values with time for high-risk AAA than for low-risk AAA, explaining the added value of the standard deviation of variables.

2.4.2 Risk prediction

The classification process aimed at building a risk predictor based on information acquired at a given time to anticipate if the patient will evolve to a high-risk state or stay at low-risk in the foreseeable future. Knowing that many of the evaluated metrics of interest contain powerful information to separate the low from the high-risk population, but does not give better results than the D_{max} if taken alone, a combination of metrics was sought.

For reference, we started with the D_{max} alone as feature to predict the future risk, providing a mediocre yet above the average predictor. Clinical information did not perform well either but the missing clinical features for some patient may have a large impact on the predictor and results shall be taken cautiously. However, age, systolic and diastolic pressure and BMI are known factors associated with AAA risk. When the morphological and hemodynamic features are considered separately, the predictor performs well, even with the repetition of the 3-folds splits on a small cohort of patients. Once all features are

merged, the AUC reaches 0.95. However, despite high values of AUCs for flow and morphological features, Table 2.VIII shows that taking either flow metrics or all features leads to a significant difference with using the D_{max} alone. We believe that the very conservative results of the p-values (in Table 2.VIII) comes from the variability of the AUCs during the k-fold repetition (visible in Figure 2.8). A larger patient database with a prospective follow-up should confirm the clinical relevance of the AUC obtained here. However, morphological features can now be easily obtained by lumen and thrombus segmentation [KTD+11] for a significant increase in classification power. Even if the relation between flow alteration and AAA growth is still poorly understood, the combination of flow pattern with morphological analyses clearly improves patient risk stratification and should be integrated in future clinical algorithms.

2.4.3 Limitation

This study presents limitations discussed below:

- Simulation did not include wall deformation due to the pressure variation during the cardiac cycle. While FSI models for the aorta exist, the aortic wall was considered rigid, in accordance both with previous measurements [JSG+18] and literature [RKCdT+06]. Also, in the context of diseased aortas, the wall is highly heterogeneous and no non-invasive measurement can currently capture such heterogeneous mechanical properties.

- Boundary conditions are literature-based as this was a retrospective study. Thus, no patient-specific measurement was available, as often in such cases. However, flow patterns were favorably compared with PC-MRI data on a few patients with AAA [JSG+18].

- To characterize AAA growth, metrics were compared patch to patch which does not reflect the non-homogeneous and anisotropic growth of AAA. In the absence of

local wall displacement tracking method, this approach still gives insights on AAA growth.

- Considering the number of follow-up scans available, the learning approach did not considered AAAs as time-series. An approach similar to Lipton et al. [LKEW15] could eventually be implemented on a database with more follow-up scans per patient.

- The healthy population was 13 years younger than the AAA population on average (but with aortas already showing signs of aging, see Figure 2.3) and clinical data was not available for all patients, see Table 2.II.

- The database did not include ruptured aneurysms for the reasons described in the Methods section. When such data become available for AAA, the link between 'high risk' as defined here by clinicians and rupture prediction should be studied. A very recent study in cerebral aneurysms showed adverse morphology and hemodynamics to be related to aneurysm rupture [DCJ+19]. The corresponding statistical model of rupture probability was then successfully validated [DFJM+18]. These results combined with our findings give hope that such approach should be successful for AAAs as well.

- While flow in healthy aortas remain laminar, transition to turbulence may occur in AAAs due to the brutal enlargement[LSF+10] and could impact the studied wall fields.

2.4.4 Conclusion

We have presented a retrospective population study on the metrics quantifying the growth of AAA, and have built a model to anticipate their further evolution towards rupture. This longitudinal study included clinical and imaging data available at different time points for a total number of 138 scans from 42 patients. The analysis considered clini-

cal, morphological and simulation-based hemodynamic metrics, separately or combined to incorporate a diversity of potential growth markers. Different global and local metrics or their time evolution were found to separate the healthy, low-risk and high-risk groups. Local hemodynamics metrics presented in fact a large intra- and interpatient variability: even if for some patients a clear relationship could be established between hemodynamics variables and growth, their extrapolation to the whole population is yet to be found. Nevertheless, a risk predictor could be built with supervised learning from the clinical, morphological and simulation-based hemodynamic metrics. From a clinical point of view, we have shown that, compared to the current clinical criteria, morphological metrics describing the lumen and ILT shape could already greatly improve risk prediction, and thus potentially patient follow-up or treatment decision, at a moderate analysis cost. Blood flow simulations provide valuable additional information for the predictor, as well as for understanding the underlying relationship between flow alteration and AAA growth. Finally, risk prediction works best by combining all metrics. Although the results show the high predictive value of this approach, validation of the risk predictors on another set of data is needed before clinical translation.

2.5 Acknowledgments

The authors thank Daniel Stubbs and Compute Canada for the HPC support. The presented work relies on open-source projects and their community, especially *OpenFOAM* and ITKSnap (http://www.itksnap.org). This work has been supported by the Collaborative Research and Development Grants no. 460903-13 provided by the Natural Sciences and Engineering Research Council of Canada (NSERC) and the Industry-partnered Collaborative Research grant no. 124294 from the Canadian Institutes of Health Research (CIHR).

2.6 Electronic Supplementary Material

2.6.1 Boundary conditions

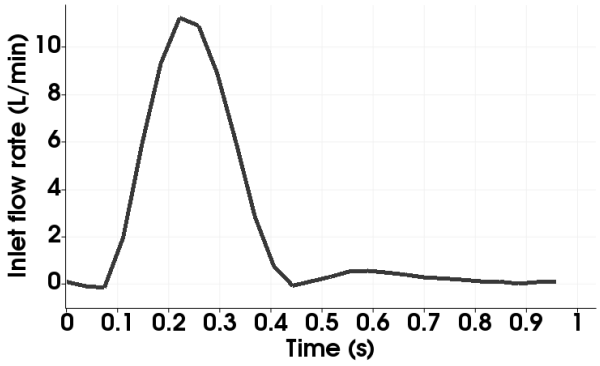

Figure I – Volumetric flow rate imposed at the inlet of the AAA.

2.6.2 Metrics description

2.6.3 Local distribution

Outlets	**Rp**	**C**	**Rd**
Mes. Sup.	$6.7 * 10^3$	$8.11 * 10^6$	$1.13 * 10^5$
Celiac	$6.7 * 10^3$	$8.11 * 10^6$	$1.13 * 10^5$
Renal	$1.2 * 10^4$	$1.8 * 10^{-5}$	$4.8 * 10^4$
Int. Iliac	$4.55 * 10^3$	$1.582 * 10^{-5}$	$7.7 * 10^4$
Ext. Iliac	$4.8 * 10^3$	$1.75 * 10^{-5}$	$8.2 * 10^4$

Table I – Proximal resistance, compliance and distale resistance for the 0D-RCR model, from Xiao et al. [XHF13] (in [CGS] units).

	Metric notation	Extraction	Remarks & litt.
Morphological parameters	D_{max}^{lumen}	maximal diameter of the lumen in a plane orthogonal to the luminal centerline	-
	D_{max}	maximal diameter of the AAA (inc. ILT) in a plane orthogonal to the luminal centerline	Current clinical criteria.
	H^{ILT}	thrombus thickness, computed as the Euclidean distance between the lumen and ILT	-
	Lumen centerline curvature	inverse of the radius of the local oscillating circle	Shum et al. [SMDM+11]
	Lumen centerline tortuosity	ratio between the centerline length and the endpoints distance.	Shum et al. [SMDM+11]
	Lumen NSI	$\frac{1}{2.199}\frac{\sqrt{Area}}{\sqrt[3]{Volume}}$	Raghavan et al. [RKCdT+06]
	Lumen (ILT) volume	volume of the lumen (ILT) between the renal and the iliac bifurcation.	-
	Lumen (ILT) surface area	surface of the lumen (ILT) between the renal and the iliac bifurcation.	-
	ILT coverage	percentage of the lumen covered with thrombus. The observed quantity is the ratio of lumen outer wall area exposed to ILT to the total area, not the aortic wall covered in ILT	-
hemodynamic param.	TAWSS	$\frac{1}{T}\int_0^T \lvert\tau_W\rvert \mathrm{dt}$	Bluestein et al. [BNSD96] and Arzani et al. [ASDS14a]
	OSI	$\frac{1}{2}\left(1-\frac{\lvert\int_0^T \tau_W \mathrm{dt}\rvert}{\int_0^T \lvert\tau_W\rvert \mathrm{dt}}\right)$	Arzani al. [ASDS14a]
	RRT	$\frac{1}{(1-2OSI)\,TAWSS}$	Himburg et al. [Him04]
	ECAP	$\frac{OSI}{TAWSS}$	Di Achille et al. [DATFH14]
	WSSG	$\lvert\nabla WSS\rvert$	Nagel et al. [NRDG99]

Table II – Description of the various metrics used in the article.

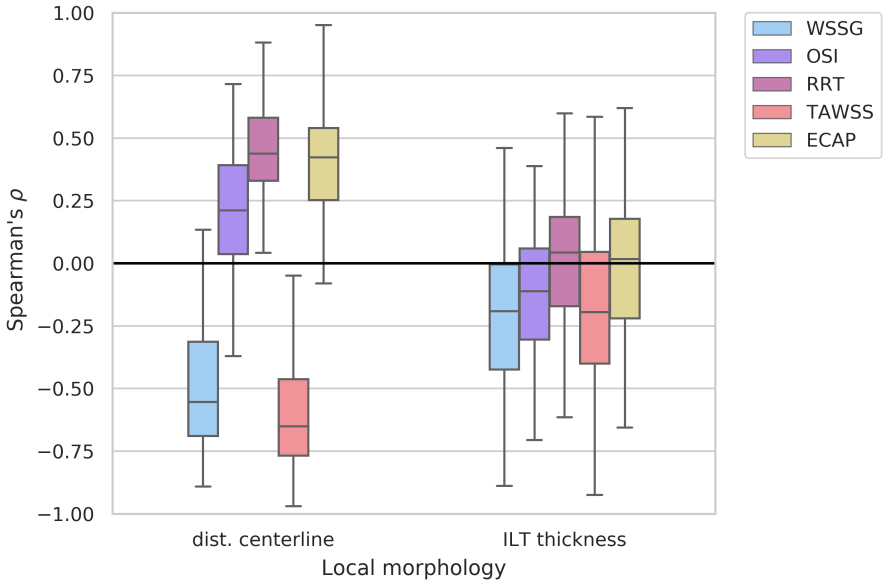

(a) All CTs evaluated independently.

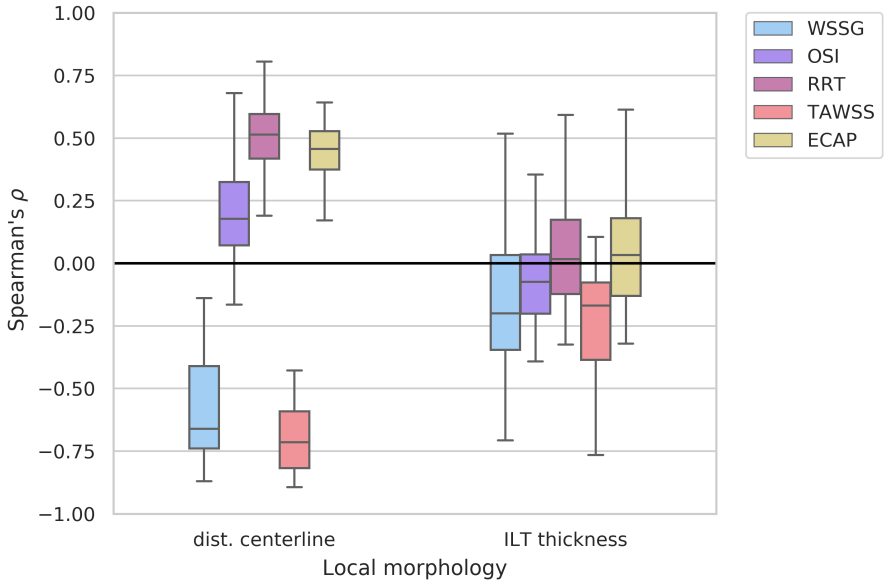

(b) Statistics performed on each patient, (one correlation for all scans of that patient).

Figure 2.7 – Boxplot of the distribution of Spearman's ρ between local flow and morphological evaluation metrics. On the left, all scans are evaluated separately and on the right statistics are patient-wise. The boxes represent the inter-quartile range (IQR) i.e. data between the 25 (Q1) and 75% (Q3) percentile. Bottom whisker is $Q1 - 1.5IQR$ and top whisker is $Q3 + 1.5IQR$. Outliers are not represented for readability. Correlations are computed on patch-wise data for each scan. The large dispersion of Spearman's ρ distribution is illustrated in Figure 2.6 for one metric.

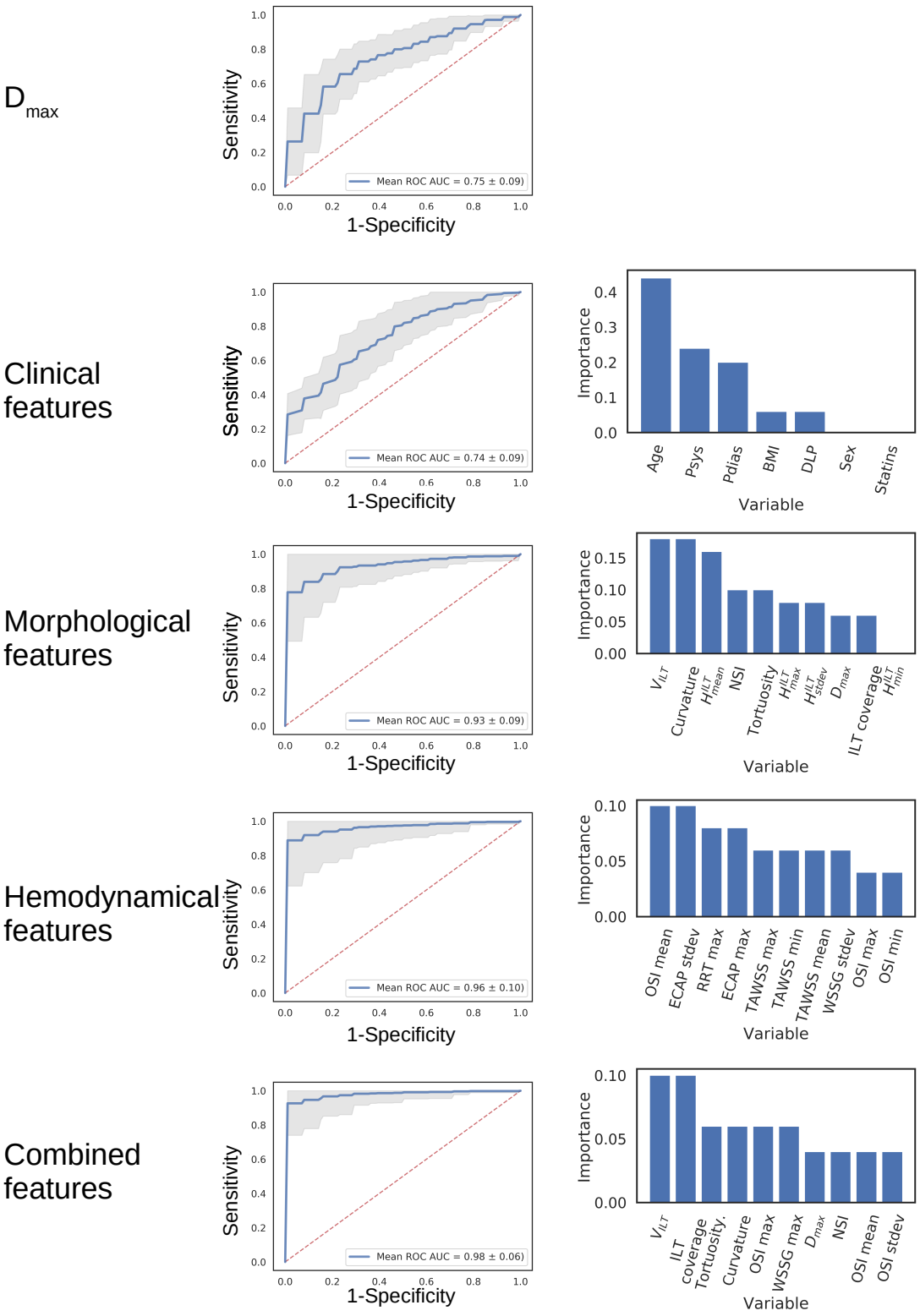

Figure 2.8 – Left: ROC curves for the classification of high risk (i.e. risk predictor). Right: Top 10 features ranked with respect to predictability of the target variable.

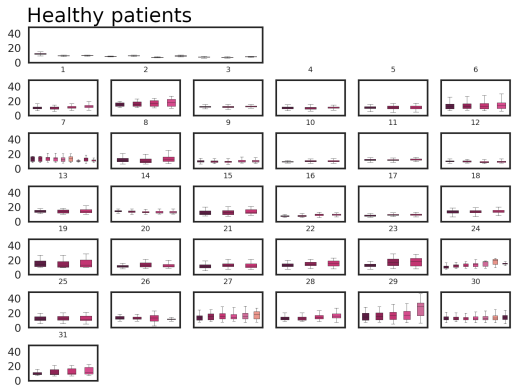

a) lumen - centerline distance

b) RRT

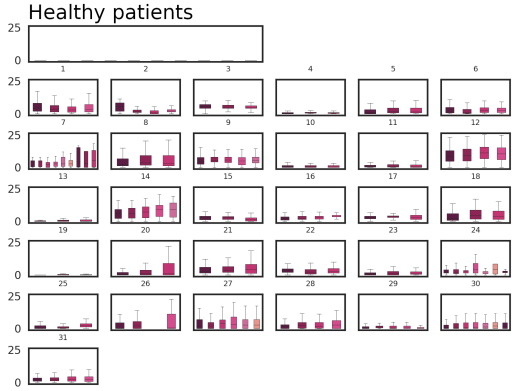

c) H_{max}^{ILT}

d) ECAP

e) WSSG

Figure II – Boxplot of local distribution of various metrics, for all patient, along their follow-up. Statistical distribution is built from data from all 600 patches.The box represents the inter-quartile range (IQR) or data between the 25 (Q1) and 75% (Q3) percentile. Bottom whisker is $Q1 - 1.5IQR$ and top whisker is $Q3 + 1.5IQR$. Outliers are not represented for the sake of readability.

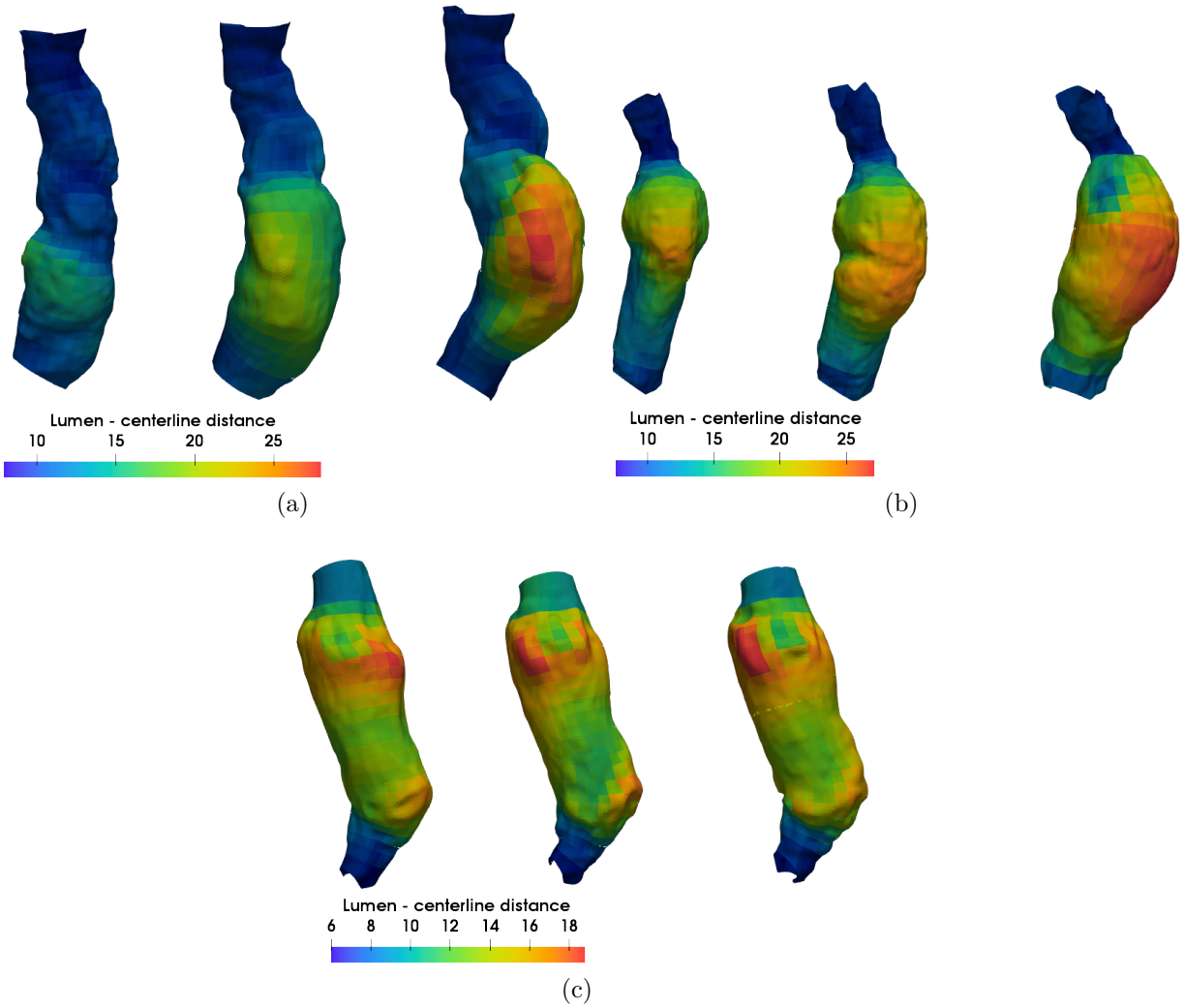

Figure III – View of local distance from the lumen to the centerline mapped on the lumen and averaged on patches for patient 6, 21 and 22. Patient 6 exhibits a strong and localized growth of the lumen. Patient 21's lumen is pretty tubular with a constant diameter while patient 22's diameter is healthy at the proximal neck and over 50 mm at the D_{max} location, hence the large dispersion of values seen on the boxplot.

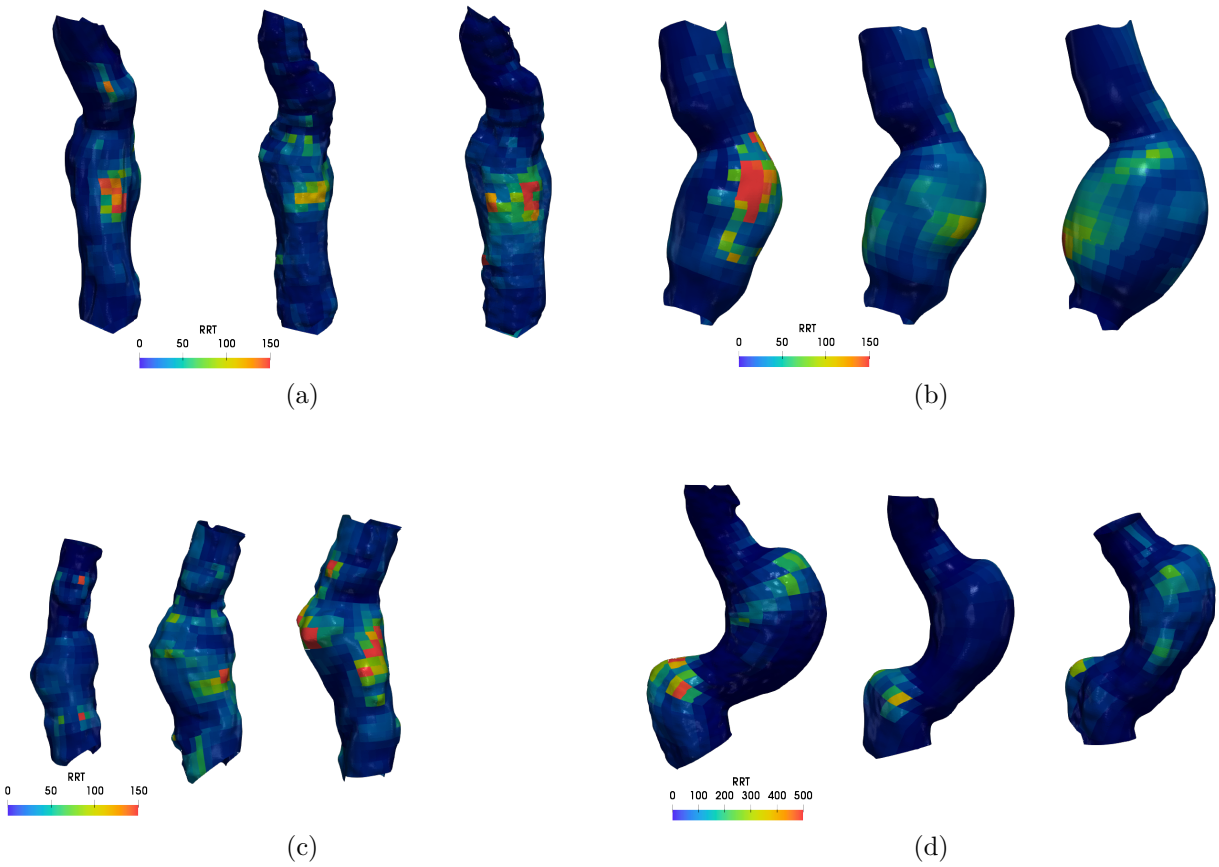

Figure VI – For 4 patients, RRT averaged on patches. Patient 10, left, exhibits a steady growth with time. Patient 2 (center top): RRT standard deviation is relatively small compared to patient 29 (center bottom). For patient 15, right, RRT decreases before increasing.

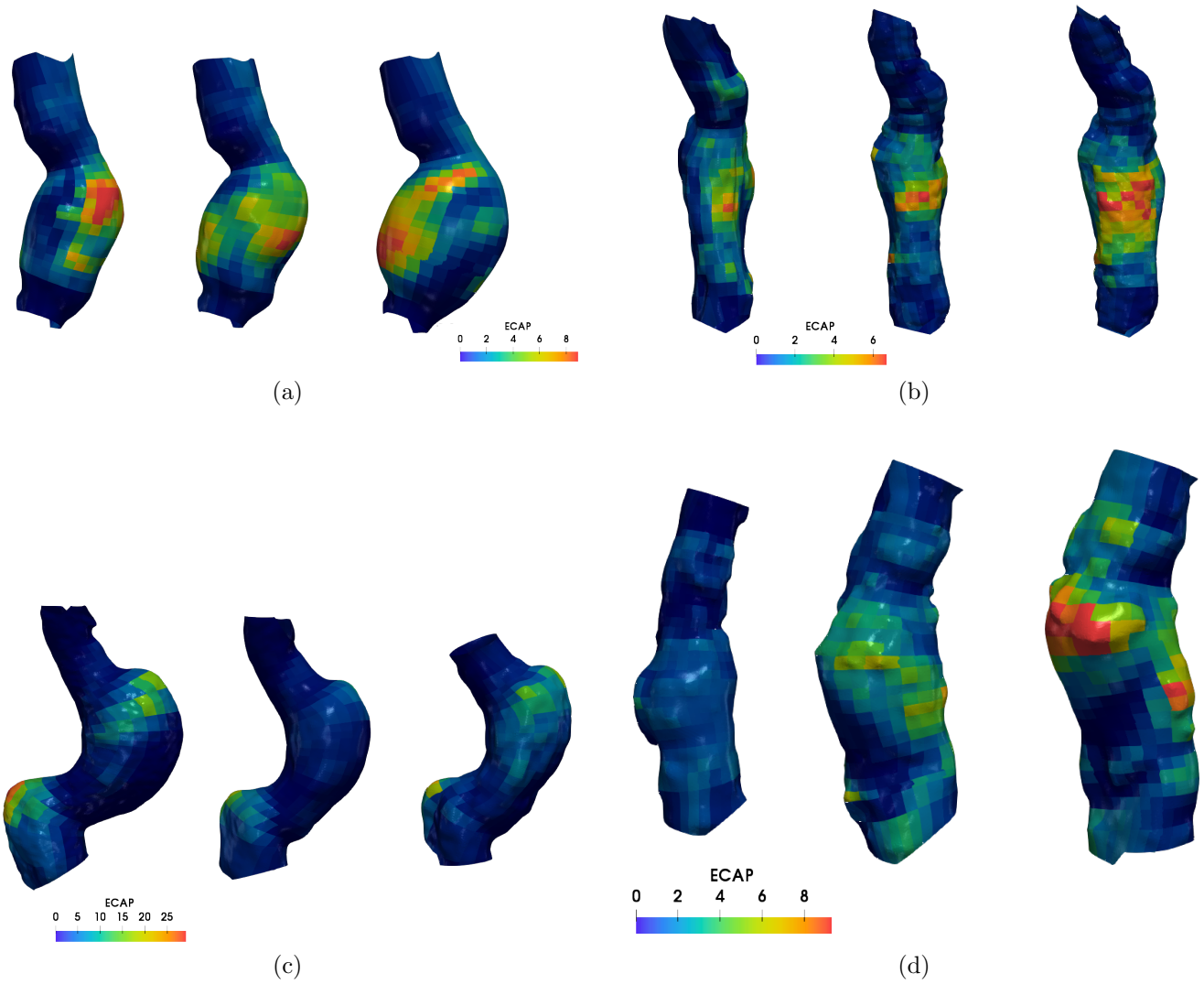

Figure V – ECAP averaged on patches, for 4 patients. ECAP, similarly to the RRT contains information from OSI and TAWSS. Left, patient 10, monotonic growth, center top patient 28 with a small standard deviation compared to patient 29, center bottom. Patient 15 ECAP average, right, decreases and then increases.

BIBLIOGRAPHY

AEIR03. Luca Antiga, Bogdan Ene-Iordache, and Andrea Remuzzi. Computational geometry for patient-specific reconstruction and meshing of blood vessels from MR and CT angiography. *Medical Imaging, IEEE Transactions on*, 22(5):674–684, 5 2003.

AS04. Luca Antiga and David A. Steinman. Robust and objective decomposition and mapping of bifurcating vessels. *IEEE Transactions on Medical Imaging*, 2004.

ASDS14a. A. Arzani, G.-Y. Suh, R. L. Dalman, and S. C. Shadden. A longitudinal comparison of hemodynamics and intraluminal thrombus deposition in abdominal aortic aneurysms. *AJP: Heart and Circulatory Physiology*, 307(12):H1786–H1795, 12 2014.

ASDS14b. Amirhossein Arzani, Ga-Young Suh, Ronald L. Dalman, and Shawn C. Shadden. A longitudinal comparison of hemodynamics and intraluminal thrombus deposition in abdominal aortic aneurysms. *American Journal of Physiology-Heart and Circulatory Physiology*, 307(12):H1786–H1795, 12 2014.

BAH18. D Bhagavan, P Di Achille, and J D Humphrey. Strongly Coupled Morphological Features of Aortic Aneurysms Drive Intraluminal Thrombus. *Scientific Reports*, (August):1–18, 2018.

BCB+18. Cristóbal Bertoglio, Alfonso Caiazzo, Yuri Bazilevs, Malte Braack, Mahdi Esmaily, Volker Gravemeier, Alison L. Marsden, Olivier Pironneau, Irene E. Vignon-Clementel, and Wolfgang A. Wall. Benchmark problems for numerical treatment of backflow at open boundaries. *International Journal for Numerical Methods in Biomedical Engineering*, 2018.

BCH+03. David C. Brewster, Jack L. Cronenwett, John W. Hallett, K. Wayne Johnston, William C. Krupski, and Jon S. Matsumura. Guidelines for the treatment of abdominal aortic aneurysms: Report of a subcommittee of the Joint Council of the American Association for Vascular Surgery and Society for Vascular Surgery. *Journal of Vascular Surgery*, 37(5):1106–1117, 2003.

BFKS+11. Róbert Busa-Fekete, Balázs Kégl, György Szarvas, Olivier Chapelle, Yi Chang, and Tie-Yan Liu. Ranking by calibrated AdaBoost. In *Learning to Rank Challenge*, 2011.

BKC00. J. R. Buchanan, C. Kleinstreuer, and J. K. Comer. Rheological effects on pulsatile hemodynamics in a stenosed tube. *Computers and Fluids*, 29(6):695–724, 2000.

BKHF11. C. Basciano, C. Kleinstreuer, S. Hyun, and E. A. Finol. A relation between near-wall particle-hemodynamics and onset of thrombus formation in abdominal aortic aneurysms. *Annals of Biomedical Engineering*, 39(7):2010–2026, 9 2011.

BKLK16. April J. Boyd, David C.S. Kuhn, Richard J. Lozowy, and Gordon P. Kulbisky. Low wall shear stress predominates at sites of abdominal aortic aneurysm rupture. *Journal of Vascular Surgery*, 63(6):1613–1619, 6 2016.

BKNS00. M.M.a Breuniq, H.-P.a Kriegel, R.T.b Ng, and J.a Sander. LOF: Identifying density-based local outliers. *SIGMOD Record (ACM Special Interest Group on Management of Data)*, 2000.

BNSD96. D. Bluestein, L. Niu, R. T. Schoephoerster, and M. K. Dewanjee. Steady Flow in an Aneurysm Model: Correlation Between Fluid Dynamics and Blood Platelet Deposition. *Journal of Biomechanical Engineering*, 118(3):280, 1996.

BSTM90. C. C. Boring, T. S. Squires, T Tong, and S Montgomery. Cancer statistics, 1994. *CA: a cancer journal for clinicians*, 44(1):7–26, 1 1990.

BTF+04. Anthony R. Brady, Simon G. Thompson, F. Gerald R. Fowkes, Roger M. Greenhalgh, and Janet T. Powell. Abdominal aortic aneurysm expansion: Risk factors and time intervals for surveillance. *Circulation*, 110(1):16–21, 2004.

CBD+09. Elliot L. Chaikof, David C. Brewster, Ronald L. Dalman, Michel S. Makaroun, Karl A. Illig, Gregorio A. Sicard, Carlos H. Timaran, Gilbert R. Upchurch, and Frank J. Veith. The care of patients with an abdominal aortic aneurysm: The Society for Vascular Surgery practice guidelines. *Journal of Vascular Surgery*, 50(4):S2–S49, 2009.

CBH+02. Elliot L. Chaikof, Jan D. Blankensteijn, Peter L. Harris, Geoffrey H. White, Christopher K. Zarins, Victor M. Bernhard, Jon S. Matsumura, James May, Frank J. Veith, Mark F. Fillinger, Robert B. Rutherford, and K.Craig Kent. Reporting standards for endovascular aortic aneurysm repair. *Journal of Vascular Surgery*, 35(5):1048–1060, 2002.

CDE+18. Elliot L. Chaikof, Ronald L. Dalman, Mark K. Eskandari, Benjamin M. Jackson, W. Anthony Lee, M. Ashraf Mansour, Tara M. Mastracci, Matthew Mell, M. Hassan Murad, Louis L. Nguyen, Gustavo S. Oderich, Madhukar S. Patel, Marc L. Schermerhorn, and Benjamin W. Starnes. The Society for Vascular Surgery practice guidelines on the care of patients with an abdominal aortic aneurysm. *Journal of Vascular Surgery*, 67(1):2–77, 2018.

DATFH14. P. Di Achille, G. Tellides, C. A. Figueroa, and J. D. Humphrey. A haemodynamic predictor of intraluminal thrombus formation in abdominal aortic aneurysms. *Proceedings of the Royal Society A: Mathematical, Physical and Engineering Sciences*, 470(2172):20140163–20140163, 2014.

DCJ+19. Felicitas J. Detmer, Bong Jae Chung, Carlos Jimenez, Farid Hamzei-Sichani, David Kallmes, Christopher Putman, and Juan R. Cebral. Associations of hemodynamics, morphology, and patient characteristics with aneurysm rupture stratified by aneurysm location. *Neuroradiology*, 2019.

DDCP88. E R DeLong, D M DeLong, and D L Clarke-Pearson. Comparing the areas under two or more correlated receiver operating characteristic curves: a nonparametric approach. *Biometrics*, 44(3):837–45, 1988.

DFJM+18. Felicitas J Detmer, Daniel Fajardo-Jiménez, Fernando Mut, Norman Juchler, Sven Hirsch, Vitor Mendes Pereira, Philippe Bijlenga, and Juan R Cebral. External validation of cerebral aneurysm rupture probability model with data from two patient cohorts. *Acta neurochirurgica*, 2018.

DMBO77. R C Darling, C R Messina, D C Brewster, and L W Ottinger. Autopsy study of unoperated abdominal aortic aneurysms. The case for early resection. *Circulation*, 56(3 Suppl):161–4, 9 1977.

DWMY14. Tyler Duellman, Christopher L. Warren, Jon Matsumura, and Jay Yang. Analysis of multiple genetic polymorphisms in aggressive-growing and slow-growing abdominal aortic aneurysms. *Journal of Vascular Surgery*, 60(3):613–621, 9 2014.

EMBH+11. Mahdi Esmaily Moghadam, Yuri Bazilevs, Tain Yen Hsia, Irene E. Vignon-Clementel, and Alison L. Marsden. A comparison of outlet boundary treatments for prevention of backflow divergence with relevance to blood flow simulations. *Computational Mechanics*, 48(3):277–291, 2011.

ET07. B. Efron and R. Tibshirani. [Bootstrap Methods for Standard Errors, Confidence Intervals, and Other Measures of Statistical Accuracy]: Rejoinder. *Statistical Science*, 1(1):77–77, 2007.

FA01. Ender A. Finol and Cristina H. Amon. Blood flow in abdominal aortic aneurysms: pulsatile flow hemodynamics. *Journal of biomechanical engineering*, 123(5):474–484, 10 2001.

GWH15. Andrii Grytsan, Paul N. Watton, and Gerhard A. Holzapfel. A Thick-Walled Fluid–Solid-Growth Model of Abdominal Aortic Aneurysm Evolution: Application to a Patient-Specific Geometry. *Journal of Biomechanical Engineering*, 137(3):031008, 2015.

HCC+18. Stephen J. Haller, Jeffrey D. Crawford, Katherine M. Courchaine, Colin J. Bohannan, Gregory J. Landry, Gregory L. Moneta, Amir F. Azarbal, and Sandra Rugonyi. Intraluminal thrombus is associated with early rupture of abdominal aortic aneurysm. *Journal of Vascular Surgery*, 67(4):1051–1058, 4 2018.

Him04. H. A. Himburg. Spatial comparison between wall shear stress measures and porcine arterial endothelial permeability. *AJP: Heart and Circulatory Physiology*, 286(5):H1916–H1922, 2004.

Jas96. Hrvoje Jasak. *Error Analysis and Estimation for the Finite Volume Method with Applications to Fluid Flows*. PhD thesis, Imperial College, University of London, 1996.

JSG+18. Florian Joly, Gilles Soulez, Damien Garcia, Simon Lessard, and Claude Kauffmann. Flow stagnation volume and abdominal aortic aneurysm growth: Insights from patient-specific computational flow dynamics of Lagrangian-coherent structures. *Computers in Biology and Medicine*, 92:98–109, 1 2018.

JW00. H. Jasak and H. G. Weller. Application of the finite volume method and unstructured meshes to linear elasticity. *International Journal for Numerical Methods in Engineering*, 48(2):267–287, 2000.

KTD+11. Claude Kauffmann, An Tang, Alexandre Dugas, Éric Therasse, Vincent Oliva, and Gilles Soulez. Clinical validation of a software for quantitative follow-up of abdominal aortic aneurysm maximal diameter and growth by CT angiography. *European Journal of Radiology*, 77(3):502–508, 2011.

LKEW15. Zachary C. Lipton, David C. Kale, Charles Elkan, and Randall Wetzel. Learning to Diagnose with LSTM Recurrent Neural Networks. 11 2015.

LSF+10. Andrea S. Les, Shawn C. Shadden, C. Alberto Figueroa, Jinha M. Park, Maureen M. Tedesco, Robert J. Herfkens, Ronald L. Dalman, and Charles A. Taylor. Quantification of hemodynamics in abdominal aortic aneurysms during rest and exercise using magnetic resonance imaging and computational fluid dynamics. *Annals of Biomedical Engineering*, 38(4):1288–1313, 2010.

MGG+70. C. J. Mills, I. T. Gabe, J. H. Gault, D. T. Mason, J. Ross, E. Braunwald, and J. P. Shillingford. Pressure-flow relationships and vascular impedance in man. *Cardiovascular Research*, 4(4):405–417, 1970.

MGGE+07. Anna Marcinkowska-Gapińska, Jacek Gapinski, Waldemar Elikowski, Feliks Jaroszyk, and Leszek Kubisz. Comparison of three rheological models of shear flow behavior studied on blood samples from post-infarction patients. *Medical and Biological Engineering and Computing*, 45(9):837–844, 2007.

MK96. E W Merrill and M. Kaibara. Rheology of blood. *Biorheology*, 33(2):101–117, 1996.

MLLS+16. Giampaolo Martufi, Moritz Lindquist Liljeqvist, Natzi Sakalihasan, Giuseppe Panuccio, Rebecka Hultgren, Joy Roy, and T. Christian Gasser. Local Diameter, Wall Stress, and Thrombus Thickness Influence the Local Growth of Abdominal Aortic Aneurysms. *Journal of Endovascular Therapy*, 23(6):957–966, 2016.

MMKB94. J.E. E. Moore, S.E. E. Maier, D.N. N. Ku, and P. Boesiger. Hemodynamics in the abdominal aorta: A comparison of in vitro and in vivo measurements. *J Appl Physiol*, 76(4):1520–1527, 4 1994.

NRDG99. Tobi Nagel, Nitzan Resnick, C. Forbes Dewey, and Michael A. Gimbrone. Vascular endothelial cells respond to spatial gradients in fluid shear stress by enhanced activation of transcription factors. *Arteriosclerosis, Thrombosis, and Vascular Biology*, 19(8):1825–1834, 1999.

OGD+92. Kenneth Ouriel, Richard M. Green, Carlos Donayre, Cynthia K. Shortell, Janice Elliott, and James A. DeWeese. An evaluation of new methods of expressing aortic aneurysm size: Relationship to rupture. *Journal of vascular surgery*, 15(1):12–20, 1 1992.

PFL+15. Fran Parkinson, Stuart Ferguson, Peter Lewis, Ian M. Williams, Christopher P. Twine, and South East Wales Vascular Network. Rupture rates of untreated large abdominal aortic aneurysms in patients unfit for elective repair. *Journal of Vascular Surgery*, 61(6):1606–1612, 6 2015.

RKCdT+06. Madhavan L. Raghavan, Jarin Kratzberg, E. M. Castro de Tolosa, Mauro M. Hanaoka, Patricia Walker, Erasmo Simão da Silva, Erasmo Magalhães Castro de Tolosa, Mauro M. Hanaoka, Patricia Walker, and Erasmo Simão da Silva. Regional distribution of wall thickness and failure properties of human abdominal aortic aneurysm. *J Biomech*, 39(16):3010–3016, 2006.

RMP+13. C. Reeps, A. Maier, J. Pelisek, F. Härtl, V. Grabher-Meier, W. A. Wall, M. Essler, H. H. Eckstein, and M. W. Gee. Measuring and modeling patient-specific distributions of material properties in abdominal aortic aneurysm wall. *Biomechanics and Modeling in Mechanobiology*, 12(4):717–733, 2013.

RMYC+15. Ethan M. Rowland, Yumnah Mohamied, K. Yean Chooi, Emma L. Bailey,

Peter D. Weinberg, K Yean Chooi, Emma L. Bailey, and Peter D. Weinberg. Comparison of Statistical Methods for Assessing Spatial Correlations Between Maps of Different Arterial Properties. *Journal of Biomechanical Engineering*, 137(10100):3, 8 2015.

Roa94. P. J. Roache. Perspective: A Method for Uniform Reporting of Grid Refinement Studies, 1994.

SDVM+17. Florian Strub, Harm De Vries, Jeremie Mary, Bilal Piot, Aaron Courvile, and Olivier Pietquin. End-to-end optimization of goal-driven and visually grounded dialogue systems. In *IJCAI International Joint Conference on Artificial Intelligence*, 2017.

SGB+17. Raoul R.F. Stevens, Andrii Grytsan, Jacopo Biasetti, Joy Roy, Moritz Lindquist Liljeqvist, and T. Christian Gasser. Biomechanical changes during abdominal aortic aneurysm growth. *PLoS ONE*, 12(11):e0187421, 11 2017.

SH13. Shawn C. Shadden and Sahar Hendabadi. Potential fluid mechanic pathways of platelet activation. *Biomechanics and Modeling in Mechanobiology*, 12(3):467–474, 2013.

SKS00. J. Stenbaek, B. Kalin, and J. Swedenborg. Growth of thrombus may be a better predictor of rupture than diameter in patients with abdominal aortic aneurysms. *European Journal of Vascular and Endovascular Surgery*, 20(5):466–469, 2000.

SMDM+11. Judy Shum, Giampaolo Martufi, Elena Di Martino, Christopher B. Washington, Joseph Grisafi, Satish C. Muluk, Ender A. Finol, Elena Di Martino, Christopher B. Washington, Joseph Grisafi, Satish C. Muluk, and Ender A.

Finol. Quantitative assessment of abdominal aortic aneurysm geometry. *Annals of Biomedical Engineering*, 39(1):277–286, 1 2011.

SSWJ. S Solberg, K Singh, T Wilsgaard, and B K Jacobsen. {Increased growth rate of abdominal aortic aneurysms in women}, volume = {29}, unidentified = {EEuropean journal of vascular and endovascular surgery,)„2005},. *The Tromsøstudy*, (2):145–149.

SXCF11. Judy Shum, Amber Xu, Itthi Chatnuntawech, and Ender A. Finol. A framework for the automatic generation of surface topologies for abdominal aortic aneurysm models. *Annals of Biomedical Engineering*, 39(1):249–259, 2011.

TARA$^+$16. The Theano Development Team, R Al-Rfou, G Alain, A Almahairi, C Angermueller, D Bahdanau, N Ballas, F Bastien, J Bayer, A Belikov, A Belopolsky, Y Bengio, A Bergeron, J Bergstra, V Bisson, J B Snyder, N Bouchard, N Boulanger-Lewandowski, X Bouthillier, A de Brébisson, O Breuleux, P.-L. Carrier, K Cho, J Chorowski, P Christiano, T Cooijmans, M.-A. Côté, M Côté, A Courville, Y N Dauphin, O Delalleau, J Demouth, G Desjardins, S Dieleman, L Dinh, M Ducoffe, V Dumoulin, S E Kahou, D Erhan, Z Fan, O Firat, M Germain, X Glorot, I Goodfellow, M Graham, C Gulcehre, P Hamel, I Harlouchet, J.-P. Heng, B Hidasi, S Honari, A Jain, S Jean, K Jia, M Korobov, V Kulkarni, A Lamb, P Lamblin, E Larsen, C Laurent, S Lee, S Lefrancois, S Lemieux, N Léonard, Z Lin, J A Livezey, C Lorenz, J Lowin, Q Ma, P.-A. Manzagol, O Mastropietro, R T McGibbon, R Memisevic, B van Merriënboer, V Michalski, M Mirza, A Orlandi, C Pal, R Pascanu, M Pezeshki, C Raffel, D Renshaw, M Rocklin, A Romero, M Roth, P Sadowski, J Salvatier, F Savard, J Schlüter, J Schulman, G Schwartz, I V Serban, D Serdyuk, S Shabanian, C Simon, S Spieckermann, S R Subramanyam, J Sygnowski, and J Tanguay. J. *Turian, S. Urban, P. Vincent, F.*

Visin, H. de Vries, D. Warde-Farley, D. J. Webb, M. Willson, K. Xu, L. Xue, L. Yao, S. Zhang, and Y. Zhang. {*Theano: A Python framework for fast computation of mathematical expressions*}. *arXiv e-prints*, 19, 2016.

TGP+15. F. Tanios, M. W. Gee, J. Pelisek, S. Kehl, J. Biehler, V. Grabher-Meier, W. A. Wall, H. H. Eckstein, and C. Reeps. Interaction of Biomechanics with Extracellular Matrix Components in Abdominal Aortic Aneurysm Wall. *European Journal of Vascular and Endovascular Surgery*, 50(2):167–174, 2015.

TKM+17. Konstantinos Tzirakis, Yiannis Kamarianakis, Eleni Metaxa, Nikolaos Kontopodis, Christos V. Ioannou, and Yannis Papaharilaou. A robust approach for exploring hemodynamics and thrombus growth associations in abdominal aortic aneurysms. *Medical and Biological Engineering and Computing*, 55(8):1493–1506, 2017.

Wom55. J. R. Womersley. Method for the calculation of velocity, rate of flow and viscous drag in arteries when the pressure gradient is known. *J Physiol*, 127(3):553–563, 3 1955.

WS15. Jiacheng Wu and Shawn C. Shadden. Coupled Simulation of Hemodynamics and Vascular Growth and Remodeling in a Subject-Specific Geometry. *Annals of biomedical engineering*, 43(7):1543–1554, 3 2015.

XHF13. Nan Xiao, Jay D. Humphrey, and C. Alberto Figueroa. Multi-scale computational model of three-dimensional hemodynamics within a deformable full-body arterial network. *Journal of Computational Physics*, 244:22–40, 2013.

XWR+17. Xianglai Xu, Brian Wang, Changhong Ren, Jiangnan Hu, David A Greenberg, Tianxiang Chen, Liping Xie, and Kunlin Jin. Age-related Impairment

of Vascular Structure and Functions. *Aging and disease*, 8(5):590–610, 10 2017.

YPH+06. Paul A. Yushkevich, Joseph Piven, Heather Cody Hazlett, Rachel Gimpel Smith, Sean Ho, James C. Gee, and Guido Gerig. User-guided 3D active contour segmentation of anatomical structures: Significantly improved efficiency and reliability. *NeuroImage*, 31(3):1116–1128, 2006.

ZGL+16. Byron A. Zambrano, Hamidreza Gharahi, ChaeYoung Young Lim, Farhad A. Jaberi, Jongeun Choi, Whal Lee, and Seungik Baek. Association of Intraluminal Thrombus, Hemodynamic Forces, and Abdominal Aortic Aneurysm Expansion Using Longitudinal CT Images. *Annals of Biomedical Engineering*, 44(5):1502–1514, 5 2016.

CHAPTER 3

Flow stagnation volume and abdominal aortic aneurysm growth: insights from patient-specific computational flow dynamics of Lagrangian-coherent structures

Abstract

ABDOMINAL aortic aneurysms (AAA) are localized, commonly-occurring dilations of the aorta. When equilibrium between blood pressure (loading) and wall mechanical resistance is lost, rupture ensues, and patient death follows, if not treated immediately. Experimental and numerical analyses of flow patterns in arteries show direct correlations between wall shear stress and wall mechano-adaptation with the development of zones prone to thrombus formation. For further insights into AAA flow topology/growth interaction, a workout of patient-specific computational flow dynamics (CFD) is proposed to compute finite-time Lyapunov exponents and extract Lagrangian-coherent structures (LCS). This computational model was first compared with 4-D phase-contrast magnetic resonance imaging (MRI) in 5 patients.

To better understand the impact of flow topology and transport on AAA growth, hyperbolic, repelling LCS were computed in 1 patient during the 8-year follow-up, including 9 volumetric morphologic AAA measures by computed tomography-angiography (CTA). LCS defined barriers to Lagrangian jet cores entering AAA. Domains enclosed between LCS and the aortic wall were considered to be stagnation zones. Their evolution was studied during AAA growth.

Good correlation – 2D cross-correlation coefficients of 0.65, 0.86 and 0.082 (min, max, SD) – was obtained between numerical simulations and 4-D MRI acquisitions in 6 specific cross-sections from 4 patients. In follow-up study, LCS divided AAA lumens into 3 dynamically-isolated zones: 2 stagnation volumes lying in dilated portions of the AAA, and circulating volume connecting the inlet to the outlet. The volume of each zone was tracked over time. Although circulating volume remained unchanged during 8-year follow-up, the AAA lumen and main stagnation zones grew significantly ($8\text{cm}^3\,\text{yr}^{-1}$ and $6\text{cm}^3\,\text{yr}^{-1}$, respectively).

This study reveals that transient transport topology can be quantified in patient-specific AAA during disease progression by CTA, in parallel with lumen morphology. It is anticipated that analysis of the main AAA stagnation zones by patient-specific CFD on a yearly basis could help predict AAA growth and rupture.

Keywords: aortic aneurysms; hemodynamics; transport topology; CFD; AAA growth; interventional radiology; intraluminal thrombus; FTLE

3.1 Introduction

Abdominal aortic aneurysms (AAA) are localized dilations of the abdominal aorta which can rupture if equilibrium between artery resistance and blood pressure is lost. AAA prevalence reaches 8.9 % among men and 2.2% among women: it is the 14^{th} leading cause of death in the USA [McG11]. AAA risk factors are typically the same as for atherosclerosis, i.e., gender (male), smoking, age, hypertension and hyperlipidemia [McG11] or [Ger13], but

genetic factors are also believed to contribute to AAA development, growth and rupture.

AAA are usually asymptomatic and are therefore often detected through unrelated examinations or dedicated screenings, such as echography or X-ray computed tomography (CT-scan). Once detected, AAA risk assessment is generally based on maximal diameter [OGD+92] (D_{max} criterion). Patients will undergo elective surgery if D_{max} is over a statistically-based threshold: 55 mm for men and less for women [OGD+92, HGT+15, HFC+08]. If D_{max} is below these values, AAA are examined yearly by ultrasound or CT-scan, until the surgical threshold is reached or if AAA D_{max} increases more than 1 cm per year [CBD+09]. Because of poor diagnostic performance of D_{max} [WBME00], new metrics have been introduced for better AAA-rupture risk assessment [BCH+03]. Efforts were first made to provide a better standard for maximum diameter [OGD+92]. The increasing availability of patient-specific 3D AAA models from computed tomography angiography (CTA) now makes individualized hemodynamic analyses possible, with blood flow simulation, fluid-solid interaction and multiphysics modeling. The latter couples mechanics with biology, enabling, for example, simplified simulations of AAA growth [GWH15, TOK+09, WS15] by replicating the evolution of wall composition and rheology.

The key factors that differentiate one AAA from another are geometric shape, mechanical tissue properties and flow topology [TKTP+14]. Some morphological features with known linkage to AAA rupture risk are, indeed, volume, surface, bulge height, tortuosity and local surface curvature [SMDM+11, TKTP+14]. Besides the above geometric attributes, mechanical wall stresses in AAAs depend upon tissue properties, which are essentially heterogeneous and nonlinear [RKCdT+06] and patient specific [RMP+13]. As it is impossible to fully characterize such properties as well as complex micro- to macro-scale interconnections, handling generalized numerical models for rupture risk prediction becomes difficult. Blood flow and its altered topology are known to play a key role in both wall-fluid shearing action and transport perturbations in AAA evolution [BKHF11, SH13]. Several metrics can efficiently account for the wall-shearing action [LAS09, PSW13b, PSW13a], but evaluation of transport changes in complex AAA flow remains challenging.

The presence of thrombus deposits over the AAA wall modifies its composition and mechanical behavior [WVDA+13]. Thrombus formation [BHCG11] has been linked to flow separation in the dilated portion of the aorta. The present study was motivated by the need for new tools to understand the contribution of fluid transport changes to AAA and thrombus growth.

The concept of Lagrangian-coherent structures (LCS) is an efficient way of characterizing transport in complex fluid flow. To cite [PH13], the LCS approach is a means of identifying key material lines that organize fluid-flow transport. LCS form separatrice surfaces, which divide the domain into dynamically-isolated regions and reveal the hidden flow skeleton. LCS defining Lagrangian jet cores [Hal11] can be extracted from maxima ridges in the so-called finite-time Lyapunov exponent (FTLE) scalar field. FTLE quantifies the rate of stretching between flow trajectories integrated over time. Previous studies [AS12, ADES12, ST08] have shown that extraction of LCS from the FTLE field allows the observation of blood flow transport over a complete cardiac cycle from an Eulerian point of view.

The purpose of this article is to provide an efficient numerical workflow to compute dynamically isolated zones from LCS inside the AAA lumen geometry extracted from patient-specific CTA. We hypothesize the identification of these stagnation zones could be useful to predict thrombus formation and its impact on AAA growth and vulnerability. The following section presents a numerical simulation model of 3D blood flow, with special emphasis on boundary conditions. Numerical flow was validated in 4 patients undergoing 4-D phase contrast MRI. The model then computed flow transport and stagnation zones in 9 CTA-based AAA geometries acquired over 8 years in specific patient follow-up. The chronologic evolution of altered flow topology in the lumen was computed and compared to morphological changes of AAA.

3.2 Materials and methods

This section describes the 3D computational flow dynamics (CFD) model and, more specifically, defines the parameters involved in boundary conditions. Patient-specific conditions were unavailable in the context of a retrospective study. Simulated velocity magnitudes were compared with those obtained by 4-D MRI velocimetry in 4 patients.

3.2.1 Blood flow simulation

Domain acquisition

Four patients with diagnosed AAA were enrolled: they were regularly followed by CT-scan to assess AAA growth and eligibility criteria for open or endovascular repair. The study was approved by the local Institutional review board, and all patients gave signed informed consent form. First, blood flow was computed in the last follow-up CTA in 4 patients with AAA (aged 70 $\pm$ 11.2 years) and compared to MRI velocimetry for validation. Then, blood stagnation zones on 9 follow-up CTAs acquired between 2006 and 2013 (Δ t_{avg} = 1 year, 14 days) were studied in another patient (age 79 years).

CTA voxel size ranged from (0.75×0.75×0.75) mm^3 to (0.85×0.85×1) mm^3 in the 3 orthogonal axes: anterior-posterior, right-left and craniocaudal, respectively. The lumen was segmented using the region growing tool of *MITK* [NZS+13] according to the following procedure: 1) placing the seed point in the lumen 2) Setting the upper and lower threshold values, varying on each scan. Particular attention was paid to the upper limit to avoid the segmentation of the bones. 3) Evolution of the contour until the whole domain is segmented. After segmentation, segmented lumen were smoothed using a Taubin [Tau95] filter, avoiding the shrinkage of the geometry. Outlets were extruded (1 diameter length) to provide circular boundary. Final surfaces were overlaid on the CTA and validated by a radiologist.

Boundary conditions

Inlet

A time-varying flow rate was imposed at the inlet [MGG+70], located approximately 5 cm upstream of the upper renal artery (Figure 3.1 1). Though actual inlet flow patterns

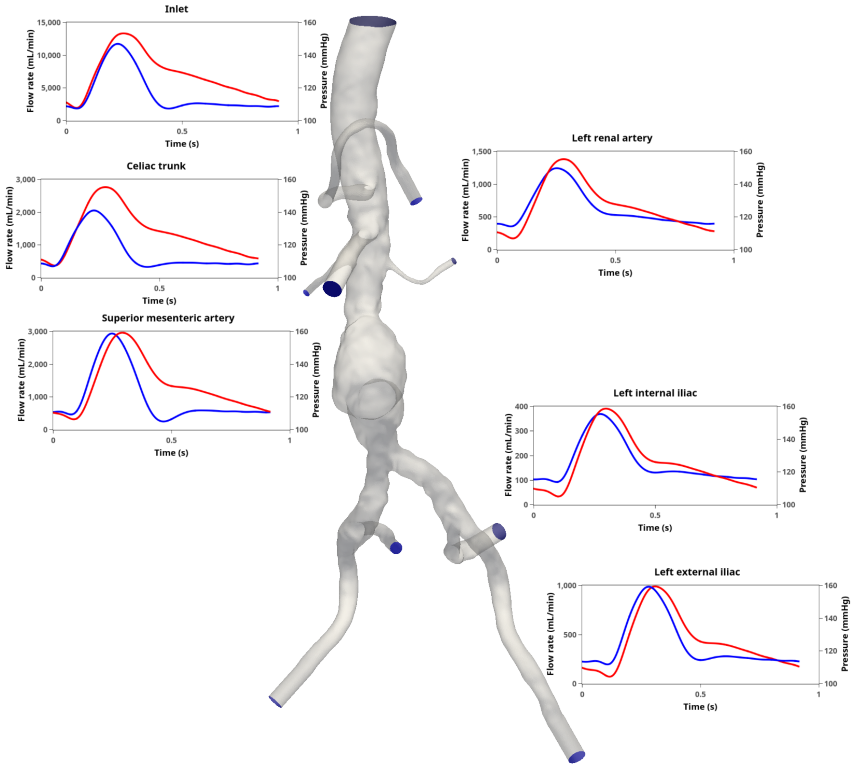

Figure 3.1 – Localization of the inlet and outlets boundary conditions. The pressure profiles are averaged on the surface of the boundary. At the inlet, a time varying flow rate is applied while at the outlets pressure is enforced using a 0D RCR model. For renal, internal and external iliac arteries, identical conditions were applied on both right and left side.

may present either single or double swirl structures [MPR+11], no generic spatial velocity profile can currently describe flow entering AAA. Considering the lack of available information, a time-dependent flow rate from [MGG+70] was mapped on a Womersley profile.

Wall

In AAA, wall geometry is characterized by the aorta and thrombus deposits. Aortic wall mechanical properties vary with vessel size and location as well as patient age. Wall rheology becomes highly patient-specific and heterogeneous with the progression of atherosclerotic disease [RKCdT+06]. The thrombus is also a complex, layer-structured and heterogeneous material [WVDA+13]. In practice, it is difficult, if not impossible, to characterize 3D wall rheology by non-invasive techniques for fluid-structure simulations. Wall stiffness increases with disease progression and patient age [TCRH11]. In addition, thrombus alters wall stress distribution and augments apparent stiffness [WMWV02]. The present study considered the wall and thrombus as rigid materials, and applied no-slip conditions. This simplification turned out to be acceptable according to the velocity measurements performed by MRI (see following text and Figure 3.3). Also, the potential impact on FTLE computation proved to be negligeable [DMS13].

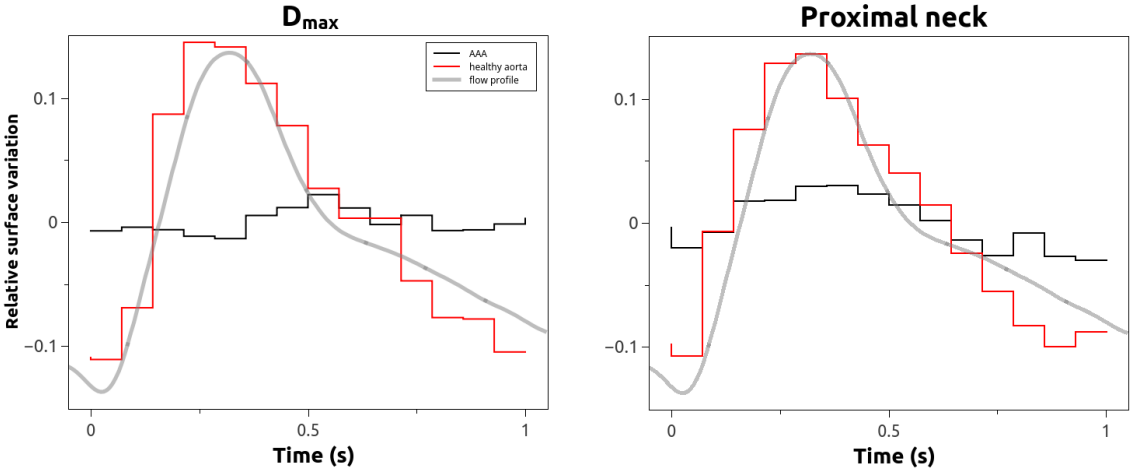

Figure 3.2 – Relative surface variation of the lumen. Data is average on 5 AAA (black) and 2 healthy aortas (red). On the left, the section was taken at the D max location along the axial axis and on the right at the proximal neck location. For healthy subjects, sections were done respectively mid distance between the lowest renal artery and the iliac bifurcation and approximately 2 cm under the lowest renal artery.

Outlets

Blood flow can present complex recirculation patterns in diseased aorta that can stretch

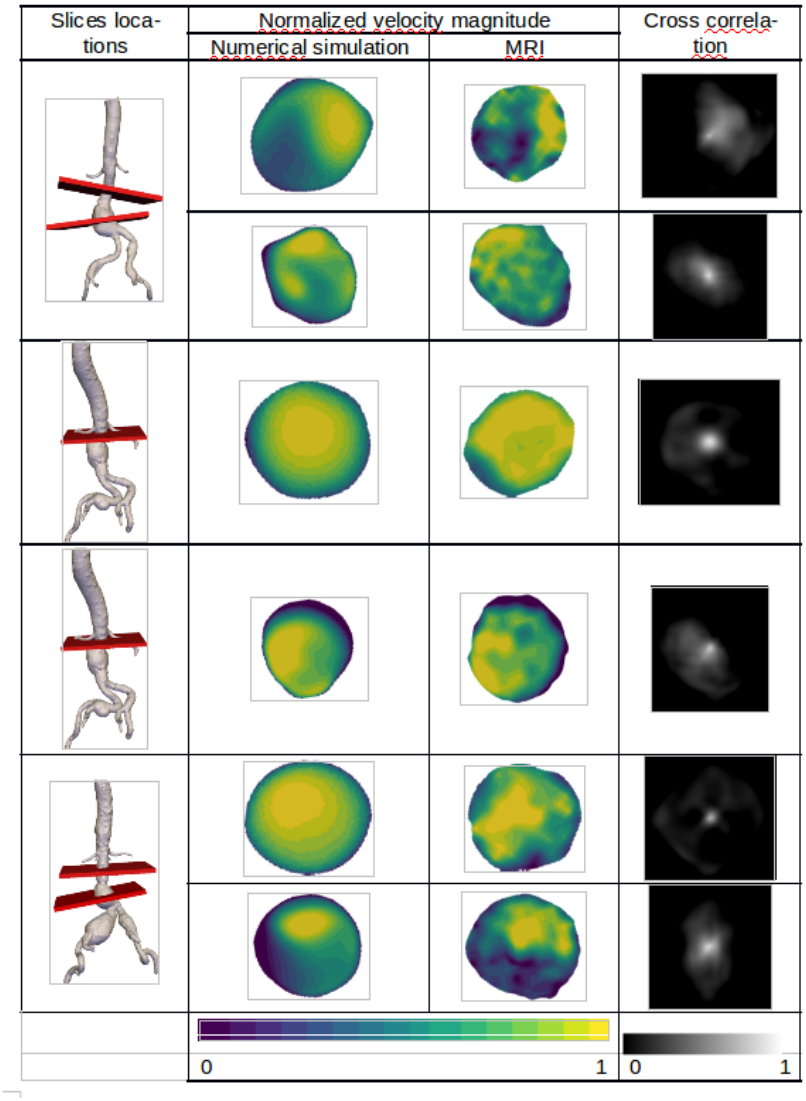

Figure 3.3 – Comparison between the simulated blood flow and the MRI measurements performed on 4 patients. Comparisons are done at the systolic peak and numerical values of the maximum cross-correlation are given.

down to outlet planes. Reverse flow is also a natural phenomenon occurring in large arteries during diastole [EMBH+11, KYM+93]. Artificial extension of outlets, leading to unrealistic geometries and increased number of mesh elements, is common practice in arterial flow simulations addressing these issues. Neumann boundary conditions on velocities were rather adopted with gradient to control blood backflow in the domain derived from the solution proposed [EMBH+11]. A 3-element Windkessel model was applied on each outlet

[MBRvdV11, VCFJT10] (see Figure 3.1). Model parameters were chosen according to [XHF13] study.

Flow regime

Reynold numbers in our simulations were within the physiological range [FA01], varying from 1,634 to 1,954 at the proximal inlet. Womersley numbers at the proximal inlet varied from 10.00 to 14.97, which was within the physiological range [MMKB94]. Blood was modelled as an homogeneous non-Newtonian fluid following the Quemada model [Bia13, MGGE+07]. Model parameters were chosen according to the study of [BKC00], based on the rheological data from [MK96]. Expressed a modified Casson model, the viscosity can be written as: $\eta = \left(\sqrt{(}\eta_\infty) + \frac{\sqrt{\tau_0}}{\sqrt{\lambda}+\sqrt{\dot{\gamma}}}\right)^2$ With η the apparent viscosity, $\dot{\gamma}$ the shear rate, η_∞ the viscosity when $\dot{\gamma} \to \infty$, τ_0 the shear stress when $\dot{\gamma} \to 0$ and λ the characteristic time. Numerical values are $\eta_\infty = 0.002654\,Pa/s$; $\tau_0 = 0.004360 Pa/s$ and $\lambda = 0.02181 s^{-1}$ [BKC00].

Numerical methods

The domain was discretized using a polyhedral mesh with an average of 463000 elements (SD : 51470; range: $408570 - 568026$). Navier-Stokes equations were discretized with finite volume methods (FVM) implemented in the *OpenFOAM* toolbox [JW00, Jas96]. The solver used is a large time-step transient solver for incompressible for solving pressure–velocity coupling, using the PIMPLE (merged PISO-SIMPLE) algorithm. Simulations were initialized using first order schemes in time (Euler) and space (Gauss upwind) up to temporal convergence. Second order schemes in time (Crank Nicolson) and space (Gauss linear upwind) were then used up to temporal convergence. The time step of the simulation was automatically adapted to keep the CFL [Coa03] condition below 1, leading to approximately mean time step size of $3.9.10^{-4}$ s (SD : $2.23.10^{-4}$; range: $1.15.10^{-4}$ – $9.25.10^{-4}$). Temporal convergence verification was performed on the velocity at a control

location in the AAA between consecutive cardiac cycles. It was achieved after 5-7 cardiac cycles [1]. To sum-up:

- each time steps is fully converged under chosen residuals criteria, i.e. 10^{-6} for pressure and 10^{-8} for velocity.
- each cardiac pulse is similar to the previous one. See chapter 4 for more details.
- the solution is independent to further mesh refinement, computed using the Grid Convergence Index (GCI) see Table 3.I

We accessed resources from Calcul Québec and Compute Canada [2] for FVM computations.

	U	WSS	p
GCI_{12} (%)	18.9	19.73	6.58
GCI_{23} (%)	0.94	4.30	0.23

Table 3.I – Grid Convergence Index pour the blood velocity, wall shear stress and pressure on a local probing domain (in the AAA sack for **U** and p and small surface domain on the AAA wall for the WSS) for three mesh sizes : 183406, 336159 and 641139 volume elements.

3.2.2 CFD comparison with MRI velocimetry

MRI acquisitions were validated on a 3T magnet (Achieva X-Series, Philips Medical, Eindhoven, Netherlands) with 16-channel abdominal antenna and phase-contrast velocity sequence. Blood velocities in 4 volunteer patients were measured on AAA cross-sections orthogonal to maximal diameter ($D_{max} = 44.7 \pm 8.33$mm) and proximal neck. Because of breathing artefacts, technically-successful acquisitions were obtained on only 6 slices for the 4 AAA patients investigated by MRI (Figure 3.3, left column).

1. See Figure 4.6
2. The operation of the supercomputer used is funded by the Canada Foundation for Innovation (CFI), NanoQuébec, RMGA and the Fonds de recherche du Québec - Nature et technologies (FRQNT).

MRI spatial resolution was $1.6 \times 1.6 \times 6\,\mathrm{mm}^3$, the temporal resolution $1/8^{th}$ of the cardiac period and grid size 256×25. The chosen velocity encoding was $2\,\mathrm{m\,s}^{-1}$ to encompass the highest velocity likely to be met in the aorta and was not exceeded. Three velocity components were measured in each slice. Aortic flow was assumed to be periodic during MRI acquisition (ECG-gating). Since respiratory gating was not available, patients were asked, if possible, to hold their breath during acquisitions, i.e., for at least 20 s.

In addition, the lumen was segmented to evaluate its section variation over time (Figure 3.2 3). Two healthy volunteers (35 ± 1.4 years old) were investigated as controls. Section surfaces were evaluated at maximal and proximal diameters of the 5 AAA and at mid-distance between the lowest renal artery and iliac bifurcation, approximately 2 cm under the lowest renal artery of the 2 healthy subjects.

3.2.3 Transport quantification

Flow in AAA is often characterized by the presence of jet cores [AS12, BGA+10, SSL04, SMPK11], creating a coherent vortex in their wake [BHCG11]. Zones of low shearing and low stretching, isolated by the repelling surface, lie between the jet cores and dilated aortic wall. Repelling LCS can thus mark the boundaries of stagnant flow [SA14], the feature of interest in the present study.

LCS extraction has proven to be an efficient tool for the visualization of transport structures in biomedical [SA14], industrial [SCF+12] and environmental [Pra14] contexts. LCS are not only a convenient way to observe transport barriers in flow, but they also help investigate the transport of unsteady flows where conventional techniques may fail [Sha11]. FTLE field trenches bounded by repelling hyperbolic LCS have already been successful in viewing bioaccumulation in oceanic flows [OBVBK08].

LCS were extracted from the FTLE field [AP15]. Given λ_{max}, maximal eigenvalue of the Cauchy-Green tensor of flow, the largest stretching at location x_0, was $\sqrt{\lambda_{max}(x_0)}$.

Such exponentially-evolving stretching, FTLE at x_0, was defined as:

$$\sigma_{t_0}^{T}(x_0) = \frac{1}{|T|} \ln \sqrt{\lambda_{max}(x_0)}$$

With $\sigma_{t_0}^{T}(x_0)$ the FTLE field where particles where advected from the time t_0 to $t_0 + T$, starting at the location x_0.

To compute the Cauchy-Green deformation tensor, trajectories of particles seeded in each point of the grid were integrated over time with a Runge-Kutta integrator onto a sub-grid with $0.25 \times 0.25 \times 0.25$ mm^3 resolution. An auxiliary grid ($0.1 \times 0.1 \times 0.1$mm^3) was considered for the Cauchy-Green tensor computation. Particles were advected backward in time to obtain attractive LCS [ST08]. Integration time T of 1.5 s allowed most particles to leave the domain [ST08]. FLTE computations were performed with *VisIt* [CBW+12] on a subdomain of the initial CFD domain (Figure 3.4), in the AAA portion located between the lowest renal artery and the iliac bifurcation.

LCS ridges were computed as dot products of eigenvalues of the Hessian of FTLE [SLM05].

Since flow topology varied highly over cardiac cycles, LCS did not necessarily close domain boundaries completely (Figure 3.5). To close volumes of interest (stagnation volumes), as we assumed them to be smooth and continuous, a region-growing segmentation method [PXP00] was chosen, with *ITKSnap* [YPH+06]. This region-growing method works well on continuous fields. Yet, LCS are an ensemble of disconnected 3D surfaces in AAA. Consequently, LCS barriers were added to FTLE field AAA to produce a new, continuous, smooth FTLE field, aFTLE. Initial seeding points were placed visually by the operator, and segmentation was allowed to grow until no change was seen.

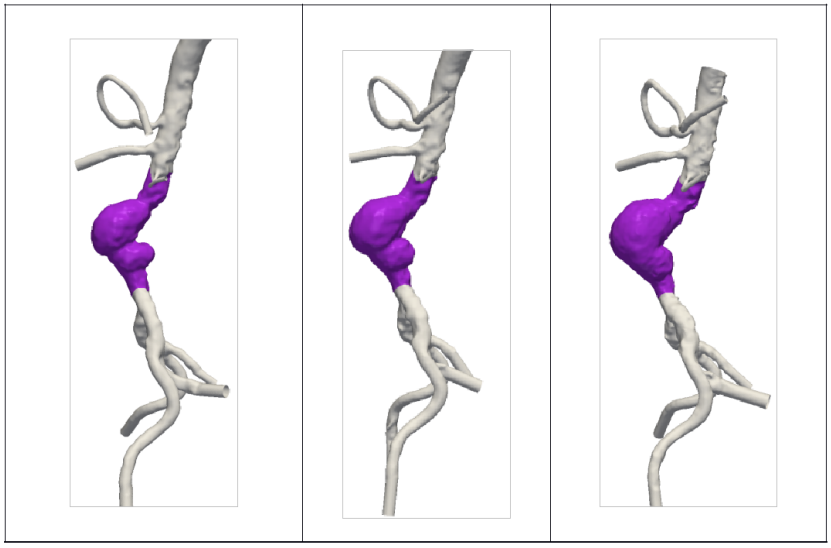

Figure 3.4 – Result of the automated selection of the domain of interest, based on the position of the lowest renal artery and the iliac bifurcation for the CT of 2006 (left), 2009 (center), and 2012 (right).

3.3 Results

3.3.1 MRI velocimetry

CFD validation

Figure 3.3 illustrates the localization of the slices used to compare experimental data to the simulation results. The velocity magnitude obtained from reconstruction of PC-MRI data at systolic peaks is compared to the simulated data for each slice and a cross-correlation value is computed. Experimental and simulated data are visually consistent, and cross correlation of velocity magnitude confirmed good representation of flow topology. 2D maximum cross-correlation coefficients ranged between 0.65, 0.86, and 0.082 (min, max, SD).

These results show that generic boundary conditions and blood rheology used in the computation of the CFD model are consistent for the analysis of AAA flow topology.

Rigid wall hypothesis validation

Lumen segmentation during different phases of the cardiac cycle gave an estimation of

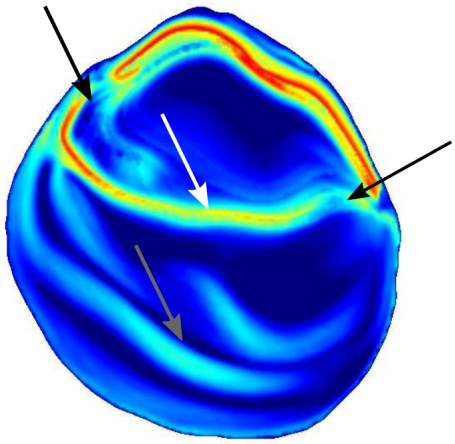

Figure 3.5 – Axial slice of the FTLE field in the AAA (D_{max} location). Main separatrice (white arrow), secondary separatrices (grey arrow), and separatrice discontinuities (black arrows).

wall compliance and AAA size lumen variation. Relative surface section variation during 1 cardiac cycle was plotted in Figure 3.2. As expected from the literature [vtVBM+08], patient age correlated to aorta wall stiffening led to small cross-sectional surface variation of 0.78 ± 0.54 % and 1.82 ± 0.96 % at D_{max} location and at proximal neck respectively. As expected, for healthy patients, the aorta surface variation is greater: 7.95 ± 4.41 % and 7.47 ± 4.00 % and D_{max} location at proximal neck respectively. The small change in wall deformation during cardiac pulse motivated the choice of a rigid wall model for AAA of elderly patients.

3.3.2 LCS

The morphology of the AAA case-study, followed by CTA during 8 years, presented 2 main bulges, a big one on the anterior side and a smaller one on the posterior (Figure 3.4).

The smaller one (posterior side), close to the spine, flattened slightly with time. The larger one, on the anterior side, grew over time in the direction of the abdominal cavity. These 2 bulges were the locations of recirculation zones secondary to jets created at the exit of the AAA proximal neck. These recirculation zones formed during peak-systole, when blood rapidly entered the dilated section of the AAA, forming Lagrangian jet cores. LCS from repelling FTLE (which characterizes stagnant flow) enclosed the AAA bulge areas, dividing the flow domain into 3 sub-domains (Figure 3.6, top left): 2 isolated stagnation volumes and 1 stretched domain connecting the inlet to the outlet of the AAA (freely-circulating blood). Smaller barriers were visible inside these zones and denoted the presence of enclosed transport features (Figure 3.7). Figure 3.8 illustrates how the observation of instantaneous flow contrasts with hyperbolic LCS.

3.3.3 Evolution of transport during patient follow-up

The 2 main stagnation zones were well discernible in all 9 simulations. Although their volumes increased (Figure 3.9), their localization and overall shape remained unchanged. Even though LCS did not always provide perfectly-closed volumes, segmentation remained reproducible. On the first CT-scan, 3 segmentations were performed in each stagnation zone 3 times per 3 users: intra-user variability on volume was -3.46, 4.03, 3.91 and inter-user variability was -1.22, 1.08, and 1.16 (min, max, SD, in %). The smallest stagnation zone grew linearly from 1.81 to 4.11 cm^3 in 8 years (127 % increase, Figure 3.6), and the largest, from 16.17 to 63.66 cm^3 (293 % increase, Figure 3.6). Growth of both the large and small stagnation zones are correlated with lumen dilation (Pearson's r = 0.99, p=0.0004 and 0.93, p=0.002, respectively). Average yearly growth rates were 8.14, 6.08 and 0.28 $\mathrm{cm}^3\,\mathrm{yr}^{-1}$ (r^2= 0.99, 0.84 and 0.98) for the lumen, large and small stagnation zones, respectively, (see Figure 3.6). The circulating zone, connecting the AAA inlet to the outlet, was only weakly correlated to lumen growth (r^2= 0.52). Lumen growth was mostly composed of stagnation zones while the volume contributing to transport remains

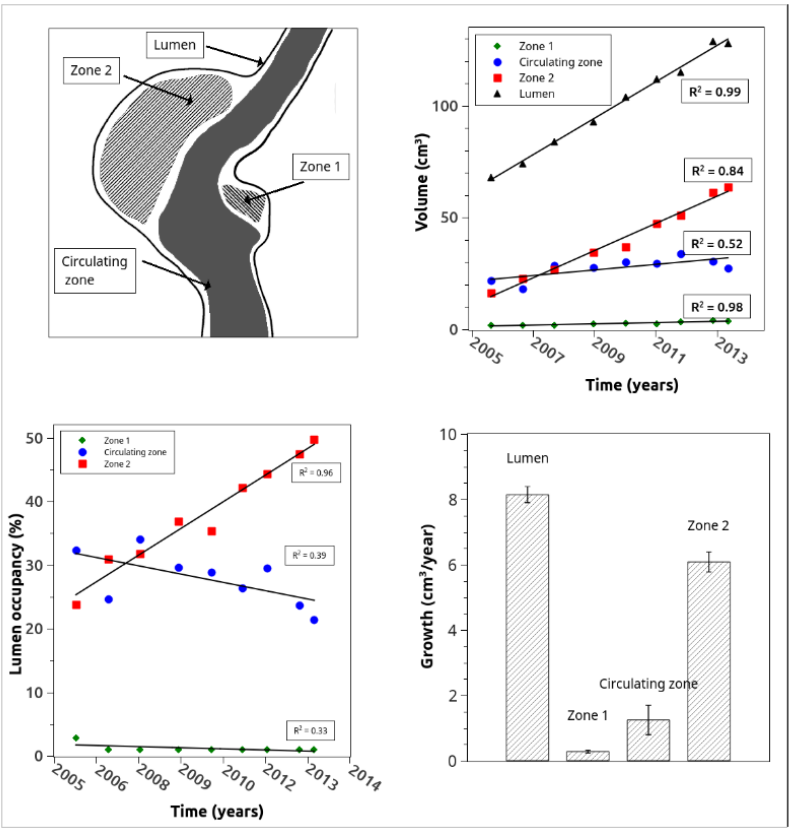

Figure 3.6 – Top left: Sagittal view of the schematized dynamically isolated zone in the AAA lumen; top right: volume evolution over time of the three dynamically isolated zones and the whole lumen with linear fits; bottom left: volume of the dynamically isolated zones compared the whole lumen and bottom right: growth speed of the four zones based on the linear fit on their temporal growth.

barely affected by it.

3.4 Discussion

The aorta's role is to deliver oxygenated blood and nutrients as well as to remove waste products. Transport performance between blood and vessel wall is dictated by transit through the artery surface and fluid mechanics [Tar03]. With abdominal aortae losing their straight tubular shape with aging or aneurysm progression, blood flow topology is expected to change from its original state. The current study aims to provide an efficient

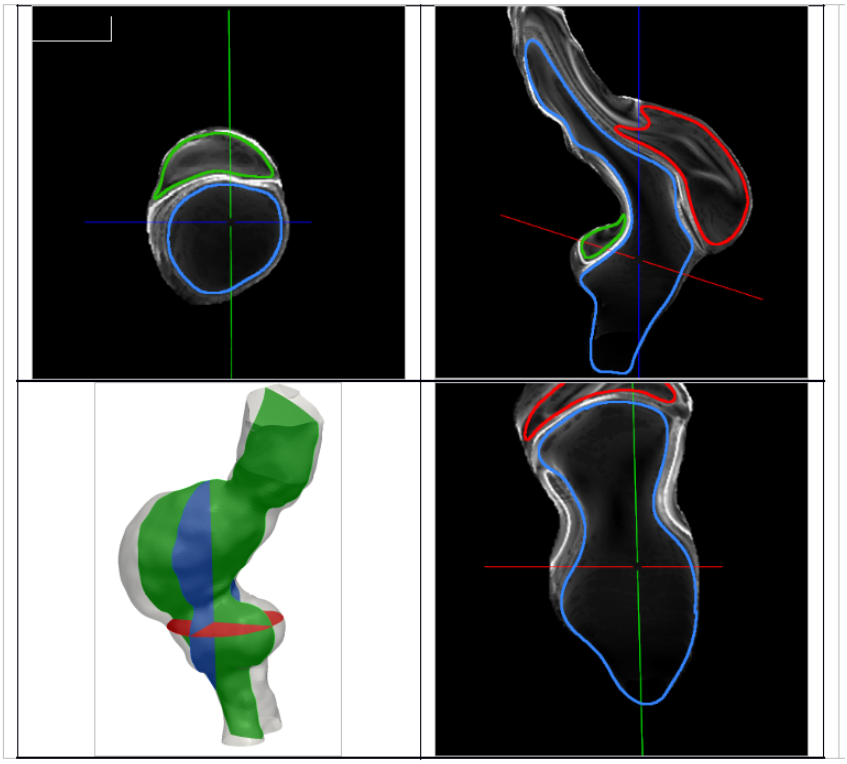

Figure 3.7 – Coronal, axial and sagittal view of the aFTLE field in the lumen with dynamically isolated zones superimposed over (2006 follow-up). Lower left view shows the cut planes on the lumen geometry.

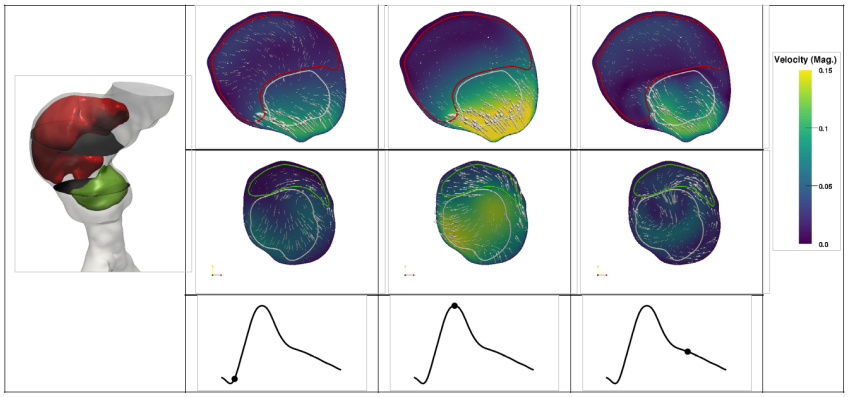

Figure 3.8 – Blood flow velocity magnitude and in plane vectors at two locations and three times. In overlay the two stagnation zones (red and green) and the circulation domain (white). The instantaneous velocity fields do not coincide with the extracted frontiers in the context of a pulsatile flow.

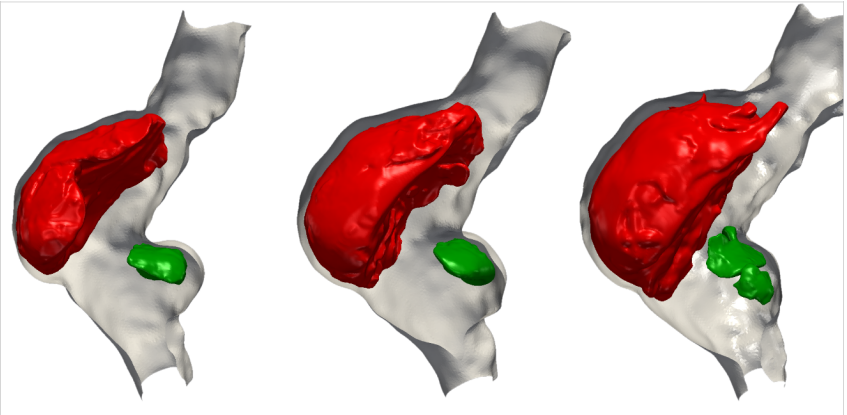

Figure 3.9 – Posterior (red) and anterior (green) segmented stagnation domains in 2006, 2009 and 2012.

methodology to locate and quantify transport topology alterations. The first step was to validate that our computation CFD model is consistent for the analysis of AAA flow topology using MRI velocimetry on four patient followed for AAA. Based on this flow model, dynamically-isolated zones were extracted from the flow simulation performed on 9 scans of 1 patient followed clinically with an unrepaired AAA. Patient-specific geometric models were constructed from 3D CTA of the aorta. Transport barriers were reconstructed inside the lumen from the transient flow field.

Blood flow was solved using FVM with boundary conditions build from patient specific data by [XHF13] and was confirmed by PC-MRI.

Even though the location of 2 dynamically-isolated zones in the area of luminal dilatation could be guessed, their volume and boundaries could now be computed. Furthermore, stagnation in the bulbous part of the AAA was witnessed with particle residence times [SLT+11]. It was observed that the domain connecting the proximal to the distal neck in the lumen remained unperturbed and formed an effective circulation path in the entire lumen. Its approximately constant volume during entire follow-up went along with constant perfusion needed for the pelvic organs and lower limbs. The quasi-linear growth of the AAA agreed with the observations of [ZGL+16] in 14 followed patients.

LCS-based methods have previously been applied to study flow in AAA [ST08] and

various other domains [Hal15, SCF+12]. In this AAA case-study, barriers between stagnation and circulating zones were highlighted in the lumen geometry, given the fact that the FTLE field was constructed from stretching between adjacent fluid particles. Distinct barriers to flow appeared as the arterial lumen dilated and became tortuous. Age could have been the initial insult, as buckling of the artery wall appears with loss of elastin and resulting lengthening [LH12]. Particles traveling along LCS may be subject to high shearing, the cause of platelet activation. If activated, i.e., subjected to a certain shear stress level for long enough [RZM79, WOBSS85], platelets entering stagnation zones are likely to adhere to the wall and create a substrate favourable to thrombus deposition. Low shear stress may also be a condition necessary for platelet adhesion [BGA+10] which happens in stagnation zones. Portions of the wall exposed to low shear can be visualized as time average wall shear stress and linked to thrombus deposition [ZGL+16]. However, this only accounts for part of the adhesion mechanism. Looking at the aorta location exposed to stagnation zones could be an additional complete predictor of intra-luminal thrombus (ILT) deposition.

Thrombus covering the AAA wall will accelerate its degeneration. An important outcome is the increase of elastase and thus the rate of elastin destruction. ILT presence is potentially linked with local hypoxia and inflammation of the underlying wall [TH15]. In addition, ILT thickness is correlated to smooth muscle cell apoptosis, elastin degradation and MMP-2 concentration, relative to mechanical stability, accelerating AAA growth. During the cardiac cycle, ILT may partly withstand the mechanical load due to blood flow. In parallel, increased pressure load on the wall promotes the synthesis of collagen and proteoglycans, consequently approaching the AAA wall rupture limit [TGP+15]. However, wall degradation is mostly active in areas covered by thin ILT, barely quantifiable by CTA [WSS+10].

In the AAA studied, in the first CTA the ILT thickness was too low to be segmented. Thin ILT was nevertheless visible, facing both stagnation zones (Figure 3.10) but did not cover a large part of the lumen, as seen in most AAA [ZGL+16]. However, even

in the early stage, this AAA presented well-defined dead circulation zones in bulging areas, as shown Figure 3.9. Even though platelet-endothelial cell adhesion is lower than platelet-fresh ILT adhesion, trapped and shear-activated platelets [BKHF11] slowly formed a thrombus layer over the wall. ILT will then grow from this location, because of platelet thrombus affinity, progressively filling existing concavity. Blood pressure and high flow rate will prevent lumen section reduction to preserve pelvis and lower limb perfusion. This minimal size could match the computed circulation zone, approximately constant with time (Figure 3.6). Zambrano et al. [ZGL+16] studied fast-growing AAA and observed constant diameter of the lumen section whereas D_{max} progression was related to thrombus growth.

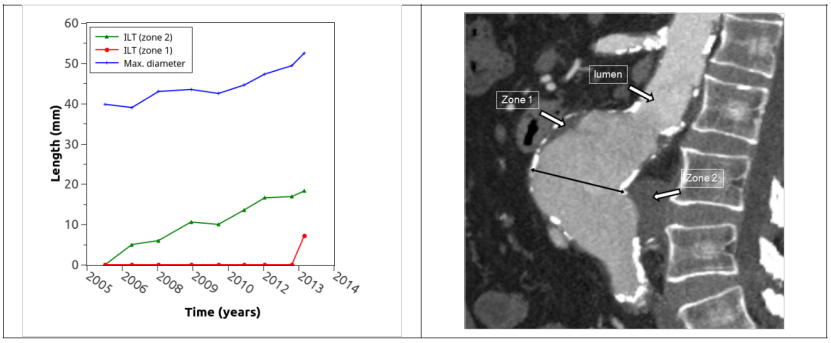

Figure 3.10 – Evolution with time of the maximal thickness of the two ILT (ILT 1 facing the stagnation zone 1 and ILT 2 facing the stagnation zone 2). The ILT zone 1 was not thick enough before 2013 to be measured and segmented on the CT-A. The maximal diameter was measured on the CTA by a radiologist (black line).

The most common way to study the role of blood circulation in AAA physiology is through WSS and WSS derivative. However, an AAA with or without ILT should not be considered the same way: in the absence of ILT, the flow exposed endothelium may be able to trigger vascular mechano-adaptation in response to flow modification. In contrast, in the presence of ILT, the WSS could be an indicator of platelet adhesion risk. Portions of the aorta covered by ILT and those without ILT presenting atherosclerotic plaques give totally different roughness data. This textural information is not visible on

spatial resolution by CTA. Nevertheless, it is crucial for WSS numerical computation and constitutes a limitation of this approach. However, looking at the transport field limits the impact of the near wall lack of information.

Recent progress in multiphysics coupling allows the simulation of thrombus deposition and growth as proven by [MX16] and [BSSCG12]. This gives direct information on the portion of the lumen exposed to it and the progressive alteration of the flow field. However, thrombus formation in the AAA is a long term process going with the deformation of the arterial wall, not considered in cited models. Alternatively, growth and remodelling of the lumen model exist [GWH15] but do not include thrombus development. Extracting the dynamically isolated zones on the other hand do not require extensive hypothesis on the biological process of thrombus formation but gives information on the severity of the alteration of the flow and, as such, metrics for AAA classification.

A long-term challenge is to understand the mechanisms promoting AAA growth – to improve patient management, especially regarding eligibility and timing for open or endovascular repair. The measurement of AAA D_{max}, in multiplanar CT-scans, is the current way to assess AAA growth and growth rate over time in clinical studies. This 1-D measurement, however, cannot reflect the changes observed in complex AAA geometry.

3.5 Limitation

Extraction of dynamically isolated zones requires a realistic flow field as support. This retrospective study relied on CT-scans acquired over a time span of 8 years and no flow information was recorded at the time. Generic simulation parameters were therefore used. This point has no influence on the presented workflow but the results, such as the shape and size of the dynamically isolated zones, can be altered. Numerical [LSF+10] and experimental [PRB04] studies show the presence of mild turbulence in AAA of patient at rest, increasing with exercise. Turbulence in AAA will likely shrink recirculation zones [BNSD96] compared to our laminar simulation. At the inlet, the Wormersley velocity

profile was enforced with no rotational component. To the knowledge of the authors, no general model exists other than modelling the whole circulation upstream the aneurysm, including the aortic arch. Helicity was however measured [MPR+09, MPR+11] and its role on the dynamically isolated zones should be investigated.

Recent work on transport proposes more robust methods for material surface extraction [Hal15] not based on FTLE, allowing the visualization of hyperbolic but also parabolic and elliptic LCS [Hal15]. Elliptic LCS may allow skipping the segmentation step because by definition when hyperbolic LCS are formed from Lagrangian jet cores it forms closed domains. As jet cores are interesting as a typical feature of AAA [ADES12, AS12], both hyperbolic and elliptic LCS should be studied. Although not the most reliable mathematical tools to extract LCS, Shadden and Taylor [ST08] demonstrated the ability of the method to capture transport boundaries in the specific context of biological flow.

3.6 Conclusion

A computation flow dynamic model applicable to AAA was proposed and presented good agreement with MRI velocimetry. Transient flow transport topology evolution in this model was computed on an AAA over the span of 8 years and 9 CT-scans. Lumen geometries were reconstructed from injected CT images and transient flow simulated with FVM. The presented workflow allowed extraction of blood flow stagnation zones in an AAA and studied their evolution during its growth, with only clinically-available data. The steps to accomplish this goal are summarized below:

1. Flow computation:

   (a) CT-scans with contrast agent are segmented by a region-growing approach. The geometry thus obtained is meshed with polyhedral elements (between $\approx 500k$ and $\approx 750k$ volume element) and boundary conditions are set.

   (b) Navier-Stokes equations are solved over the domain until convergence with a transient flow inlet and 0-D outlets.

(c) The resulting flow velocity fields are validated with MRI velocimetry.

2. Stagnation zone extraction:

(a) Stagnation zones are segmented from the FTLE field, by edge-based pre-processing. The FTLE field is convoluted with computed LCS.

The proposed workflow provides a solution to not only visualize but also quantify the dynamically isolated zones of the blood flow in aneurysms. The identification of these stagnation zones can be performed with routine medical imaging in AAA patients. This opens the door for large scale comparative studies to improve our understanding on the role of flow topology and transport on ILT formation and their association with AAA growth and vulnerability.

3.7 Acknowledgments

The authors thank Michel Gouin for experimental data acquisition. They also acknowledge the volunteers who gave their time for MRI measurements. The presented work relied highly on open-source projects, especially *OpenFOAM* (http://www.openfoam.com/) and ITKSnap (http://www.itksnap.org), and the whole community behind them.

BIBLIOGRAPHY

ADES12. Amirhossein Arzani, Petter Dyverfeldt, Tino Ebbers, and Shawn C. Shadden. In vivo validation of numerical prediction for turbulence intensity in an aortic coarctation. *Annals of Biomedical Engineering*, 40(4):860–870, 2012.

AP15. Michael R. Allshouse and Thomas Peacock. Refining finite-time Lyapunov exponent ridges and the challenges of classifying them. *Chaos*, 25(8):087410, 2015.

AS12. Amirhossein Arzani and Shawn C. Shadden. Characterization of the transport topology in patient-specific abdominal aortic aneurysm models. *Physics of Fluids*, 24(8):81901, 8 2012.

BCH+03. David C. Brewster, Jack L. Cronenwett, John W. Hallett, K. Wayne Johnston, William C. Krupski, and Jon S. Matsumura. Guidelines for the treatment of abdominal aortic aneurysms: Report of a subcommittee of the Joint Council of the American Association for Vascular Surgery and Society for Vascular Surgery. *Journal of Vascular Surgery*, 37(5):1106–1117, 2003.

BGA+10. Jacopo Biasetti, T. Christian Gasser, Martin Auer, Ulf Hedin, and Fausto Labruto. Hemodynamics of the normal aorta compared to fusiform and saccular abdominal aortic aneurysms with emphasis on a potential thrombus formation mechanism. *Annals of Biomedical Engineering*, 38(2):380–390, 2 2010.

BHCG11. Jacopo Biasetti, Fazle Hussain, and T. Christian Gasser. Blood flow and coherent vortices in the normal and aneurysmatic aortas: A fluid dynamical approach to intraluminal thrombus formation. *Journal of the Royal Society Interface*, 8(63):1449–1461, 10 2011.

Bia13. Jacopo Biasetti. *Physics of blood flow in arteries and its relation to intra-luminal thrombus and atherosclerosis*. PhD thesis, KTH School of Engineering Sciences, 2013.

BKC00. J. R. Buchanan, C. Kleinstreuer, and J. K. Comer. Rheological effects on pulsatile hemodynamics in a stenosed tube. *Computers and Fluids*, 29(6):695–724, 2000.

BKHF11. C. Basciano, C. Kleinstreuer, S. Hyun, and E. A. Finol. A relation between near-wall particle-hemodynamics and onset of thrombus formation in abdominal aortic aneurysms. *Annals of Biomedical Engineering*, 39(7):2010–2026, 9 2011.

BNSD96. D. Bluestein, L. Niu, R. T. Schoephoerster, and M. K. Dewanjee. Steady Flow in an Aneurysm Model: Correlation Between Fluid Dynamics and Blood Platelet Deposition. *Journal of Biomechanical Engineering*, 118(3):280, 1996.

BSSCG12. Jacopo Biasetti, Pier Giorgio Spazzini, Jesper Swedenborg, and T. Christian Gasser. An integrated fluid-chemical model toward modeling the formation of intra-luminal thrombus in abdominal aortic aneurysms. *Frontiers in Physiology*, 3 JUL:266, 7 2012.

CBD+09. Elliot L. Chaikof, David C. Brewster, Ronald L. Dalman, Michel S. Makaroun, Karl A. Illig, Gregorio A. Sicard, Carlos H. Timaran, Gilbert R. Upchurch, and Frank J. Veith. The care of patients with an abdominal aortic aneurysm: The Society for Vascular Surgery practice guidelines. *Journal of Vascular Surgery*, 50(4):S2–S49, 2009.

CBW+12. Hank Childs, Eric Brugger, Brad Whitlock, Jeremy Meredith, Sean Ahern, David Pugmire, Kathleen Biagas, Mark Miller, Cyrus Harrison, Gunther H

Weber, Hari Krishnan, Thomas Fogal, Allen Sanderson, Christoph Garth, E Wes Bethel, David Camp, Oliver Rübel, Marc Durant, Jean Favre, and Paul Návratil. VisIt: An end-user tool for visualizing and analyzing very large data. *High Performance Visualization–Enabling Extreme-Scale Scientific Insight*, (1):357–372, 2012.

Coa03. K.H. Coats. IMPES Stability: The CFL Limit. *SPE Journal*, 8(03):291–297, 2003.

DMS13. Vincent Duvernois, Alison L. Marsden, and Shawn C. Shadden. Lagrangian analysis of hemodynamics data from FSI simulation. *International Journal for Numerical Methods in Biomedical Engineering*, 29(4):445–461, 2013.

EMBH$^+$11. Mahdi Esmaily Moghadam, Yuri Bazilevs, Tain Yen Hsia, Irene E. Vignon-Clementel, and Alison L. Marsden. A comparison of outlet boundary treatments for prevention of backflow divergence with relevance to blood flow simulations. *Computational Mechanics*, 48(3):277–291, 2011.

FA01. Ender A. Finol and Cristina H. Amon. Blood flow in abdominal aortic aneurysms: pulsatile flow hemodynamics. *Journal of biomechanical engineering*, 123(5):474–484, 10 2001.

Ger13. Liesbet Geris. *Computational Modeling in Tissue Engineering*, volume 10 of *Studies in Mechanobiology, Tissue Engineering and Biomaterials*. Springer Berlin Heidelberg, Berlin, Heidelberg, 2013.

GWH15. Andrii Grytsan, Paul N. Watton, and Gerhard A. Holzapfel. A Thick-Walled Fluid–Solid-Growth Model of Abdominal Aortic Aneurysm Evolution: Application to a Patient-Specific Geometry. *Journal of Biomechanical Engineering*, 137(3):031008, 2015.

Hal11. George Haller. A variational theory of hyperbolic Lagrangian Coherent Structures. *Physica D: Nonlinear Phenomena*, 240(7):574–598, 2011.

Hal15. George Haller. Lagrangian Coherent Structures. *Annual Review of Fluid Mechanics*, 47(1):137–162, 1 2015.

HFC+08. Michael S. Heng, Michael J. Fagan, Jason W. Collier, Grishma Desai, Peter T. McCollum, and Ian C. Chetter. Peak wall stress measurement in elective and acute abdominal aortic aneurysms. *Journal of Vascular Surgery*, 47(1):17–22, 1 2008.

HGT+15. Julie Hallet, Brice Gayet, Allan Tsung, Go Wakabayashi, and Patrick Pessaux. Systematic review of the use of pre-operative simulation and navigation for hepatectomy: Current status and future perspectives. *Journal of Hepato-Biliary-Pancreatic Sciences*, 22(5):353–362, 5 2015.

Jas96. Hrvoje Jasak. *Error Analysis and Estimation for the Finite Volume Method with Applications to Fluid Flows*. PhD thesis, Imperial College, University of London, 1996.

JW00. H. Jasak and H. G. Weller. Application of the finite volume method and unstructured meshes to linear elasticity. *International Journal for Numerical Methods in Engineering*, 48(2):267–287, 2000.

KYM+93. P. J. Kilner, G. Z. Yang, R. H. Mohiaddin, D. N. Firmin, and D. B. Longmore. Helical and retrograde secondary flow patterns in the aortic arch studied by three-directional magnetic resonance velocity mapping. *Circulation*, 88(5 I):2235–2247, 11 1993.

LAS09. Sang-Wook Lee, Luca Antiga, and David A. Steinman. Correlations Among Indicators of Disturbed Flow at the Normal Carotid Bifurcation. *Journal of Biomechanical Engineering*, 131(6):061013, 6 2009.

LH12. Qin Liu and Hai Chao Han. Mechanical buckling of artery under pulsatile pressure. *Journal of Biomechanics*, 45(7):1192–1198, 2012.

LSF+10. Andrea S. Les, Shawn C. Shadden, C. Alberto Figueroa, Jinha M. Park, Maureen M. Tedesco, Robert J. Herfkens, Ronald L. Dalman, and Charles A. Taylor. Quantification of hemodynamics in abdominal aortic aneurysms during rest and exercise using magnetic resonance imaging and computational fluid dynamics. *Annals of Biomedical Engineering*, 38(4):1288–1313, 2010.

MBRvdV11. G. Mulder, A. C B Bogaerds, P. Rongen, and F. N. van de Vosse. The influence of contrast agent injection on physiological flow in the circle of Willis. *Medical Engineering and Physics*, 33(2):195–203, 2011.

McG11. Tim M McGloughlin. *Biomechanics and Mechanobiology of Aneurysms*, volume 7 of *Studies in Mechanobiology, Tissue Engineering and Biomaterials*. Springer Berlin Heidelberg, Berlin, Heidelberg, 2011.

MGG+70. C. J. Mills, I. T. Gabe, J. H. Gault, D. T. Mason, J. Ross, E. Braunwald, and J. P. Shillingford. Pressure-flow relationships and vascular impedance in man. *Cardiovascular Research*, 4(4):405–417, 1970.

MGGE+07. Anna Marcinkowska-Gapińska, Jacek Gapinski, Waldemar Elikowski, Feliks Jaroszyk, and Leszek Kubisz. Comparison of three rheological models of shear flow behavior studied on blood samples from post-infarction patients. *Medical and Biological Engineering and Computing*, 45(9):837–844, 2007.

MK96. E W Merrill and M. Kaibara. Rheology of blood. *Biorheology*, 33(2):101–117, 1996.

MMKB94. J.E. E. Moore, S.E. E. Maier, D.N. N. Ku, and P. Boesiger. Hemodynamics in the abdominal aorta: A comparison of in vitro and in vivo measurements. *J Appl Physiol*, 76(4):1520–1527, 4 1994.

MPR+09. Umberto Morbiducci, Raffaele Ponzini, Giovanna Rizzo, Marcello Cadioli, Antonio Esposito, Francesco De Cobelli, Alessandro Del Maschio, Franco Maria Montevecchi, and Alberto Redaelli. In vivo quantification of helical blood flow in human aorta by time-Resolved three-dimensional cine phase contrast magnetic resonance imaging. *Annals of Biomedical Engineering*, 37(3):516–531, 3 2009.

MPR+11. Umberto Morbiducci, Raffaele Ponzini, Giovanna Rizzo, Marcello Cadioli, Antonio Esposito, Franco Maria Montevecchi, and Alberto Redaelli. Mechanistic insight into the physiological relevance of helical blood flow in the human aorta: An in vivo study. *Biomechanics and Modeling in Mechanobiology*, 10(3):339–355, 6 2011.

MX16. Claudia Menichini and Xiao Yun Xu. Mathematical modeling of thrombus formation in idealized models of aortic dissection: initial findings and potential applications. *Journal of Mathematical Biology*, 73(5):1205–1226, 11 2016.

NZS+13. Marco Nolden, Sascha Zelzer, Alexander Seitel, Diana Wald, Michael Müller, Alfred M. Franz, Daniel Maleike, Markus Fangerau, Matthias Baumhauer, Lena Maier-Hein, Klaus H. Maier-Hein, Hans Peter Meinzer, and Ivo Wolf. The medical imaging interaction toolkit: Challenges and advances: 10 years of open-source development. *International Journal of Computer Assisted Radiology and Surgery*, 8(4):607–620, 2013.

OBVBK08. M. J. Olascoaga, F. J. Beron-Vera, L. E. Brand, and H. Koçak. Tracing the early development of harmful algal blooms on the West Florida Shelf with the aid of Lagrangian coherent structures. *Journal of Geophysical Research: Oceans*, 113(12), 2008.

OGD+92. Kenneth Ouriel, Richard M. Green, Carlos Donayre, Cynthia K. Shortell,

Janice Elliott, and James A. DeWeese. An evaluation of new methods of expressing aortic aneurysm size: Relationship to rupture. *Journal of vascular surgery*, 15(1):12–20, 1 1992.

PH13. Thomas Peacock and George Haller. Lagrangian coherent structures: The hidden skeleton of fluid flows. *Physics Today*, 66(2):41–47, 2013.

Pra14. S. V. Prants. Chaotic Lagrangian transport and mixing in the ocean. *European Physical Journal: Special Topics*, 223(13):2723–2743, 12 2014.

PRB04. Robert A. Peattie, Tiffany J. Riehle, and Edward I. Bluth. Pulsatile Flow in Fusiform Models of Abdominal Aortic Aneurysms: Flow Fields, Velocity Patterns and Flow-Induced Wall Stresses. *Journal of Biomechanical Engineering*, 126(4):438, 8 2004.

PSW13a. Veronique Peiffer, Spencer J. Sherwin, and Peter D. Weinberg. Does low and oscillatory wall shear stress correlate spatially with early atherosclerosis? A systematic review, 2013.

PSW13b. Véronique Peiffer, Spencer J. Sherwin, and Peter D. Weinberg. Computation in the rabbit aorta of a new metric - the transverse wall shear stress - to quantify the multidirectional character of disturbed blood flow. *Journal of Biomechanics*, 46(15):2651–2658, 2013.

PXP00. Dzung L. Pham, Chenyang Xu, and Jerry L. Prince. Current Methods in Medical Image Segmentation. *Annual Review of Biomedical Engineering*, 2(1):315–337, 2000.

RKCdT$^+$06. Madhavan L. Raghavan, Jarin Kratzberg, E. M. Castro de Tolosa, Mauro M. Hanaoka, Patricia Walker, Erasmo Simão da Silva, Erasmo Magalhães Castro de Tolosa, Mauro M. Hanaoka, Patricia Walker, and Erasmo Simão da Silva.

Regional distribution of wall thickness and failure properties of human abdominal aortic aneurysm. *J Biomech*, 39(16):3010–3016, 2006.

RMP+13. C. Reeps, A. Maier, J. Pelisek, F. Härtl, V. Grabher-Meier, W. A. Wall, M. Essler, H. H. Eckstein, and M. W. Gee. Measuring and modeling patient-specific distributions of material properties in abdominal aortic aneurysm wall. *Biomechanics and Modeling in Mechanobiology*, 12(4):717–733, 2013.

RZM79. J. M. Ramstack, L. Zuckerman, and L. F. Mockros. Shear-induced activation of platelets. *Journal of Biomechanics*, 12(2):113–125, 1979.

SA14. Shawn C. Shadden and Amirhossein Arzani. Lagrangian Postprocessing of Computational Hemodynamics. *Annals of Biomedical Engineering*, 43(1):41–58, 1 2014.

SCF+12. Benjamin Schindler, Ieee Cs, Raphael Fuchs, Stefan Barp, Armin Pobitzer, and Robert Carnecky. Lagrangian Coherent Structures for Design Analysis of Revolving Doors. *Visualization and Computer Graphics, IEEE Transactions on*, 18(12):2159–2168, 2012.

SH13. Shawn C. Shadden and Sahar Hendabadi. Potential fluid mechanic pathways of platelet activation. *Biomechanics and Modeling in Mechanobiology*, 12(3):467–474, 2013.

Sha11. Shawn C. Shadden. Lagrangian Coherent Structures. *Transport and Mixing in Laminar Flows: From Microfluidics to Oceanic Currents*, pages 59–89, 2011.

SLM05. Shawn C. Shadden, Francois Lekien, and Jerrold E. Marsden. Definition and properties of Lagrangian coherent structures from finite-time Lyapunov exponents in two-dimensional aperiodic flows. *Physica D: Nonlinear Phenomena*, 212(3-4):271–304, 12 2005.

SLT+11. Ga Young Suh, Andrea S. Les, Adam S. Tenforde, Shawn C. Shadden, Ryan L. Spilker, Janice J. Yeung, Christopher P. Cheng, Robert J. Herfkens, Ronald L. Dalman, and Charles A. Taylor. Hemodynamic changes quantified in abdominal aortic aneurysms with increasing exercise intensity using MR exercise imaging and image-based computational fluid dynamics. *Annals of Biomedical Engineering*, 39(8):2186–2202, 8 2011.

SMDM+11. Judy Shum, Giampaolo Martufi, Elena Di Martino, Christopher B. Washington, Joseph Grisafi, Satish C. Muluk, Ender A. Finol, Elena Di Martino, Christopher B. Washington, Joseph Grisafi, Satish C. Muluk, and Ender A. Finol. Quantitative assessment of abdominal aortic aneurysm geometry. *Annals of Biomedical Engineering*, 39(1):277–286, 1 2011.

SMPK11. Ch Stamatopoulos, D. S. Mathioulakis, Y. Papaharilaou, and A. Katsamouris. Experimental unsteady flow study in a patient-specific abdominal aortic aneurysm model. *Experiments in Fluids*, 50(6):1695–1709, 6 2011.

SSL04. Anne-Virginie Salsac, Steven R Sparks, and Juan C Lasheras. Hemodynamic changes occurring during the progressive enlargement of abdominal aortic aneurysms. *Annals of vascular surgery*, 18(1):14–21, 1 2004.

ST08. Shawn C. Shadden and Charles A. Taylor. Characterization of coherent structures in the cardiovascular system. *Annals of Biomedical Engineering*, 36(7):1152–1162, 7 2008.

Tar03. John M. Tarbell. Mass Transport in Arteries and the Localization of Atherosclerosis. *Annual Review of Biomedical Engineering*, 5(1):79–118, 8 2003.

Tau95. G. Taubin. Curve and surface smoothing without shrinkage, 1995.

TCRH11. J. Tong, T. Cohnert, P. Regitnig, and G. A. Holzapfel. Effects of age on the elastic properties of the intraluminal thrombus and the thrombus-covered wall in abdominal aortic aneurysms: Biaxial extension behaviour and material modelling. *European Journal of Vascular and Endovascular Surgery*, 42(2):207–219, 8 2011.

TGP+15. F. Tanios, M. W. Gee, J. Pelisek, S. Kehl, J. Biehler, V. Grabher-Meier, W. A. Wall, H. H. Eckstein, and C. Reeps. Interaction of Biomechanics with Extracellular Matrix Components in Abdominal Aortic Aneurysm Wall. *European Journal of Vascular and Endovascular Surgery*, 50(2):167–174, 2015.

TH15. Jianhua Tong and Gerhard A. Holzapfel. Structure, Mechanics, and Histology of Intraluminal Thrombi in Abdominal Aortic Aneurysms. *Annals of Biomedical Engineering*, 43(7):1488–1501, 5 2015.

TKTP+14. An Tang, Claude Kauffmann, Sophie Tremblay-Paquet, Stéphane Elkouri, Oren Steinmetz, Florence Morin-Roy, Laurie Cloutier-Gill, and Gilles Soulez. Morphologic evaluation of ruptured and symptomatic abdominal aortic aneurysm by three-dimensional modeling. *Journal of Vascular Surgery*, 59(4):894–902, 4 2014.

TOK+09. Ryo Torii, Marie Oshima, Toshio Kobayashi, Kiyoshi Takagi, and Tayfun E. Tezduyar. Fluid-structure interaction modeling of blood flow and cerebral aneurysm: Significance of artery and aneurysm shapes. *Computer Methods in Applied Mechanics and Engineering*, 198(45-46):3613–3621, 9 2009.

VCFJT10. I. E. Vignon-Clementel, C. A. Figueroa, K. E. Jansen, and C. A. Taylor. Outflow boundary conditions for 3D simulations of non-periodic blood flow and pressure fields in deformable arteries. *Computer Methods in Biomechanics and Biomedical Engineering*, 13(5):625–640, 10 2010.

vtVBM+08. Marcel van 't Veer, Jaap Buth, Maarten Merkx, Pim Tonino, Harrie van den Bosch, Nico Pijls, and Frans van de Vosse. Biomechanical properties of abdominal aortic aneurysms assessed by simultaneously measured pressure and volume changes in humans. *Journal of Vascular Surgery*, 48(6):1401–1407, 2008.

WBME00. J. J. Wever, J. D. Blankensteijn, W. P.Th M. Mali, and B. C. Eikelboom. Maximal aneurysm diameter follow-up is inadequate after endovascular abdominal aortic aneurysm repair. In *European Journal of Vascular and Endovascular Surgery*, volume 20, pages 177–182. 2000.

WMWV02. David H.J. Wang, Michel S. Makaroun, Marshall W. Webster, and David A. Vorp. Effect of intraluminal thrombus on wall stress in patient-specific models of abdominal aortic aneurysm. *Journal of Vascular Surgery*, 36(3):598–604, 10 2002.

WOBSS85. L. J. Wurzinger, R. Opitz, P. Blasberg, and H. Schmid-Schonbein. Platelet and coagulation parameters following millisecond exposure to laminar shear stress. *Thrombosis and Haemostasis*, 54(2):381–386, 1985.

WS15. Jiacheng Wu and Shawn C. Shadden. Coupled Simulation of Hemodynamics and Vascular Growth and Remodeling in a Subject-Specific Geometry. *Annals of biomedical engineering*, 43(7):1543–1554, 3 2015.

WSS+10. Ireneusz Wiernicki, Ewa Stachowska, Krzysztof Safranow, Miloslaw Cnotliwy, Marta Rybicka, Mariusz Kaczmarczyk, and Piotr Gutowski. Enhanced matrix-degrading proteolytic activity within the thin thrombus-covered wall of human abdominal aortic aneurysms. *Atherosclerosis*, 212(1):161–165, 9 2010.

WVDA+13. J. S. Wilson, L. Virag, P. Di Achille, I. Karšaj, and J. D. Humphrey.

Biochemomechanics of Intraluminal Thrombus in Abdominal Aortic Aneurysms. *Journal of Biomechanical Engineering*, 135(2):021011, 2 2013.

XHF13. Nan Xiao, Jay D. Humphrey, and C. Alberto Figueroa. Multi-scale computational model of three-dimensional hemodynamics within a deformable full-body arterial network. *Journal of Computational Physics*, 244:22–40, 2013.

YPH+06. Paul A. Yushkevich, Joseph Piven, Heather Cody Hazlett, Rachel Gimpel Smith, Sean Ho, James C. Gee, and Guido Gerig. User-guided 3D active contour segmentation of anatomical structures: Significantly improved efficiency and reliability. *NeuroImage*, 31(3):1116–1128, 2006.

ZGL+16. Byron A. Zambrano, Hamidreza Gharahi, ChaeYoung Young Lim, Farhad A. Jaberi, Jongeun Choi, Whal Lee, and Seungik Baek. Association of Intraluminal Thrombus, Hemodynamic Forces, and Abdominal Aortic Aneurysm Expansion Using Longitudinal CT Images. *Annals of Biomedical Engineering*, 44(5):1502–1514, 5 2016.

CHAPTER 4

Vorticity in AAA: from an Eulerian to a Lagrangian point of view

Keywords:

aortic aneurysms; hemodynamics; transport topology; CFD; AAA growth; interventional radiology; intraluminal thrombus; FTLE

4.1 Introduction

BLOOD flow characteristics play a significant role in AAA risk prediction and relations between several flow features and AAA growth were explored in chapter 2. However, the interplay between flow alteration, intra-luminal thrombus (ILT) growth and AAA growth has not been fully elucidated. In light of the current literature, the progression of the disease is believed to follow the pattern shown in Figure 4.1.

To summarize, aging could be the initial insult, as buckling of the artery wall appears with loss of elastin and resulting lengthening [LH12]. The resulting flow alteration may induce WSS and transport transformation, leading to the presence of activated platelets that tend to adhere to ILT and the inflammed wall. ILT prevents correct oxygenation of the arterial wall and thereby further deteriorates the wall since hypoxia is a known

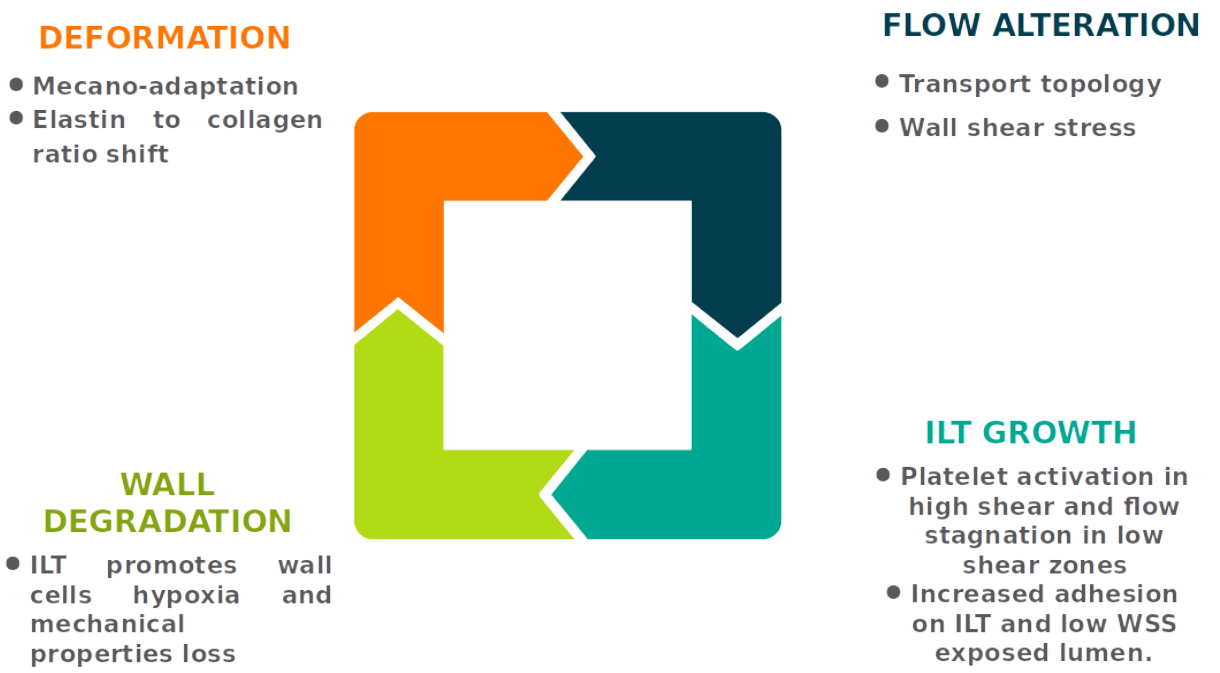

Figure 4.1 – Vicious circle of AAA growth with simplified mechanisms.

factor of mechanical degradation [WVDA+13]. Because of the pressure load, elastin loss (degradation and slow production) precedes further wall deformation. From a transport point of view, particles travelling along LCS may be subject to high shearing, causing possible platelet activation. If activated, i.e., subjected to a certain hemodynamic shear stress level for long enough [RZM79, WOBSS85], platelets entering stagnation zones are likely to adhere to the wall and create a substrate favourable to thrombus deposition. Low shear stress may also be a condition necessary for platelet adhesion [BGA+10] which happens in stagnation zones. Portions of the wall exposed to low shear can be visualized as time average wall shear stress and linked to thrombus deposition [ZGL+16]. However, this only accounts for part of the adhesion mechanism. Looking at the aorta location exposed to stagnation zones could be an additional predictor of ILT deposition.

The transition from visualization to quantification was performed by segmenting the dynamically isolated zones, i.e. the sinks in the FTLE field (see chapter 3 and [JSG+18]). However, if this approach worked reasonably well in the presented case, once the authors

tried to extend the concept to other patients, it failed on most of them. The example used was very tortuous with very distinct bulges and clearly distinguishable dynamically isolated zone (DIZ) (see Figure 4.2).

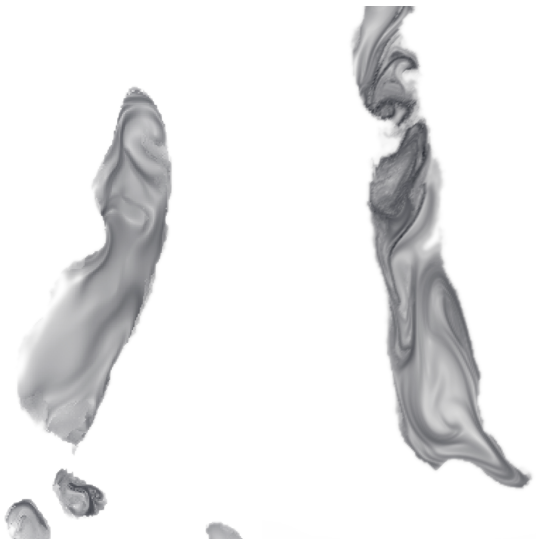

Figure 4.2 – Sagital cut of the FTLE field in two AAA without easily distinguishable DIZ.

In chapter 3, FTLE were computed to recover the hyperbolic LCS of the system. It was applied to a AAA, where the extracted material surfaces allowed the visualization of the underlying structure of the flow and, more importantly, the quantification of the volume of "dead" zones in the lumen. Nonetheless, LCS defined as FTLE ridges suffer from further conceptual and mathematical problems: second-derivative of FTLE ridges (definition used in chapter 3) are necessarily continuous straight lines and may not exist in physical problems [SPFT12]; the flux formula from [SLM05, LC07], showing the null flux through the FTLE ridge, has been proven wrong in [Hal15, Hal11]. Furthermore, while FTLE ridges mark hyperbolic LCS positions they also include high shear surface [Hal02], elliptic and parabolic LCS [Hal15]. The observed field is a mixture of both and could lead to erroneous interpretation. As also considered in the study, the use of sliding time windows to enhance flow separation visualization [FSP12] is affected by the material flux formula, and ridges computed over sliding time windows with a varying integration time are generally not Lagrangian [Hal11].

If a general transport analysis in unsteady flow remains a complex subject, vortex presence in AAAs is an indicator of flow alteration but is also believed to contribute to AAA growth [BAH18, LTA+13, EBE+99].

In particular, platelets are convected toward the distal aneurysm region inside vortex cores and are activated via a combination of high residence times and relatively high shear stress at the vortex boundary. After vortex break-up, platelets are free to adhere to the thrombogenic wall surface. Vortical structures (VS) also convect thrombin, a potent procoagulant enzyme, captured in their core, through the aneurysmatic lumen, and force its accumulation in the distal portion of the AAA.

Finally, vortex visualization, and hence extraction, belong to the family of feature-based methods of flow visualization [PVH+03]: one goal is to partition the flow in domains of coherent behaviour. Transient topology visualization is more specifically addressed in [PPF+11]. While observing vortices developing during the cardiac pulse certainly helps understanding the flow inside AAA, few articles address the question of systematic quantification. Recently, [BAH18] extracted vortex from λ_2 iso-surfaces and computed three metrics: 1) depth of the main VS at the moment before break-up, 2) cross-sectional area of the jet at break-up and 3) the difference between jet and centerline direction at the break-up location. This information may help linking AAA shape to vortex shape as it accounts for both its size and shape. This approach gives insights on the shape and direction of the jet relative to the lumen, while the time-dependent aspect lies in the chosen evaluation moment rather than a time-integral metric. The purpose of this chapter is thus to explore the development of VS in AAAs with various shapes. [HHFH16] defined the Lagrangian-averaged vorticity deviation (LAVD), integration of the deviation of the vorticity from its spatial mean along the flow trajectory. Also, VS extracted from the LAVD are objective.

4.2 Materials and Methods

4.2.1 Patient selection

The 5 AAA from the study in chapter 2 included in this work are presented in Figure 4.3. The selected AAA lumen represent a stratified sampling of the population with respect to the normalized sphere index (NSI) [1], lumen centerline tortuosity, curvature and D_{max} of the available cases. The selection was performed from the dataset of lumen and features build in chapter 2. Visual check ensured main AAA shapes are represented.

4.2.2 Flow simulation

4.2.2.1 Modeling

Similarly to the process described in chapter 3, the continuity equation (Equation 4.1) and the Navier-Stokes momentum equation (Equation 4.2) are solved.

$$\nabla \cdot U = 0 \tag{4.1}$$

$$\frac{\partial \rho \mathbf{U}}{\partial t} + \rho(\mathbf{U} \cdot \nabla)\mathbf{U} - \nabla \cdot \mu \nabla \mathbf{U} = -\nabla p \tag{4.2}$$

with :

$\mathbf{U}$ = velocity

p = pressure

t = time

ρ = density

μ = dynamic viscosity

This system contains 4 equations (Equation 4.1 and the momentum equation Equa-

1. See Table II and Raghavan et al. [RKCdT+06]

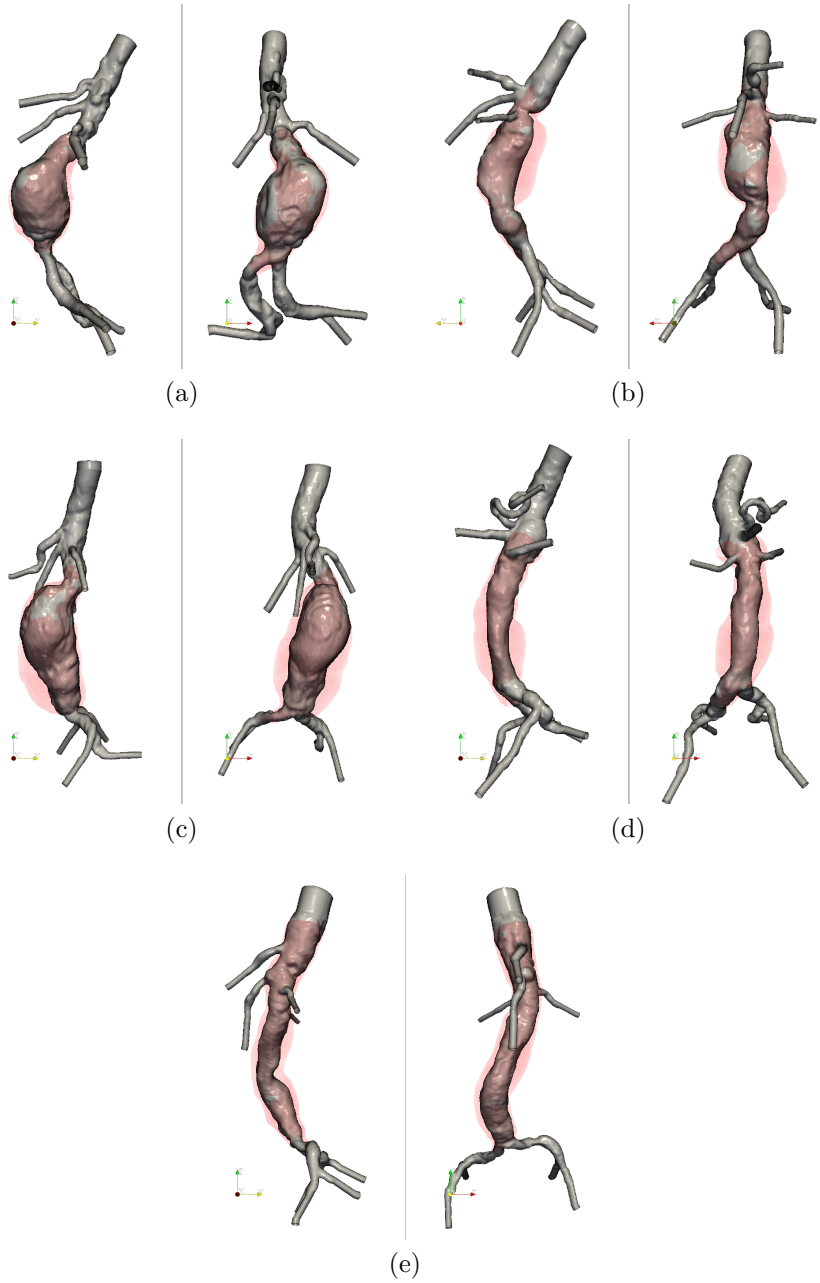

Figure 4.3 – Lumen (grey) and ILT (red) of all 5 AAA included in this study in sagittal and frontal views. Case *a* displays a balloon shape (NSI close to 1) in opposition to *e* strongly tubular (NSI close to 0). *d* : the shape is highly tortuous with a double curvature in the frontal plane. *b* and *c* neck have a strong curvature. *a* and *d* present little to no ILT deposit in contrast to *b*, *c* and *e*.

tion 4.2 on 3 directions) for 4 unknowns, p, U_x, U_y and U_z. The solution is described in subsubsection 4.2.2.2.

The flow is considered laminar in the aorta for two reasons: the velocity burst is not long enough for turbulence to develop, and the helicity of the flow has a dissipative and stabilizing role (see chapter 3). A non-newtonian model is used for the blood with the Quemada equation (Equation 4.3) describing the relationship between viscosity and shear rate [BKC00].

$$\eta = \left(\sqrt{(\eta_\infty)} + \frac{\sqrt{\tau_0}}{\sqrt{\lambda} + \sqrt{\dot{\gamma}}} \right)^2 \tag{4.3}$$

with :

η = apparent viscosity

$\dot{\gamma}$ = shear rate, such as :

$$\dot{\gamma} = \tfrac{1}{2} \left((\nabla \mathbf{U}) + (\nabla \mathbf{U})^\top \right)$$

η_∞ = viscosity when $\dot{\gamma} \to \infty$, $(0.002654\,\mathrm{Pa\,s^{-1}}$ [BKC00])

τ_0 = shear stress when $\dot{\gamma} \to 0$, $(0.004360\,\mathrm{Pa\,s^{-1}}$ [BKC00])

λ = characteristic time, $(0.02181\,\mathrm{s^{-1}}$ [BKC00])

$\mathbf{U}$ = fluid velocity

As proved by [BHCG11], a non-newtonian modelling of the blood viscosity is critical for a proper capture of VSs.

Boundary conditions are described in chapter 3. To recap:

Inlet A time-varying flow rate was imposed at the inlet [MGG+70], located approximately 5 cm upstream of the upper renal artery. Though actual inlet flow patterns may present either single or double swirl structures [MPR+11], no generic spatial velocity profile can currently describe flow entering AAA. Considering the lack of available information, a time-dependent flow rate from [MGG+70] was mapped on a Womersley profile. As in chapter 2 flow Reynolds and Womersley remain wihtin physiological values : peak

Reynolds are around 2000 at the proximal inlet and peak Womersley numbers at same location varied from 10 to 15 [MMKB94].

Wall In AAA, wall geometry is characterized by the aorta and thrombus deposits. Aortic wall mechanical properties vary with vessel size and location as well as patient age. Wall rheology becomes highly patient-specific and heterogeneous with the progression of atherosclerotic disease [RKCdT+06]. The thrombus is also a complex, layer-structured and heterogeneous material [WVDA+13]. In practice, it is difficult to characterize 3-D wall rheology by non-invasive techniques for fluid-structure simulations. Wall stiffness increases with disease progression and patient age [TCRH11]. In addition, thrombus alters wall stress distribution and augments apparent stiffness [WMWV02]. The present study considered the wall and thrombus as rigid materials, and applied no-slip conditions. Similarly to previous chapters, no surface roughness.

Outlets A 3-element Windkessel model was applied on each outlet [MBRvdV11, VCFJT10]). Model parameters were chosen according to [XHF13] study.

4.2.2.2 Numerical implementation

p does not appear in Equation 4.1 leading to the pressure-momentum coupling problem. Here, the PIMPLE algorithm is adopted for this purpose. It is the combination of the well-known PISO (Pressure-Implicit-of-Split-Operations) and SIMPLE (Semi-Implicit-Method-Of-Pressure-Linked-Equations) algorithms. For PISO, the Courant number (Equation 4.4, or *how many cells does a fluid particle travel through in one time step ?*) has to remain below ≈ 1 for stability.

$$\mathrm{Co} = \frac{\mathbf{U}\Delta t}{\Delta x} \tag{4.4}$$

with :

$\mathbf{Co}$ = Courant number

$\mathbf{U}$ = velocity

Δt = time step

Δx = distance between the cells

With PIMPLE, the Courant number can be increased. The numerical schemes used to solve the equations are: 2^{nd} order Crank-Nicholson implicit in time and Gauss linear for spatial integration, also second order implicit. Simulation were initialized with first order schemes for improved stability at start-up.

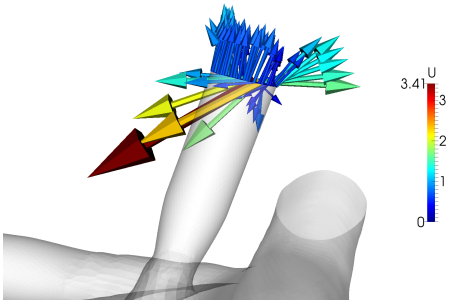

Figure 4.4 – Example of divergence at an outlet leading to the preliminary halt of the simulation.

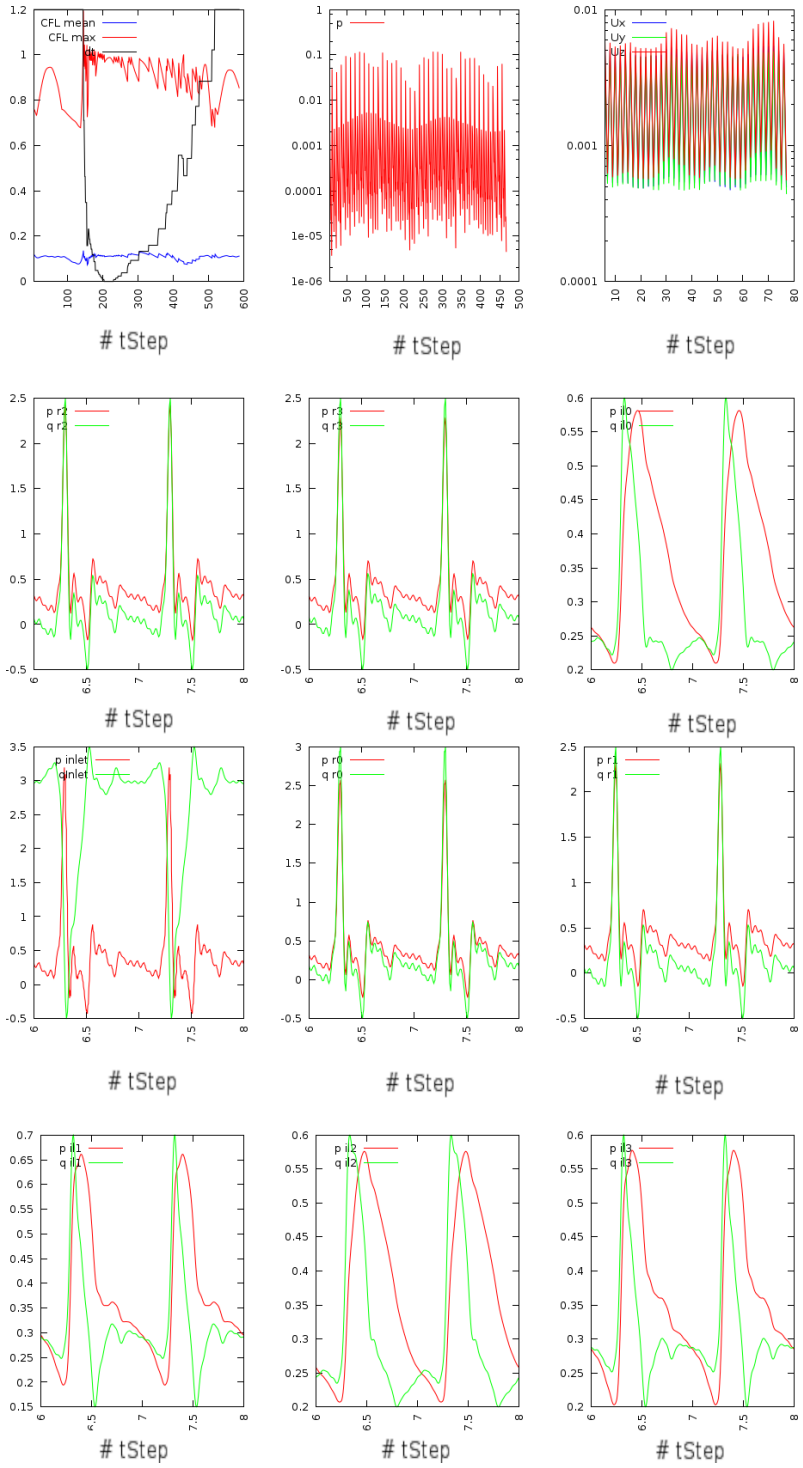

Figure 4.5 – Example of a simulation live plotting with the CFL and Δt auto adaptation, pressure and velocity residuals and average values at all inlet and outlets.

Blood flow can present complex recirculation patterns in diseased aorta that can stretch

down to outlet planes. Reverse flow is also a natural phenomenon occurring in large arteries during diastole [EMBH+11, KYM+93], generally creating instabilities and crash, see Figure 4.4. Artificial extension of outlets, leading to unrealistic geometries and increased number of mesh elements, is common practice in arterial flow simulations addressing these issues. Neumann boundary conditions on velocities were rather adopted with gradient to control blood backflow in the domain derived from the solution proposed by [EMBH+11]. In physical terms, a term is added at outlets that acts as an outward traction, opposite the direction of backflow, which pushes the flow in the direction of the outward normal. In this sense, this term provides the "missing" convective flow information from outside of the computational domain during flow reversal. The simulation stops when the flow variables averaged on the outlets minus their values evaluated at the previous cardiac period get below a threshold. The temporal convergence is illustrated in Figure 4.6. The ξ convergence criteria can be written as:

$$\xi = \sum_{i=0}^{outlets} |\langle x \rangle_t^i - \langle x \rangle_{t-T}^i|, \quad x = \mathrm{p,U} \tag{4.5}$$

with :

ξ = convergence criteria

T = cardiac period

t = time

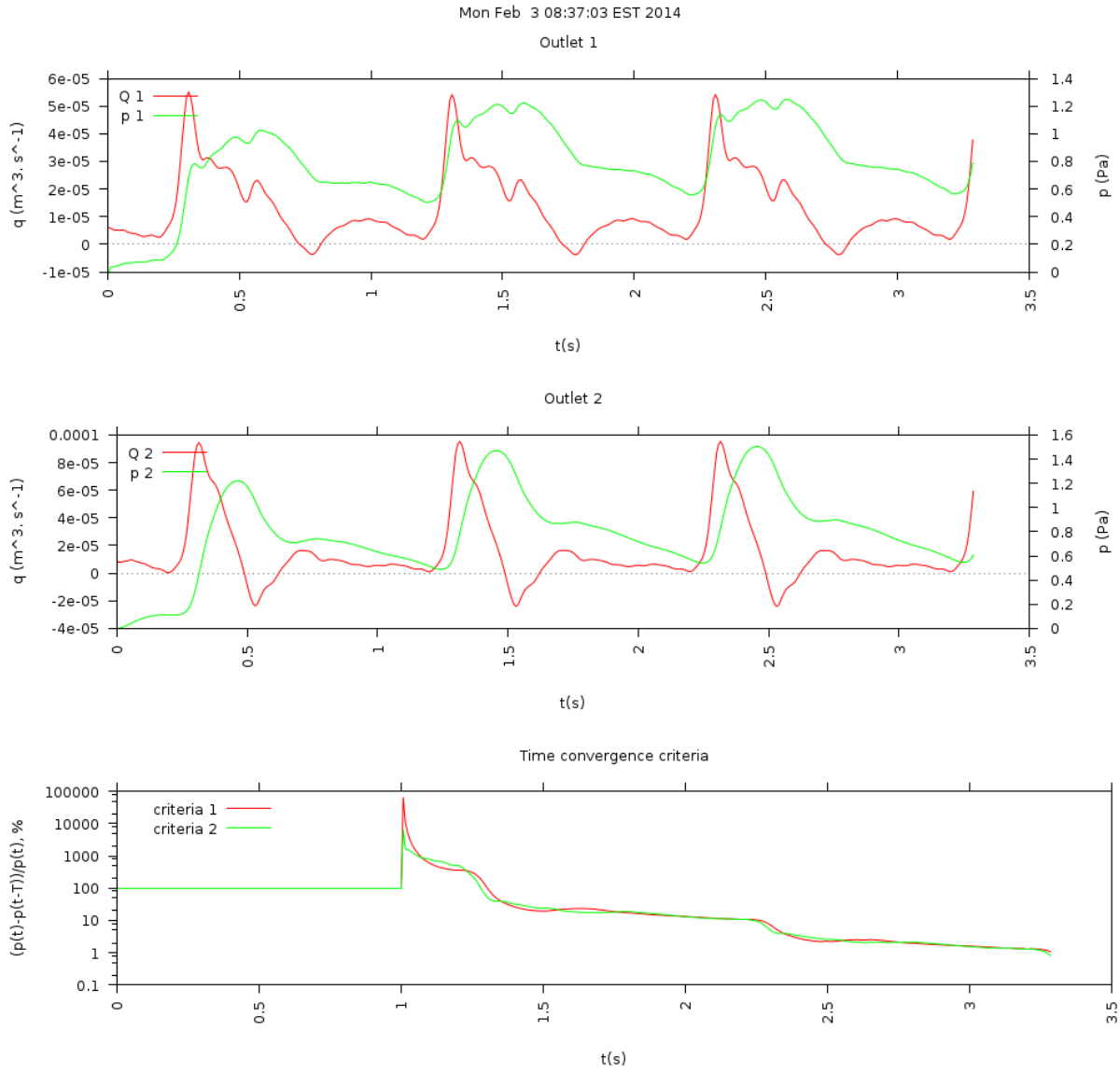

Figure 4.6 – Example of the metric used to ensure the simulation is temporally converged. The pressure is averaged at each outlet and compared to the value at the previous heartbeat. Top and middle plots: mean value of p and U at 2 outlets plotted during two cardiac periods. Bottom: plot of ξ from Equation 4.5.

4.2.3 Vortical structures

4.2.3.1 Vorticity

The vorticity term was coined in 1916 by Lamb but the concept had been known since at least 1851 by Stokes, under the name *angular velocities*, or Helmoltz in 1858 with *Rotationsgeschwindigkeiten* [Tru18]. It is a vector describing the local spinning around a point: it can either be rotation or shearing induced vorticity (flow going in on direction with different velocities). The 3 element pseudo-vector vorticity $\boldsymbol{\omega}$ of the velocity field $\mathbf{U}$ can be written :

$$\boldsymbol{\omega} = \nabla \times \mathbf{U} \tag{4.6}$$

The vorticity is computed with the central differences method on an unstructured mesh.

4.2.3.2 Rotationally Coherent Lagrangian Vortices and Rotationally Coherent Eulerian Vortices

Following the work of [HHFH16, Hal16], the LAVD field is defined as :

$$\mathrm{LAVD}^{t}_{t_0}(x_0) := \int_{t_0}^{t} \left|\boldsymbol{\omega}\left(x\left(s;x_0\right),s\right) - \overline{\boldsymbol{\omega}}(s)\right| \mathrm{d}s \tag{4.7}$$

with

$$\overline{\boldsymbol{\omega}}(t) = \frac{\int_{\Omega(t)} \boldsymbol{\omega}(x,t) dV}{\mathrm{vol}(\Omega(t))} \tag{4.8}$$

with $vol(\cdot)$ the volume, ds a small element of the fluid trajectory and $\Omega(t)$ normalization domain in $\mathbb{R}^3$. LAVD is proven objective, i.e. invariant under any smooth rotation and translation of the reference frame. In a similar fashion as dynamically isolated zones were extracted from the FTLE field, vortices will be extracted from LAVD. Those vortices, the Rotationally Coherent Lagrangian Vortices (LV) are defined as a tubular set in $3D$, or, to cite [HHFH16], a *convex, cylindrical, cup-shaped or toroidal set.*

A Taylor expansion of LAVD over a short interval δt, or $LAVD_{t_0}^{t+\delta t}$, gives :

$$\mathrm{LAVD}_{t_0}^{t+s}(x_0) = \mathbf{LAVD}_{t_0}^{t}(x_0) + \mathbf{IVD}\left(x\left(t;x_0\right),t\right)\cdot s + O\left(s^2\right) \tag{4.9}$$

by defining,

$$\mathbf{IVD}(x,t) := |\boldsymbol{\omega}(x,t) - \overline{\boldsymbol{\omega}}(t)| \tag{4.10}$$

the Instantaneous Vorticity Deviation. Also objective, IVC also permits the extraction of vortices.

The vortices extraction for LAVD and IVD is similar:

- computation of the LAVD (IVD) field from the velocity flow-map
- detection of the vortex cores $\mathscr{C}(t)$, local maxima of the LAVD (IVD)
- extraction of the vortex boundaries $\mathscr{B}(t)$ such as :
  - · a vortex $\mathscr{V}(t)$ is a set of nested tubular surfaces.
  - · $\mathscr{B}(t)$ is the outermost level surface of $\mathscr{V}(t)$ and $\mathscr{C}(t)$ the innermost member.
  - · LAVD (IVD) values are non-increasing from $\mathscr{C}(t)$ to $\mathscr{B}(t)$.

To compute the LAVD field, seeds are placed in the AAA (see Figure 4.7) and advected with a RK45 algorithm. The IVD is computed at each step and integrated along the trajectories for each seed point.

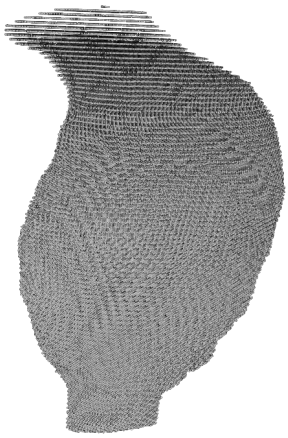

Figure 4.7 – Local view of the seeds used to initialize the advection process in the anevrismal area.

4.3 Results

4.3.1 Vorticity

Figure 4.9 to Figure 4.14 present composite rendering of colour coded vorticity plots on axial planes, vorticity cores and vorticity iso-value surfaces with the corresponding velocity glyphs. The vorticity field shows complex structures that are difficult to read as they are varying greatly with time. Iso-values, or contour plots were chosen for each patient with the aim of extracting the main VS of the flow : too low values would extract noise and irrelevant small structures, and too high values would only extract local non representative of the flow.

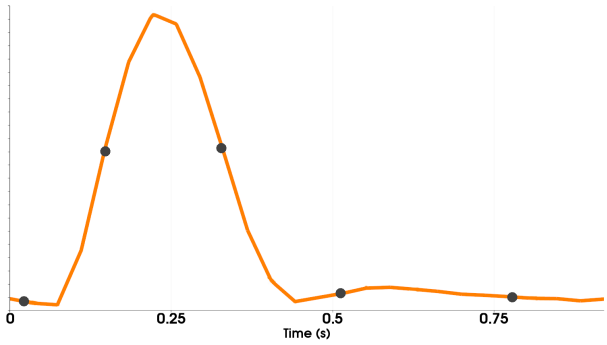

Figure 4.8 – Localization of time snapshots in a cardiac period.

Patient **A** AAA (see Figure 4.9) is saccular with an important direction change at the proximal neck. On the axial slices from all time steps the evolution of two contra-rotational swirls or a double gyre (described in [SG88]) is visible. It is less clear during the diastolic phase (see Figure 4.8 to see the location of the snapshots in the cardiac pulse), times a and e, but highly distinguishable during the high velocity phase b and c, and beginning of diastole e. Those two swirls are likely the traces of a vortex travelling in AAA coming out the jet. VSs moving in high shear regions get stretched giving them shapes similar to the hairpin vortex present in turbulent boundary layers. In patient **B** (see Figure 4.10) the descending vortex ring is well captured by the vorticity contour. Initiated at the proximal neck at time b, it develops during the systolic and diastolic phase and breaks down during the very end diastolic and early systolic phase. Figure 4.11 shows a local view at the proximal neck of the same patient. From time a to b the detachment of a VS is visible at the lumen recess. This VS will travel down the AAA, growing (time c) and then breaking into small structures. A time a the remains of the previous cardiac period is visible mid-AAA. The surface is colour-coded with the blood velocity, highlighting the sharp acceleration at the neck. Patient **C** (see Figure 4.12), by contrast, is highly fusiform, leaving the flow relatively undisturbed. Vortex lines and slices show some disturbance post renal arteries but no persistent VSs is visible, only the near-wall high shear region. Similarly to patient **A**, patient **D** (see Figure 4.13) presents a tortuous proximal neck.

From the slices and contour, the flow jet boundary entering the AAA sac is visible at time *c* and *d*. At those two times steps a vortex ring is present immediately past the neck enlargement. A vortex ring is also visible at time *e*, sheared between the extension of the jet (almost dead at that time) and the AAA slow central portion. Slices plots show this highly asymmetrical vorticity distribution. Besides the complex structure from the neck to the bulging side, a vortex core is present at all time steps centered in the AAA and aligned with it, illustrating a global rotational movement in the AAA. Finally, patient **E** (Figure 4.14), displays both a tortuous and fusiform shape. Unlike patient **C**, no main VS stems from the renal arteries bifurcation but some VS arises from the lumen kinking during the post-systolic deceleration with a highly distinguishable horseshoe vortex, sheared by the higher blood velocity on the outer side of the curvature. The particular case at time *c* is similar to patient **C**, where higher values of vorticity form a tubular shape inside the lumen at the high shear location.

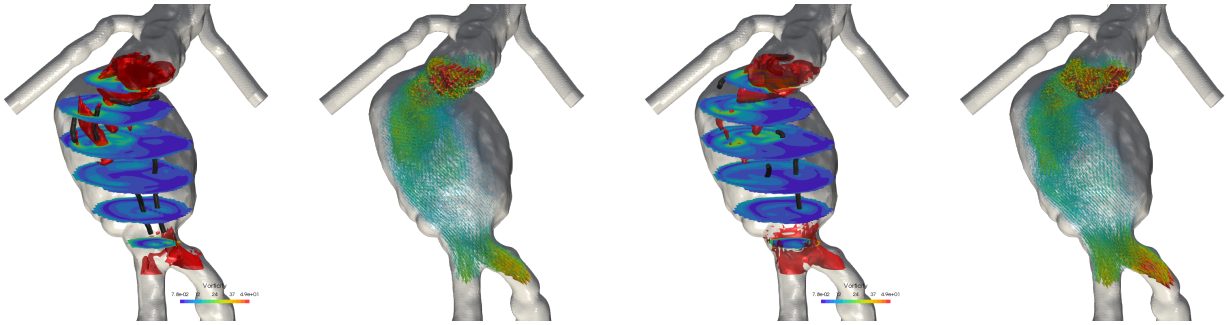

(a) $t = 0$ (b) $t = T/5$

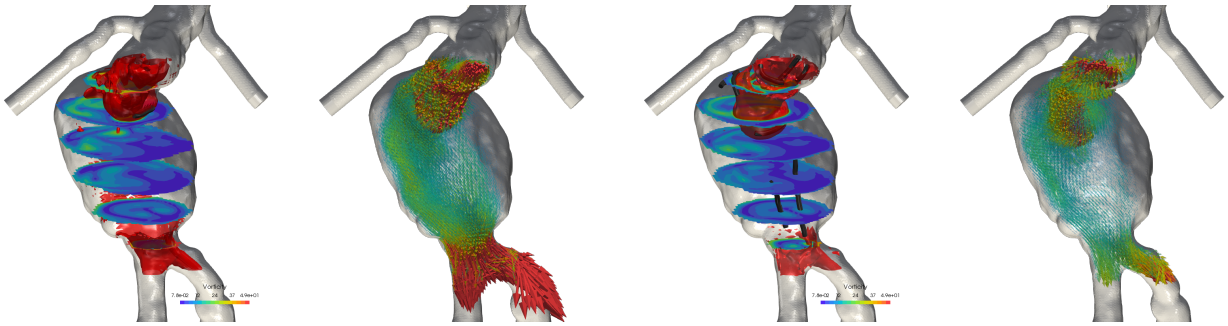

(c) $t = 2T/5$ (d) $t = 3T/5$

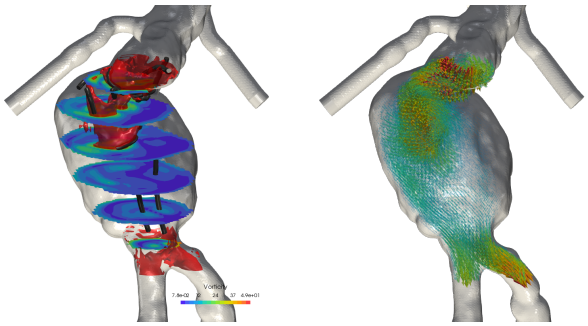

(e) $t = 4T/5$

Figure 4.9 – Patient **A**: slices along the AAA are coloured with the vorticity magnitude and a vorticity iso-level (surface build from points of constant value of vorticity in the 3D space) is shown in red. Black tubes illustrates vortex cores extracted using the [DSL90] method. For each snapshot, velocity glyphs are shown on the right.

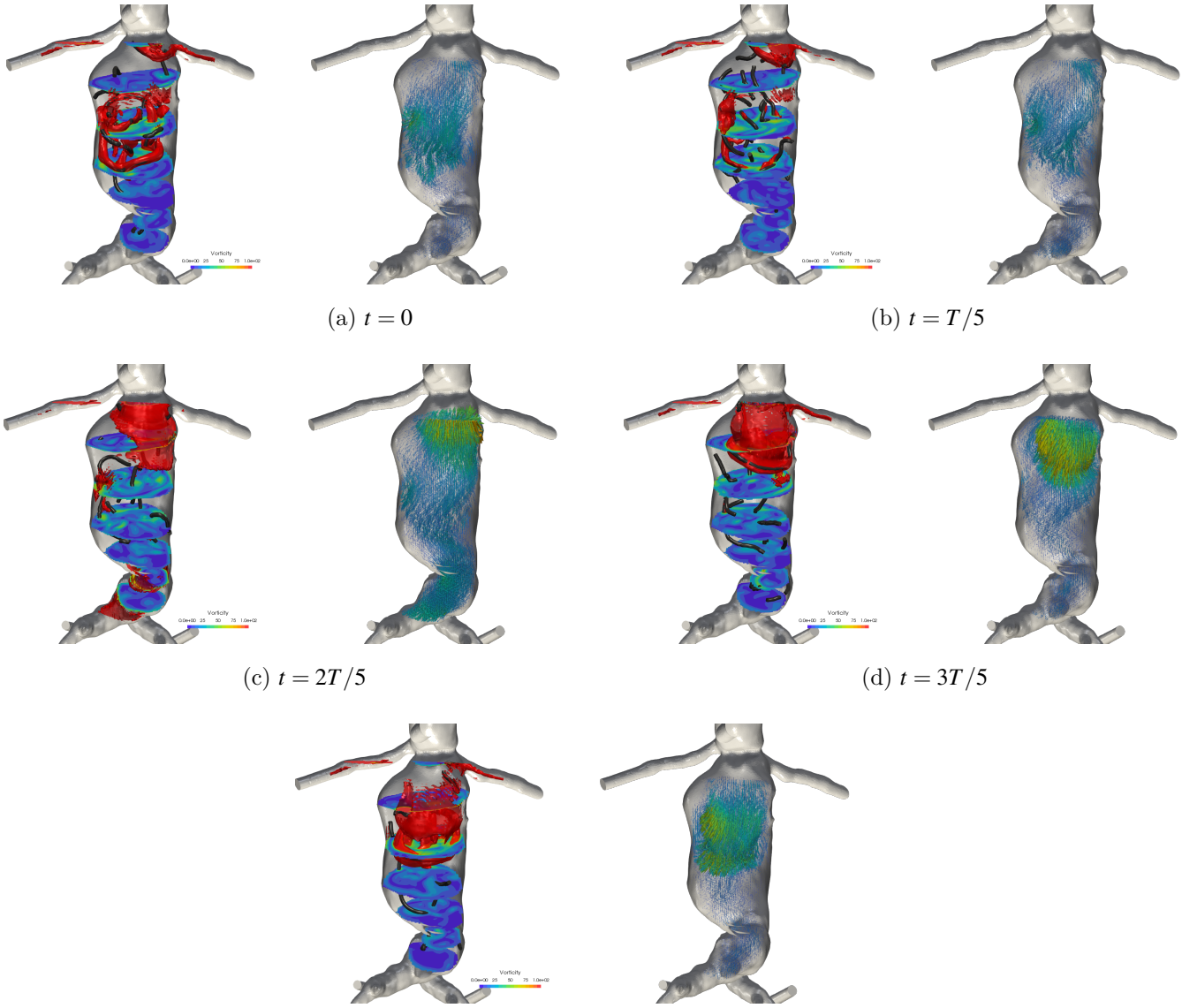

(a) $t = 0$ (b) $t = T/5$

(c) $t = 2T/5$ (d) $t = 3T/5$

(e) $t = 4T/5$

Figure 4.10 – Patient **B**: slices along the AAA are coloured with the vorticity magnitude and a vorticity iso-level is shown in red. Black tubes illustrates vortex cores extracted using the [DSL90] method. For each snapshot, velocity glyphs are shown on the right.

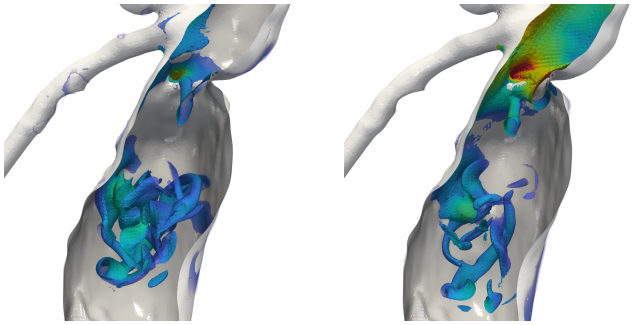

(a) $t = 0$

(b) $t = T/5$

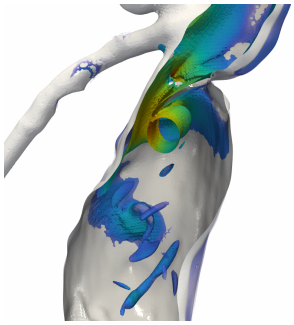

(c) $t = 2T/5$

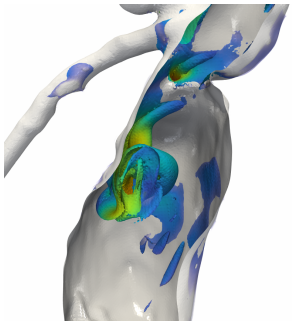

(d) $t = 3T/5$

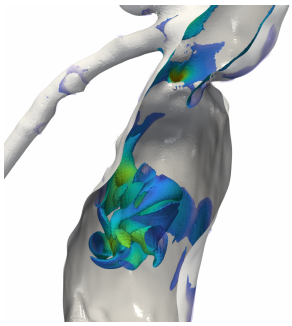

(e) $t = 4T/5$

Figure 4.11 – Local view of the development of a hairpin vortex triggered at the proximal neck of patient **B**. The surface is colour coded by the blood velocity.

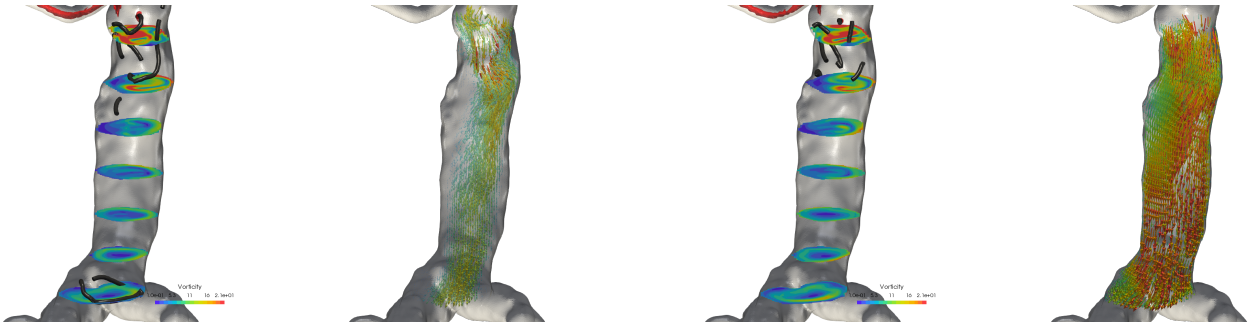

(a) $t = 0$ (b) $t = T/5$

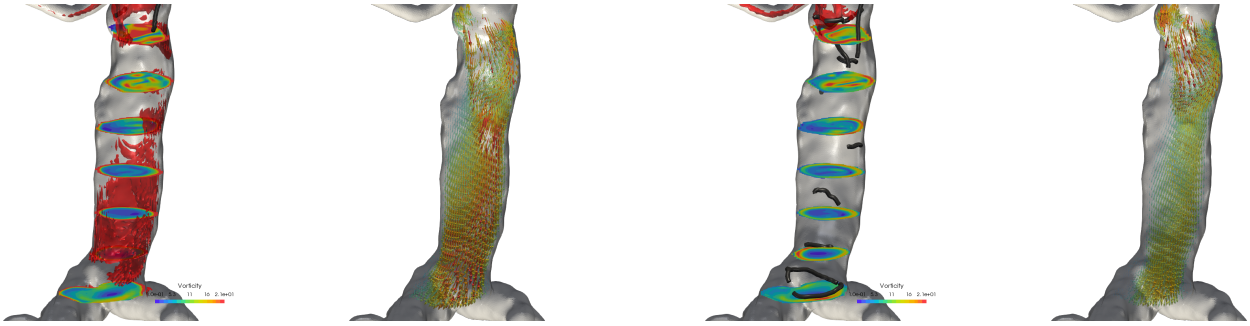

(c) $t = 2T/5$ (d) $t = 3T/5$

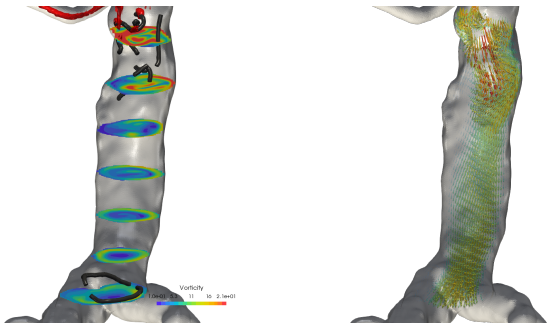

(e) $t = 4T/5$

Figure 4.12 – Patient **C**: slices along the AAA are coloured with the vorticity magnitude and a vorticity iso-level is shown in red. Black tubes illustrates vortex cores extracted using the [DSL90] method. For each snapshot, velocity glyphs are shown on the right.

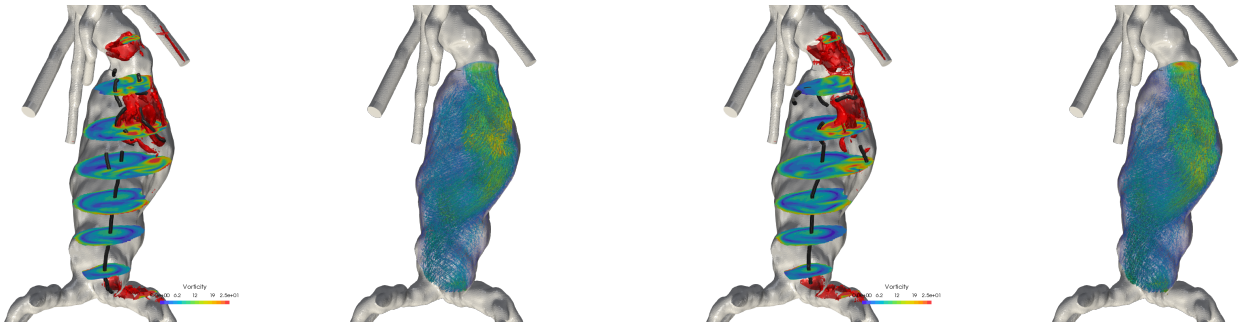

(a) $t = 0$ (b) $t = T/5$

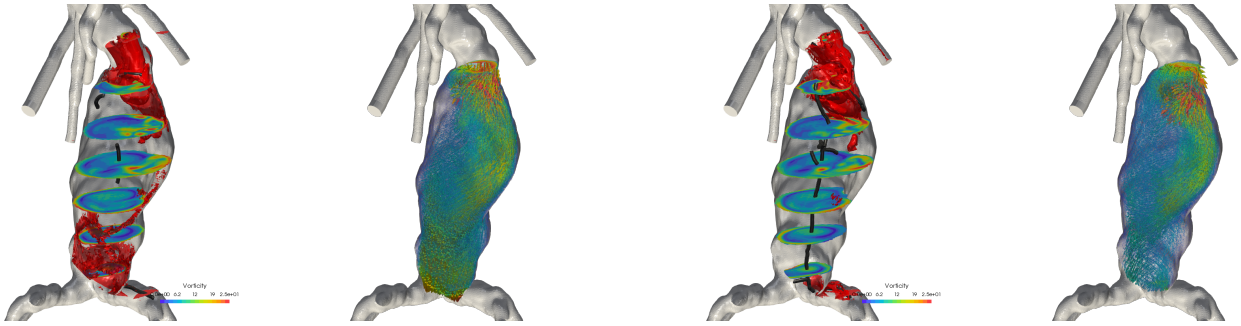

(c) $t = 2T/5$ (d) $t = 3T/5$

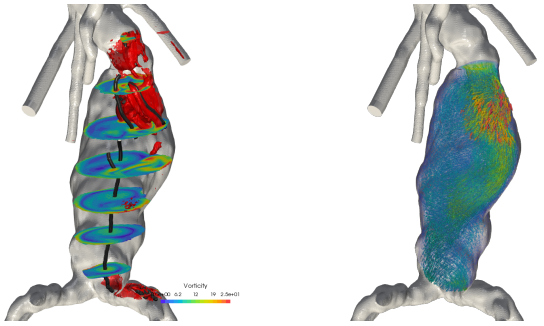

(e) $t = 4T/5$

Figure 4.13 – Patient **D**: slices along the AAA are coloured with the vorticity magnitude and a vorticity iso-level is shown in red. Black tubes illustrates vortex cores extracted using the [DSL90] method. For each snapshot, velocity glyphs are shown on the right.

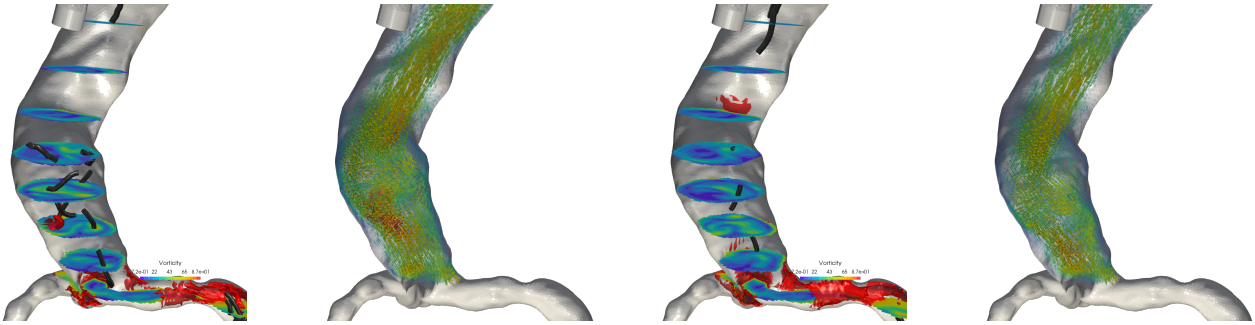

(a) $t = 0$ (b) $t = T/5$

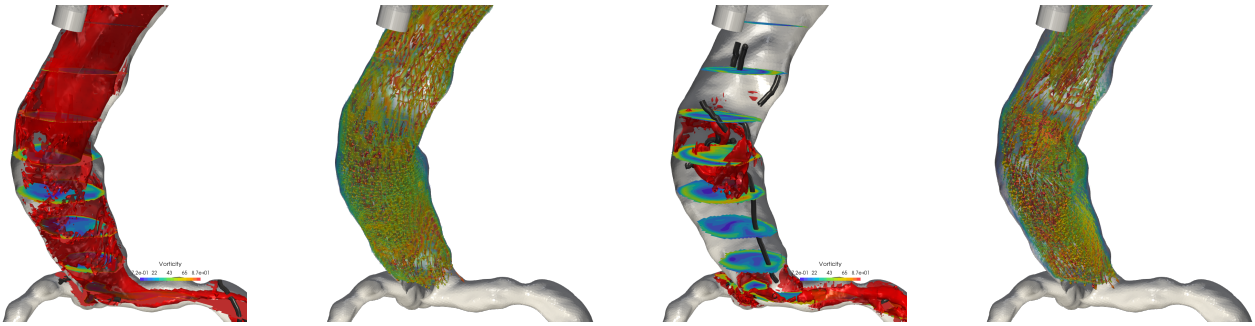

(c) $t = 2T/5$ (d) $t = 3T/5$

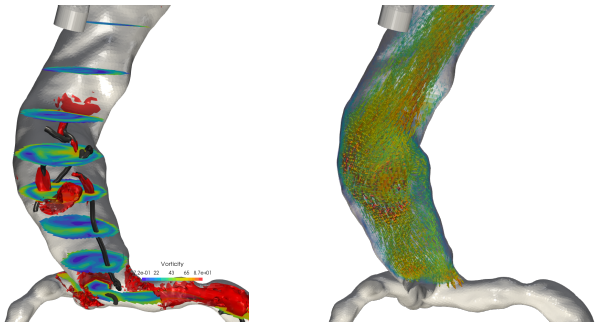

(e) $t = 4T/5$

Figure 4.14 – Patient **E**: slices along the AAA are coloured with the vorticity magnitude and a vorticity iso-level is shown in red. Black tubes illustrates vortex cores extracted using the [DSL90] method. For each snapshot, velocity glyphs are shown on the right.

4.3.2 IVD

The IVD is plotted on Figure 4.15 side-by-side with the vorticity for five time steps. The IVD field is the basis for the extraction of the instantaneous rotationally coherent

Eulerian vortices. Here no major differences are visible between IVD and vorticity. With a volume $\mathbf{\Omega}$ from Equation 4.8 equal to the entire domain, $\bar{\boldsymbol{\omega}}$ is close to zero, so the normalization was made on a local spherical subdomain, a smaller one with a diameter $\approx 2.5\text{mm}$ and a larger one with a diameter $\approx 25\text{mm}$. IVD differs more from the vorticity with a smaller normalization volume (top right images) as small features disappear (visible on Figure 4.15 *c* and *d*).

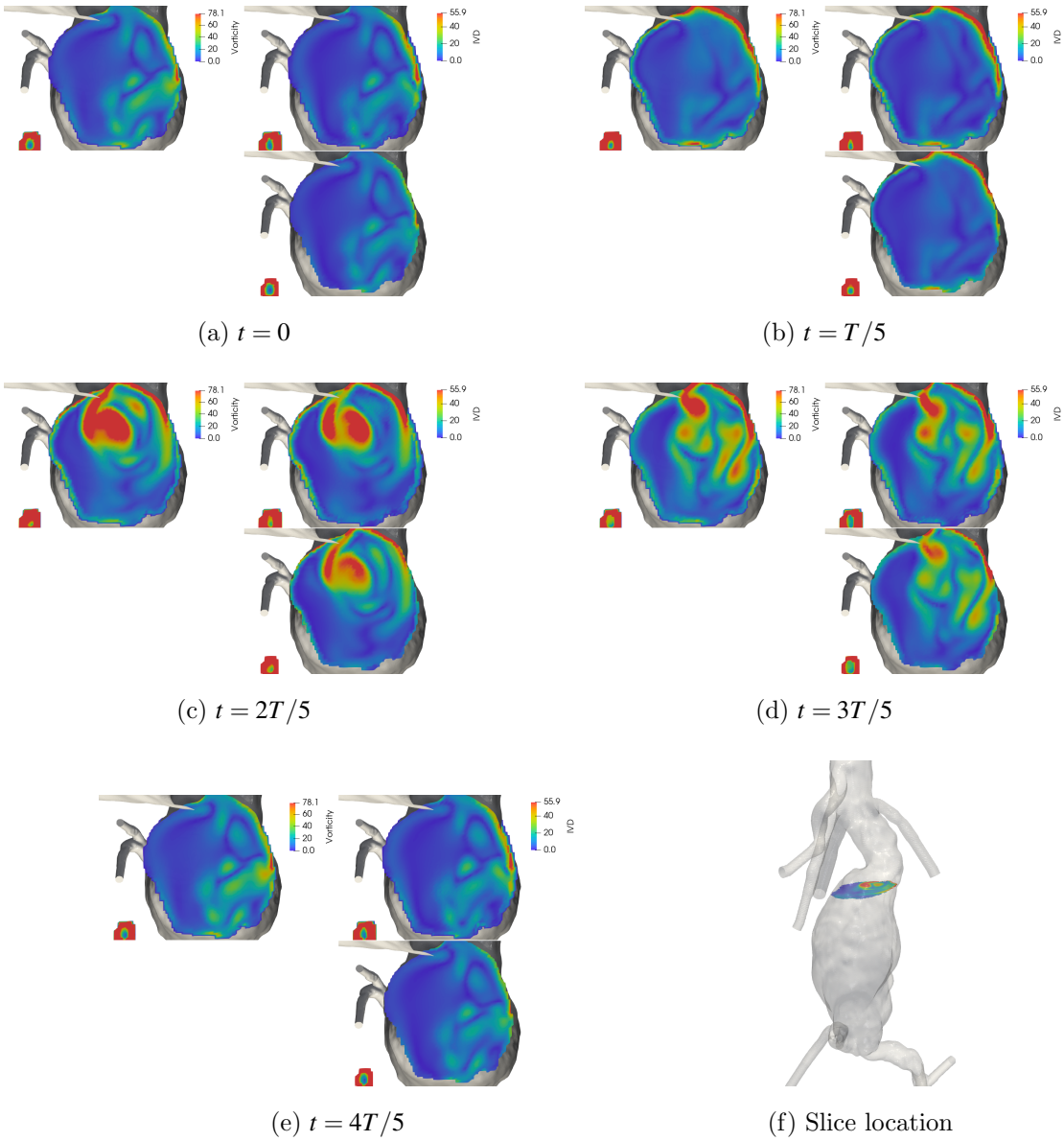

(a) $t = 0$ (b) $t = T/5$

(c) $t = 2T/5$ (d) $t = 3T/5$

(e) $t = 4T/5$ (f) Slice location

Figure 4.15 – (a) to (e) : comparison of vorticity and IVD in patient **A**, during a cardiac pulse T. For each time, left image is the vorticity and the right two images are the IVD. Top right is a case with a small Ω (see Equation 4.8) made of a sphere of diameter $\phi_{small} \approx D_{neck}/\ 10$ and bottom right is with a large normalization volume (sphere of diameter $\phi \approx D_{neck}$). The slices are in the axial plane, top view, in the AAA below the proximal neck. The location of the slice in the lumen is shown in (f).

4.3.3 LAVD

In Figure 4.16 both iso-value surfaces and volume-rendering are presented for each patient. For patients **A**, **B** and **C**, despite being noisy and discontinuous, iso-value are able to capture both generation and breaking down location of VSs. In patient **D**, surfaces highlights mainly the perturbations introduced by the renal arteries bifurcation. In patients **A**, **C** and **D**, volume rendering shows the absence of high LAVD values and structures in the AAA sack while the breaking down of VSs is visible mid-AAA for patient **B**. Near wall high LAVD values are also visible for patient **C** and **D**. Patient **E** computation did not complete.

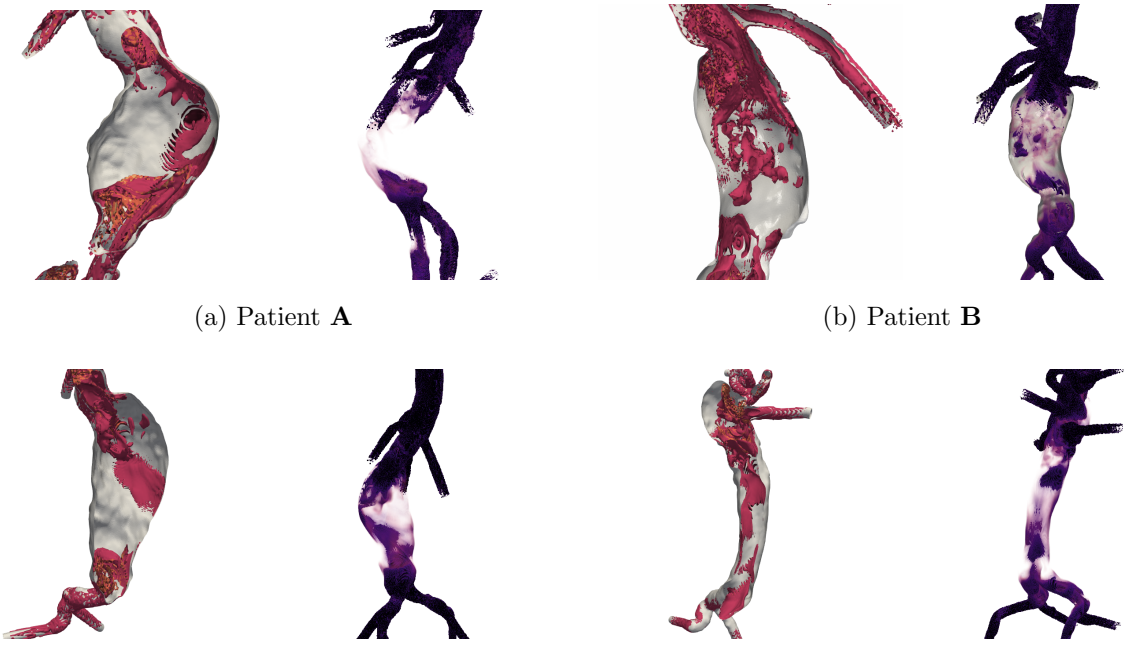

(a) Patient **A**

(b) Patient **B**

(c) Patient **C**

(d) Patient **D**

Figure 4.16 – Illustrative isocontour and volume rendering of LAVD in patient **A**, **B**, **C** and **D**.

4.4 Discussion and limitation

Flow alteration is thought to have a determining role on AAA development, potentially leading to rupture. On the one hand, the altered biomedical load on the arterial load can trigger mechano-adaptation of the artery and, on the other hand, flow topology may create favourable conditions for ILT deposition. However, translating CFD results into clinically significant quantities remains difficult. While the transport in AAA was observed through the scope of FTLE in chapter 3 ([JSG+18]) and the trace of the flow topology on the AAA lumen was computed in chapter 2 using the WSS, this chapter focuses on VSs as objective information on the transport phenomena in the aorta. Defining, extracting and visualizing vorticity and VSs are very active research fields in fluid dynamics, notably in turbulent and vortex dominated flow [PVH+03], and numerous quantities [GT18] have been proposed for various contexts. Here, three region-based methods are used, vorticity, IVD and LAVD, with a major focus on the temporal element of the phenomena.

After the pressure minimum (in a 2D inviscid flow only), vorticity is the simplest region-based method for VSs extraction, being computed as the curl of the velocity field. Vorticity was computed as a supportive information to help understand other fields and serve an illustrative purpose only, hence the simple thresholding. However, this approach may produce false positive in shear flow regions [Rob91]. This may be the cause of high vorticity values in the near wall region with high shear, making visualization difficult using thresholding alone. This is especially visible on Figure 4.12 (c) and Figure 4.14 (c). Nonetheless, vorticity snapshots offers an information of the rotational components of the flow velocity in the AAA. Even though not used in the build of a clinical risk criteria, Figure 4.9 to Figure 4.14 give insightful information on the rolling out of VS during a cardiac pulse. In the context of AAA, platelets motion, stress-activation and deposition are strongly believed to be crucial in the process of ILT initiation and thickening (see e.g. [HAS15, REAB07] and the *von Willebrand factor* [RM07]). Knowing the Stokes number of the platelets in blood is low ($St << 1$) [BHCG11, YLC04], they are passive in the flow

and thus strictly follow it. VSs tracking within a cardiac pulse will therefore provide information on platelet motion. Moreover, the development of the VS, i.e. formation (usually at the proximal neck and brutal enlargement), advection, stretching and distortion and, finally, breaking and diffusing, help understanding the transport dynamics in the AAA. This cascade is particularly visible on Figure 4.11, where the clipped view of vorticity shows the VS creation, detachment at the neck and advection in the core of the lumen before breaking mid-AAA. [BHCG11] observed the same pattern using the λ_2 criterion and made the connection with tendency of the ILT to be thicker in the lower half of the AAA. Here, patients **C** and **E** have thicker ILT in their lower part (see Figure 4.3). Platelets activated by the high shear present at the VSs frontier, transported by VS inside the AAA before breaking down with the risk of falling into a dynamically isolated zone [JSG+18]. Too few patients were here considered to conclude on this topic, especially given that patient **A** displays a clearly breaking of VSs in AAA mid-zone after a brutal enlargement, and the creation of an almost toroidal VSs (see Figure 4.9), but presents little to no ILT. Vorticity in patient **C** (see Figure 4.12) presents no notable increase in lumen diameter and no sharp geometry change at the proximal neck. Small sub-structures created at the renal arteries branching do not persist in the AAA and have totally vanished by the first third of the lumen. Interestingly, in patient **E** (see Figure 4.14), despite the same lack of brutal enlargement, VSs persists mid AAA at the apex of the lumen curvature, and ILT is present at the same location and below.

For the platelet activation process, a long enough exposure time above a critical shear [RZM79] plays a crucial role in thrombogenesis. Lagrangian methods capture the history of stress of individual platelets and seem therefore *de facto* more suitable to analyze biomechanical platelet activation, even though [HAS15] observed no significant difference between Eulerian and Lagrangian based activation potential approaches. Also, such methods require information on the activation upstream the region of interest, which is not know here and will not be considered.

IVD is a vorticity-based measure built by subtracting the local mean of the vorticity

field to itself [HHFH16], whose extrema is also objective [SKA99]. Integrating this field along the trajectories of the flow, and thus of platelets, creates the LAVD, objective as well. False positive present in shear regions are also included although [HHFH16] process to extract LCS discards structures present in near-wall high shear locations by discarding non-convex and non-closed surfaces. This promising approach did not produce exploitable results in this context, maybe due to an unsuitable pulsatile flow context. Nonetheless, Figure 4.16 presents insightful knowledge from the LAVD isocontour and LAVD volume rendering. LAVD isocontour can be interpreted as *primitive* LCS that will provide a starting point for interpretation. Also, one could argue that keeping false positive in high-shear regions makes sense in the platelet activation context. LAVD emphasizes for patient **A** the structures stemming from the impeding jet on the anterior side of the AAA, visible on the systolic part of Figure 4.9. For patient **B** and **C**, the breaking of VSs in the mid-zone of the AAA lumen is very visible, as well as the highly perturbed zone of the proximal neck. In patients **C** and **D**, near-wall structures with low curvature are visible, likely false LCS. In patient **D**, perturbations flowing from the renal branching are very visible, as well as for vorticity plots.

4.5 Conclusion

In this chapter, a Lagrangian approach to vortex detection was tested on AAAs and compared to the more standard vorticity. The AAAs presented various shapes, size and ILT deposition. First, the vorticity evolution during a cardiac cycle was discussed in the context of ILT formation through the adhesion of shear-activated platelets. Presented results are in agreement with the literature with similar Eulerian metrics. Mainly, in AAA with significant proximal neck enlargement, a jet forms during mid to end-systole, followed by VSs progressively stretching under shear and breaking into sub-structures, delivering potentially activated platelets in the mid zone of the AAA where blood velocity drops. More tubular or with smoother enlargement AAA will not experience the same phenomena

and VSs, if existing, will travel further down the AAA. When the computation of LAVD is pretty straight forward, extracting LCS from it is non-trivial in very complex flow and results from [HHFH16] could not be recreated. Yet, the simpler approach of extracting isolevel surfaces provided insightful information on the underlying Lagrangian structure of the flow. The initial goal of extracting a quantifiable metric to be compared to growth measures could not be achieved here, but including the flow history of platelets seems crucial to the prediction of ILT depositions, and thus, disease progression or patient at higher risk.

BIBLIOGRAPHY

BAH18. D Bhagavan, P Di Achille, and J D Humphrey. Strongly Coupled Morphological Features of Aortic Aneurysms Drive Intraluminal Thrombus. *Scientific Reports*, (August):1–18, 2018.

BGA+10. Jacopo Biasetti, T. Christian Gasser, Martin Auer, Ulf Hedin, and Fausto Labruto. Hemodynamics of the normal aorta compared to fusiform and saccular abdominal aortic aneurysms with emphasis on a potential thrombus formation mechanism. *Annals of Biomedical Engineering*, 38(2):380–390, 2 2010.

BHCG11. Jacopo Biasetti, Fazle Hussain, and T. Christian Gasser. Blood flow and coherent vortices in the normal and aneurysmatic aortas: A fluid dynamical approach to intraluminal thrombus formation. *Journal of the Royal Society Interface*, 8(63):1449–1461, 10 2011.

BKC00. J. R. Buchanan, C. Kleinstreuer, and J. K. Comer. Rheological effects on pulsatile hemodynamics in a stenosed tube. *Computers and Fluids*, 29(6):695–724, 2000.

DSL90. DAVID DEGANI, ARNAN SEGINER, and YUVAL LEVY. Graphical visualization of vortical flows by means of helicity. *AIAA Journal*, 28(8):1347–1352, 8 1990.

EBE+99. C. J. Egelhoff, R. S. Budwig, D. F. Elger, T. A. Khraishi, and K. H. Johansen. Model studies of the flow in abdominal aortic aneurysms during resting and exercise conditions. *Journal of Biomechanics*, 32(12):1319–1329, 12 1999.

EMBH+11. Mahdi Esmaily Moghadam, Yuri Bazilevs, Tain Yen Hsia, Irene E. Vignon-Clementel, and Alison L. Marsden. A comparison of outlet boundary treat-

ments for prevention of backflow divergence with relevance to blood flow simulations. *Computational Mechanics*, 48(3):277–291, 2011.

FSP12. Raphael Fuchs, Benjamin Schindler, and Ronald Peikert. Scale-Space Approaches to FTLE Ridges. pages 283–296. Springer, Berlin, Heidelberg, 2012.

GT18. Tobias Günther and Holger Theisel. The State of the Art in Vortex Extraction. *Computer Graphics Forum*, 37(6):149–173, 9 2018.

Hal02. G. Haller. Lagrangian coherent structures from approximate velocity data. *Physics of Fluids*, 14(6):1851–1861, 6 2002.

Hal11. George Haller. A variational theory of hyperbolic Lagrangian Coherent Structures. *Physica D: Nonlinear Phenomena*, 240(7):574–598, 2011.

Hal15. George Haller. Lagrangian Coherent Structures. *Annual Review of Fluid Mechanics*, 47(1):137–162, 1 2015.

Hal16. George Haller. Dynamic rotation and stretch tensors from a dynamic polar decomposition. *Journal of the Mechanics and Physics of Solids*, 86:70–93, 1 2016.

HAS15. Kirk B. Hansen, Amirhossein Arzani, and Shawn C. Shadden. Mechanical Platelet Activation Potential in Abdominal Aortic Aneurysms. *Journal of Biomechanical Engineering*, 137(4):041005, 4 2015.

HHFH16. G. Haller, A. Hadjighasem, M. Farazmand, and F. Huhn. Defining coherent vortices objectively from the vorticity. *Journal of Fluid Mechanics*, 795:136–173, 2016.

JSG+18. Florian Joly, Gilles Soulez, Damien Garcia, Simon Lessard, and Claude Kauffmann. Flow stagnation volume and abdominal aortic aneurysm growth:

Insights from patient-specific computational flow dynamics of Lagrangian-coherent structures. *Computers in Biology and Medicine*, 92:98–109, 1 2018.

KYM+93. P. J. Kilner, G. Z. Yang, R. H. Mohiaddin, D. N. Firmin, and D. B. Longmore. Helical and retrograde secondary flow patterns in the aortic arch studied by three-directional magnetic resonance velocity mapping. *Circulation*, 88(5 I):2235–2247, 11 1993.

LC07. Francois Lekien and Chad Coulliette. Chaotic stirring in quasi-turbulent flows. *Philosophical Transactions of the Royal Society A: Mathematical, Physical and Engineering Sciences*, 365(1861):3061–3084, 2007.

LH12. Qin Liu and Hai Chao Han. Mechanical buckling of artery under pulsatile pressure. *Journal of Biomechanics*, 45(7):1192–1198, 2012.

LTA+13. Trung B. Le, Daniel R. Troolin, Devesh Amatya, Ellen K. Longmire, and Fotis Sotiropoulos. Vortex phenomena in sidewall aneurysm hemodynamics: Experiment and numerical simulation. *Annals of Biomedical Engineering*, 41(10):2157–2170, 2013.

MBRvdV11. G. Mulder, A. C B Bogaerds, P. Rongen, and F. N. van de Vosse. The influence of contrast agent injection on physiological flow in the circle of Willis. *Medical Engineering and Physics*, 33(2):195–203, 2011.

MGG+70. C. J. Mills, I. T. Gabe, J. H. Gault, D. T. Mason, J. Ross, E. Braunwald, and J. P. Shillingford. Pressure-flow relationships and vascular impedance in man. *Cardiovascular Research*, 4(4):405–417, 1970.

MMKB94. J.E. E. Moore, S.E. E. Maier, D.N. N. Ku, and P. Boesiger. Hemodynamics in the abdominal aorta: A comparison of in vitro and in vivo measurements. *J Appl Physiol*, 76(4):1520–1527, 4 1994.

MPR+11. Umberto Morbiducci, Raffaele Ponzini, Giovanna Rizzo, Marcello Cadioli, Antonio Esposito, Franco Maria Montevecchi, and Alberto Redaelli. Mechanistic insight into the physiological relevance of helical blood flow in the human aorta: An in vivo study. *Biomechanics and Modeling in Mechanobiology*, 10(3):339–355, 6 2011.

PPF+11. Armin Pobitzer, Ronald Peikert, Raphael Fuchs, Benjamin Schindler, Alexander Kuhn, Holger Theisel, Krešimir Matković, and Helwig Hauser. The State of the Art in Topology-Based Visualization of Unsteady Flow. *Computer Graphics Forum*, 30(6):1789–1811, 9 2011.

PVH+03. Frits H. Post, Benjamin Vrolijk, Helwig Hauser, Robert S. Laramee, and Helmut Doleisch. The State of the Art in Flow Visualisation: Feature Extraction and Tracking. *Computer Graphics Forum*, 22(4):775–792, 12 2003.

REAB07. Sagi Raz, Shmuel Einav, Yared Alemu, and Danny Bluestein. DPIV prediction of flow induced platelet activation-comparison to numerical predictions. *Annals of Biomedical Engineering*, 2007.

RKCdT+06. Madhavan L. Raghavan, Jarin Kratzberg, E. M. Castro de Tolosa, Mauro M. Hanaoka, Patricia Walker, Erasmo Simão da Silva, Erasmo Magalhães Castro de Tolosa, Mauro M. Hanaoka, Patricia Walker, and Erasmo Simão da Silva. Regional distribution of wall thickness and failure properties of human abdominal aortic aneurysm. *J Biomech*, 39(16):3010–3016, 2006.

RM07. Zaverio M. Ruggeri and G. Loredana Mendolicchio. Adhesion mechanisms in platelet function, 2007.

Rob91. S. Robinson. Coherent Motions In The Turbulent Boundary Layer. *Annual Review of Fluid Mechanics*, 1991.

RZM79. J. M. Ramstack, L. Zuckerman, and L. F. Mockros. Shear-induced activation of platelets. *Journal of Biomechanics*, 12(2):113–125, 1979.

SG88. T. H. Solomon and J. P. Gollub. Chaotic particle transport in time-dependent Rayleigh-Bénard convection. *Physical Review A*, 1988.

SKA99. Roger C. Strawn, David N. Kenwright, and Jasim Ahmad. Computer Visualization of Vortex Wake Systems. *AIAA Journal*, 37(4):511–512, 4 1999.

SLM05. Shawn C. Shadden, Francois Lekien, and Jerrold E. Marsden. Definition and properties of Lagrangian coherent structures from finite-time Lyapunov exponents in two-dimensional aperiodic flows. *Physica D: Nonlinear Phenomena*, 212(3-4):271–304, 12 2005.

SPFT12. Benjamin Schindler, Ronald Peikert, Raphael Fuchs, and Holger Theisel. Ridge Concepts for the Visualization of Lagrangian Coherent Structures. pages 221–235. Springer, Berlin, Heidelberg, 2012.

TCRH11. J. Tong, T. Cohnert, P. Regitnig, and G. A. Holzapfel. Effects of age on the elastic properties of the intraluminal thrombus and the thrombus-covered wall in abdominal aortic aneurysms: Biaxial extension behaviour and material modelling. *European Journal of Vascular and Endovascular Surgery*, 42(2):207–219, 8 2011.

Tru18. Clifford. Truesdell. *The Kinematics of Vorticity*. Dover Publications, 2018.

VCFJT10. I. E. Vignon-Clementel, C. A. Figueroa, K. E. Jansen, and C. A. Taylor. Outflow boundary conditions for 3D simulations of non-periodic blood flow and pressure fields in deformable arteries. *Computer Methods in Biomechanics and Biomedical Engineering*, 13(5):625–640, 10 2010.

WMWV02. David H.J. Wang, Michel S. Makaroun, Marshall W. Webster, and David A. Vorp. Effect of intraluminal thrombus on wall stress in patient-specific mod-

els of abdominal aortic aneurysm. *Journal of Vascular Surgery*, 36(3):598–604, 10 2002.

WOBSS85. L. J. Wurzinger, R. Opitz, P. Blasberg, and H. Schmid-Schonbein. Platelet and coagulation parameters following millisecond exposure to laminar shear stress. *Thrombosis and Haemostasis*, 54(2):381–386, 1985.

WVDA+13. J. S. Wilson, L. Virag, P. Di Achille, I. Karšaj, and J. D. Humphrey. Biochemomechanics of Intraluminal Thrombus in Abdominal Aortic Aneurysms. *Journal of Biomechanical Engineering*, 135(2):021011, 2 2013.

XHF13. Nan Xiao, Jay D. Humphrey, and C. Alberto Figueroa. Multi-scale computational model of three-dimensional hemodynamics within a deformable full-body arterial network. *Journal of Computational Physics*, 244:22–40, 2013.

YLC04. K.F. Yu, K.S. Lau, and C.K. Chan. Large eddy simulation of particle-laden turbulent flow over a backward-facing step. *Communications in Nonlinear Science and Numerical Simulation*, 9(2):251–262, 4 2004.

ZGL+16. Byron A. Zambrano, Hamidreza Gharahi, ChaeYoung Young Lim, Farhad A. Jaberi, Jongeun Choi, Whal Lee, and Seungik Baek. Association of Intraluminal Thrombus, Hemodynamic Forces, and Abdominal Aortic Aneurysm Expansion Using Longitudinal CT Images. *Annals of Biomedical Engineering*, 44(5):1502–1514, 5 2016.

CHAPTER 5

Conclusion

The conclusion of each chapter gives the proposed perspectives:

- Recent focus in multiscale and multiphysics coupling of the biological reactions occurring in the ILT and arterial wall, to the mechanical load and blood flow, will be crucial in understanding mechanisms causing AAA growth.

- Growth & remodelling simulations will provide even more patient specific risk assessment, especially with the development of clinically available non-invasive material properties measurement.

- Build in the context of clinically available data, it would be interesting to validate risk predictor build in chapter 2 on a larger cohort of patients.

As a general conclusion, we retain the following contribution:

- chapter 3 was published in *Computers in Biology and Medicine* and is accessible at https://doi.org/10.1016/j.compbiomed.2017.10.033. It illustrated the difficulty to understand the transient flow topology in AAA while it is a known risk contributor. The computation of FTLE, despite mathematical drawbacks, provided

an accessible method to visualize LCS and mark out dynamically isolated zones in the AAA.

- chapter 2 was submitted for publication. Even if patient heterogeneity came up in literature, the data aggregated in this study highlighted its importance in every aspect approached. Unexpectedly, relationships between blood flow and AAA growth could be inverted from one patient to another. This could be a reason for the failure in building better risk criteria based on flow in the last two decades. This heterogeneities were even more marked when looking at local correlation, in opposition to my expectations. Besides those disappointed initial results, the combination of several criteria provided great risk assessment results and could be a starting point for a larger cohort study.

- chapter 4 provided qualitative information on the development of vortical structures in AAA of different shapes. Statistical information gathered on a larger scale in chapter 2 are essential from a clinical point of view, and being able to observe the flow and its characteristics varying during a cardiac pulse is crucial for research where it helps feeling and understanding the flow topology. No new criteria was build but both the tested Lagrangian and LAVD approaches provided an efficient and elegant way to visualize the history of flow structures in the AAA, from their development at the proximal neck to their breaking and diffusion. We could show the absence of coherent structures in some AAAs, especially the fusiform ones, despite the presence of ILT, which leads to further questioning on its formation and growth mechanisms.

*

* *

This thesis focused on both the creation of composite multiphysics metrics using deep-learning, and the exploration of the little known role and the quantification of transport phenomena in AAA. No transport metrics were included in the learning algorithm presented in chapter 2 : the FTLE based LCS extraction described in chapter 3 ended up

being too user-dependant, and lacked robustness and LAVD based LCS described in chapter 4 did not achieve the extraction of dynamically isolated zones adequately. However, the latter offers a very robust and automatic region detection, and shall be further explored. The combination of WSS and transport-derived features in the decision tool may offer an even better diagnostic power. Deep-learning is entering all fields of research, shaking them up, and was here a powerful approach to combine features from different fields to the furtherance of the patient specific treatment. The clinical, hemodynamic and morphological data gathered, and the relationship between them could be a fertile ground for a growth & remodeling study. The simulation of the ILT development in AAA is still in its infancy, but the potential to better understand and predict the disease progression is tremendous. Even though chapter 2 concluded with a promising approach, future work should include a wider variety of AAA dynamics. Recent advances in deep-learning merges the information from little informative but available in big numbers datasets (e.g. numerous followed patients) with highly informative but available in little numbers datasets (e.g. ruptured AAA).

This document was produced in LaTeX.

All figures presented were made by me unless expressly stated in the figure caption. They were exclusively generated using open-source softwares : the *Matplotlib* and *Seaborn* Python libraries for graphs, *ParaView* for simulation rendering and *MITK* for medical images viewing.